Constraining Subglacial Heat Flux in Antarctica from Thermal Conductivity and Subglacial Lakes

Simon Robert Willcocks

March 30, 2023

Thesis submitted for the degree of

Doctor of Philosophy

in

Physical Sciences

at The University of Adelaide

Faculty of Engineering, Computer and Mathematical Sciences

School of Mathematical Sciences

THE UNIVERSITY
of ADELAIDE

ii

Contents

List of Tables

List of Figures

Signed Statement

I certify that this work contains no material which has been accepted for the award of any other degree or diploma in my name, in any university or other tertiary institution and, to the best of my knowledge and belief, contains no material previously published or written by another person, except where due reference has been made in the text. In addition, I certify that no part of this work will, in the future, be used in a submission in my name, for any other degree or diploma in any university or other tertiary institution without the prior approval of the University of Adelaide and where applicable, any partner institution responsible for the joint award of this degree.

The author acknowledges that copyright of published works contained within the thesis resides with the copyright holder(s) of those works.

I give permission for the digital version of my thesis to be made available on the web, via the University's digital research repository, the Library Search and also through web search engines, unless permission has been granted by the University to restrict access for a period of time.

Signed: .   Date: 30 - 02 - 2023 ....

Acknowledgements

I would like to thank the Editor Bernd Kulssa, Lenneke Jong and an anonymous reviewer for their constructive comments that helped improved earlier versions of chapter 3. And I would like to thank the editor, Cliff Atkins, and two anonymous reviewers for constructive comments that significantly improved chapter 6. I would also like to thank Jacqui Halpin for supping a portion of the rock samples used in thermal conductivity analysis, Samuel Jennings for explaining how to use the thermal conductivity scanner and Jessica Walsh for measuring mineralogy in a portion of the rock samples.

On a personal note, I would like to extend my sincere thanks to everybody who has helped me over the last 5 years in the completion of this thesis. To everybody in my office I am grateful for the help you have given me troubleshooting problems with MATLAB and Latex in order to get my scripts to work as intended. I hope I have helped you in return as much as you have helped me. I would also extend thanks to my parents for their consistent and unwavering support right from the beginning. To the numerous researchers, both inside and outside the university, that I have contacted over the last 5 years with queries about their studies, I am thankful for your thoughtful and timely responses. This has allowed me to better understand the wider subject matter and the current state of research. Their assistance in the reading and writing of scientific papers has been gratefully appreciated.

Dedication

I would like to dedicate this thesis to my primary supervisor, Derrick Hasterok. From the outset your belief in me and trust that I could and would succeed has instilled confidence. Your on-going guidance has been a rock that has kept me anchored during the inevitable storms that have come and gone during this research. I would simply not have made it to this point without you. I know how much time you have poured into helping me to complete this thesis and you deserve huge credit.

Abstract

Developing accurate models for the dynamics of ice sheets requires detailed knowledge of the temperature field within. An important constraint on internal ice sheet temperature is provided by geothermal heat flux, the heat flow from the solid Earth to the base of the ice sheet (Fowler 2006). This flow of heat is not uniform, varying as a result of differences in thermal properties (i.e., thermal conductivity and heat production) and variations in heat transfer across the lithosphere asthenosphere boundary. Since temperature can affect a range of ice properties, from strain rate to hardness and melting rate (Paterson 1994), it is important that we have a detailed understanding of the heat flux both below and within the Antarctic Ice Sheet so that I can accurately map internal temperature. In this thesis, I examine the heat flux in Antarctic environments as well as the properties and factors that distort it. I also take an indirect approach to test geothermal heat flux models by using melting associated with subglacial lakes as a constraint.

Heat can move both vertically and horizontally in order to find the path of least thermal resistance to the surface. The path is dictated by the thermal conductivity of the crustal material as heat will attempt to move through the most conductive material. In a subglacial valley, or buried bedrock high, most heat will move through the more conductive bedrock, resulting in heat being moved away from subglacial valleys and into bedrock in regions of geological contacts whereby heat will move into the more conductive of the two mediums. The result is the creation of localized regions where heat flux at the base of the ice sheet can be 80 to 120% of the regional heat flux creating localized regions of elevated/reduced temperature.

Having demonstrated the underlying bedrock thermal geology is critical to mapping

the flow of heat through the Antarctic ice sheet, I collected the thermal conductivity on 49 Antarctic rock samples and combined them with a larger global database to develop predictors for thermal conductivities in the inaccessible Antarctic lithosphere. From this dataset, I determine oxide and mineral contributions to the effective thermal conductivity for a range of igneous compositions. I exploit a correlation between high thermal conductivities and low seismic velocities to produce an empirical model, which is applied to a crustal tomography model to predict thermal conductivity of the Antarctic crust. The largest lateral conductivity variations are found in a region with high conductivity between 15 to 27 km, which also corresponds to an anomaly in proxy models for the geothermal heat flux beneath the Antarctic Ice Sheet.

Several geothermal heat flux models for Antarctica have been made via proxy-based estimates due to limited sampling across the continent. Proxy-based estimates have large disagreements between each other (up to 50 mW m^{-2} in West Antarctica). To ascertain accuracy, I test the proxy-based estimates using a basal heat flux constraint (BHFC) assuming melting at the base of the ice sheet. In the presence of subglacial lakes, regions where proxy-based estimates should exceed this constraint. I find that while results show a subtle relation between lake and regions of elevated heat flux, a large number of lakes are in regions of insufficient heat flux to generate melting. These results indicates that current proxy models currently underestimate geothermal heat flux.

Since there is a relation between heat flux and lake locations, the proxy-based estimates can be combined with other maps of Antarctic surface temperature, ice thickness, bedrock elevation, crustal thickness, bedrock slope and ice velocity to predict lake melt source regions. Three methods are tested, comparative property analysis, principal component analysis and machine learning method using a Subspace KNN classifier. The comparative analysis shows the properties of surface temperature, ice thickness and ice velocity to have the greatest disparity between sub-glacial lakes and Antarctica but are unable to make a clear prediction about the melt source for subglacial lakes. The PCA, while shown not to be a good predictive map, is excellent at identifying regions of Antarctica as either containing active lakes (with current water infill/outflow) or stable lakes (in which water

levels remain constant). The Subspace KNN classifier meanwhile, is able to both identify lake melt sources and type of lakes generated from those sources.

This work improves our ability to accurately map the geothermal heat flux at the base of the Antarctic ice sheet by giving proxy modellers by showing the importance of bedrock thermal conductivity as well as mapping it over a large section of Antarctica. We also show future avenues of research that can improve upon or use these geothermal heat flux models including mapping the melt sources of subglacial lakes.

Chapter 1

Introduction

1.1 Contextual statement

With the role of humans on recent climate change now well established (Lynas et al. 2021), more attention has turned to the forecasting of future effects (Lwasa et al. 2022). The melting of polar ice caps, in Greenland and Antarctica has resulted in rising global sea levels and accelerated climate change (DeConto et al. 2021). To accurately model warming temperatures on ice caps a detailed model for glacial thermodynamics is required. To achieve this degree of accuracy, we need to improve models of temperatures within ice sheets and geothermal heat flux from below.

Geothermal basal heat flux establishes the rate at which temperature increases throughout an ice sheet, and thus is key to determining whether the base of the ice sheet is frozen or melting (Reading et al. 2022). The true geothermal heat flux at the base of the Antarctic ice sheet has never been directly measured outside of a handful of boreholes mostly taken in thin-ice coastal regions (Guimarães et al. 2020).

Rather than direct measurements, multiple studies have attempted to map the heat flux at the base of the Antarctic ice sheet using geophysical proxies such as Curie depth (Maule 2005, Martos et al. 2017), seismic velocity (An et al. 2015, Shen et al. 2020) and statistical comparisons (Lösing et al. 2020, Stål et al. 2021). These models are limited both due to the lack of accurate thermal properties, thermal conductivity and radioactive heat production of the Antarctic bedrock. These models also do not address small-scale

thermodynamic effects, sheet such as the refraction of heat flux induced by subglacial topography (van der Veen et al. 2007).

The magnitude of basal heat flux can influence the formation of melts at the base of the Antarctic ice sheet (Pattyn et al. 2016), which may pool in low topographic depressions to form subglacial lakes (MacKie et al. 2020). These subglaial lakes reduce bed rock friction (Gudlaugsson et al. 2016) and distort the solid Earth temperature field (Siegert et al. 2017). Outside of glacial dynamics, biologists have a keen interest in subglacial lakes due to the possible existence of unique, complex life-forms in these isolated and extreme environments (Pearce et al. 2013). With subglacial lakes cut off from the outside world by kilometers of ice sheets, life can evolve in isolation with unique traits and features that may not exist in currently known creatures (Christner et al. 2014). These extremely cold environments also serve as analogues for other bodies in the solar system such as the icy moons of Jupiter where extremophiles may be found (Thatje et al. 2019). Thus, there are a multitude of reasons we must improve our knowledge of the thermal properties of the Antarctic lithosphere and the geothermal heat flux at the base of the Antarctic Ice Sheet.

1.2   Objectives and thesis outline

In this thesis, I explore two distinct avenues in an effort to improve geothermal heat flux either directly or through further study. First, I examine the thermal conductivity of the Antarctic lithosphere and the effects lateral variations may have on the magnitude and distribution of geothermal heat flux continent wide. Second, I examine the relation between glacial geothermal profiles and subglacial lakes and use it to test several geophysical models of Antarctic geothermal heat flux.

Chapter 2: Background

In this background chapter, I describe several key aspects for the nature of heat flow in ice sheets relevant to this study and clarify the terminology used in later chapters.

Chapter 3: Thermal refraction: implications for subglacial heat flux

In this chapter, I examine the flow of heat across the ice-rock interface at the base of ice sheets. I show that topographic and geological differences around the ice-rock boundary can cause the heat to refract laterally away from thermal restive locations and towards thermal conductive locations. This refraction of heat causes temperature decreases/increases, resulting in ice remaining solid to much greater depths or melting much shallower than a simple 1D gradient predicts. These results highlights the importance of accurate subglacial topography models and geological architecture for the Antarctic bedrock when modeling the basal geothermal heat flux.

Chapter 4: Compositional controls on the thermal conductivity of igneous rocks and a model for the conductivity of Antarctic crust

Having established the importance of thermal conductivity variations on the flow of heat in glaciers, I report on a laboratory investigation of the thermal conductivity of 49 Antarctic igneous and metaigneous rocks. I show the thermal conductivity of these samples are within the expected ranges of the global distribution for their composition. Since Antarctic samples follow global trends we use the global relationship between seismic velocity and thermal conductivity to transform a map of Antarctica crustal velocity into a map of crustal thermal conductivity.

Chapter 5: Melt constraints on the Geothermal Heat Flux beneath the Antarctic Ice Sheet

While Chapters 3 and 4 focus on small-scale heat flux effects ($\sim$1 to 20 km), this chapter examines the basal heat flux in Antarctica at the continental scale. Current heat flux models of Antarctica vary widely. To constrain these models, I calculate the heat flux required to reach the melting point at the base of the ice sheet. This limit, combined

with the presence or absence of lakes, can be used to bound geothermal heat flux and test existing geophysical proxy models.

Chapter 6: Prediction of subglacial lake melt sources from site characteristics

I attempt to map lake melt sources across Antarctica using seven site parameters with some sensitivity to the thermal state. Machine learning methods are used to identify where in Antarctica where melt sources form. From these results, I predict in Antarctica as ideal melt is sourced. I also predict the types of lakes formed in said regions.

Chapter 7: Conclusion

In this final chapter, I address the issues faced in current heat flux models and how these studies improve our understanding and knowledge of the thermal state of the Antarctic Ice Sheet. I also suggest the results of this study can be extended to improved ice sheet models.

Chapter 2

Background

2.1 Heat/heat flux

Heat measures the rate at which temperature is transferred (flows) from one location to another and is measured in watts (W) ([Lienhard & Lienhard 2019]). Heat flux is a measurement of the amount of heat passing through a 2D plane, such as the Earth surface, and is measured in Watts per squared meter (W m^{-1}). Heat can be transferred by four mechanisms:

- Advection: The process of heat being transferred along with the mass containing it and occurs in all moving substances, such as flowing liquids.

- Convection: Works in the same way as advection, in which the mass is transferred along with the heat. When gasses and liquids are warmed at the base, a circulatory motion will occur in the substance as the warm, less dense part of the substance rises to the top of the medium, while the colder, more dense part falls to the base.

- Conduction: Heat can also move within a solid substance via conduction. Warm molecules within a lattice will slowly dissipate heat throughout any substance at a rate determined by the substance's temperature difference and thermal conductivity.

- Radiation: Heat can move through a vacuum in the form of electromagnetic waves ([Maxwell 2009]). All substances with a temperature above absolute zero will emit

thermal radiation, with hotter substances emitting more radiation at higher energies.

2.2   Heat in glaciers

Glaciers present a unique environment for heat flow due to the nature of ice as both a solid and a geophysical fluid (Paterson 1994). As a solid, heat flow in the ice is predominately driven by thermal conduction (Paterson 1994), however, due to snow build up and ice's nature to flow over the long term, we also see heat flow as a result of mass transport (thermal advection) and convection (Hughes 2012). Heat is also generated internally within a deforming ice sheet by viscous dissipation (Llubes et al. 2006) or at the base as ice shears over bedrock (Wilkens et al. 2015).

Heat flux is related to the thermal gradient by Fourier's law and can be tied to absolute temperatures by a known point (e.g., surface temperature, melting point at the base) (Paterson 1994). Temperature is a first-order control on ice dynamics, as colder and warmer ice behave differently. Ice properties such as rheology (Larour, Seroussi, Morlighem & Rignot 2012), basal friction (Goldsby & Kohlstedt 2001), basal sliding velocity (Sergienko & Hindmarsh 2013), and erosion (Greve & Blatter 2009) are all dependent on temperature. Temperatures can be estimated throughout an ice sheet by solving the heat equation as a boundary value problem. The basal boundary condition of the ice sheet is requires an estimate of the heat flux across the bed.

2.3   Geothermal heat flux models

The heat flux from the bedrock to the ice sheet is frequently assumed to be the geothermal heat flux—heat flux of the solid Earth—which can be estimated indirectly from geophysical proxies. The number studies estimating geothermal heat flux models for Antarctica has rapidly increased in the past few years. I have chosen six with particular interest to my study, which represent the full range of techniques used to predict heat flux. These studies include: Maule (2005) and Martos et al. (2017) estimate heat flux through the magnetic Curie depth estimates, An et al. (2015) uses mantle shear wave tomography,

which converts velocities into temperatures using a method similar to Goes et al. (2000). Guimarães et al. (2020) interpolates the heat flux from a series of ice drill cores, volcanic magma chambers, subglacial lakes, and sites based on the basal temperatures of the glaciers. Shen et al. (2020) estimate the heat flux across Antarctica by identifying regions of known heat flux on other continents with similar seismic characteristics (velocity and gradient) at ∼80 km depth. Stål et al. (2021) takes this concepts further comparing seismic profiles along with topographic, magnetotellurics and geological characteristics to compare Antarctic regions to other regions of known heat flux. All six models make broad uniform assumptions about the thermal properties of the Antarctic lithosphere (Chapter 5) raising questions about their accuracy, both magnitude and spatial variability of geothermal heat flux (Gard 2021).

Additional constraints can be placed on the heat flux at the base of an ice sheet that are independent of geophysical proxies. Since temperature increases with respect to depth, an ice sheet will inevitably reach the melting point of ice if thick enough. The melting point normally occurs well below the Antarctic ice sheet in the bedrock. However, if the heat flux is high, the melting point will occur within the ice sheet and can result in the formation of subglacial lakes. I refer to the limit where melting first occurs as the minimum basal heat flux (Chapter 5). This constraint differs depending on the overlying ice sheet's surface temperature, ice thickness and surface velocity.

2.4 Subglacial lakes

In regions where the geothermal heat flux is high enough to melt the base of the ice sheet we expect subglacial lakes to form. Subglacial lakes are bodies of water located beneath the ice sheet that remain cut off from both the surface and the open ocean. They were originally theorized in the late 1960s (De et al. 1969) and then later confirmed in the early 1990s (Ridley et al. 1993). They are believed to be formed from the run off from basal melts which pool in regions of low bedrock topography (MacKie et al. 2020). More than 600 subglacial lakes have since been discovered in Antarctica through multiple radar and satellite observations (Livingstone et al. 2013). Lakes are split into two primary

categories: stable, in which water levels in the lake remain constant and active in which water levels in the lake will change as a result of inflow/outflow (MacKie et al. 2020). The existence of such lakes is important, as it has both an impact on ice dynamics (Siegert et al. 2000, Couston 2021) and biological (Siegert et al. 2001, Christner et al. 2014, Thatje et al. 2019) implications.

With subglacial lakes being located 1-4 km under an ice sheet they can only be detect via radio-echo sounding, in the case of stable lakes, or satellite observations of ice elevation, in the case of active lakes. These indirect methods mean that multiple smaller lakes have likely not yet been discovered (Chapter 6). More focused studies of specific Antarctic regions would allow us to make scans of finer resolution but to do so would first require a confidence that a subglacial lake exist in the region. This would be more likely in a region with identical environmental properties to a region with a known subglacial lakes (chapter 6).

2.5   Thermal properties of bedrock

Basal heat flux is dictated by a several factors but the two most important are radiogenic heat production and thermal conductivity. Heat production is generated within the Antarctic crust by the decay of uranium, thorium and potassium (Hasterok & Webb 2017) while thermal conductivity limits the rate at which mantle heat can flow to the surface (Paterson 1994). Both properties are controlled lithologically, but are relatively uncertain as a result of natural variability and unknown composition of the subsurface. Neither thermal conductivity nor heat production can be remotely sensed in the same way as seismic velocity or density, making it difficult to develop crustal models via indirect means.

Although measuring trace amounts of uranium, thorium and potassium in rocks is difficult, there is a relationship between heat production and sample maficity (Hasterok & Webb 2017). Using this trend, one can predict heat production of a rock from its composition. Since the composition of the rocks also affects its seismic velocity and density, one can draw a relationship between these variables and heat production, allowing

mapping of heat production in the Antarctic crust (Gard & Hasterok 2021).

This relation between heat production and composition is also true for thermal conductivity although by different factors (S. Jennings 2019). Thus, one can generate a map of heat production in the Antarctic crust via relating thermal conductivity results to seismic velocity maps of the Antarctic region. However, with few observations globally and within Antarctica, additional measurements are needed (Chapter 4).

2.6 Bedrock Erosion

As the Antarctic ice sheet moves across the continent, it abrades the underlying bedrock. Due to the positive geothermal gradients, this erosion exposes the base of the Antarctic Ice Sheet to warmer temperatures and higher heat flow as geotherms reequilibrate (England & Richardson 1980). The magnitude of the thermal gradient disturbance due to erosion is dependent upon the rate and duration of erosion, with an increase in each causing a larger disturbance (Ehlers 2005).

While the thermal effect of erosion must be included in models to estimate heat flux accurately in coastal regions, the effect can largely ignored over much of Antarctica's continental interior. The erosion rate within Antarctica's continental interior is poorly constrained. Cosmogenic studies of erosion rates suggest extremely low erosion rates, generally less than 10^-3 mm a^{-1} (Marrero et al. 2018). However, these observations are based on rock outcrops that may not experience significant abrasive erosion from glacial sliding or subglacial fluvial processes which can exceed 10^3 mm a^{-1} (Fagherazzi et al. 2021), but such rates cannot be sustained over thousands of years and must be constrained to coastal regions where glacial velocities are highest. To estimate erosion rates in the Antarctic interior, we can make predictions from observations from temperate glaciers, which indicate a relationship between sliding velocity and erosion rates (Cook et al. 2020). A sliding velocity of 10 m a^{-1} to 100 m a^{-1} results in estimated erosion rates of 0.7 to 3.2 mm a^{-1} (Figure 2, Cook et al. 2020). Ice velocities in the Antarctic interior rarely exceed 25 m a^{-1}, corresponding to an erosion rate likely less than 1.3 mm a^{-1}. For such low erosion rates, we expect the heat flux disturbance to remain ¡10% for well over duration

less than 20 ka (Figure 5d, Ehlers 2005). While the ice sheet has existed for ∼34 million years ago (Barr et al. 2022), it is reasonable to assume the duration of flow due to the duration of glacial interglaical cycles of ∼40 ka. Therefore, it is reasonable to assume the erosional effect on heat flux is negligible within the continental interior and so, it is ignored in modelling components this thesis.

Statement of Authorship

Title of Paper	Thermal Refraction: Thermal refraction: implications for subglacial heat flux
Publication Status	● Published ☐ Accepted for Publication ☐ Submitted for Publication ☐ Unpublished and Unsubmitted work written in manuscript style
Publication Details	Willcocks, S., Hasterok, D., and Jennings, S. (2021). Thermal refraction: implications for subglacial heat flux. Journal of Glaciology, pages 1–10.

Principal Author

Name of Principal Author (Candidate)	Simon Robert Willcocks
Contribution to the Paper	Conceived the idea, wrote the main paper and generated figures.
Overall percentage (%)	70%
Certification:	This paper reports on original research I conducted during the period of my Higher Degree by Research candidature and is not subject to any obligations or contractual agreements with a third party that would constrain its inclusion in this thesis. I am the primary author of this paper.
Signature	Date 17/12/2022

Co-Author Contributions

By signing the Statement of Authorship, each author certifies that:

    i.   the candidate's stated contribution to the publication is accurate (as detailed above);

    ii.   permission is granted for the candidate in include the publication in the thesis; and

    iii. the sum of all co-author contributions is equal to 100% less the candidate's stated contribution.

Name of Co-Author	Derrick Hasterok
Contribution to the Paper	Supervised the paper, proofread and adjusted the figures and final text.
Signature	Date 20 Nov 2022

Name of Co-Author	Samuel Jennings
Contribution to the Paper	Added additional paragraph on the nature of rock thermal conductivity.
Signature	Date 28/11/2022

Please cut and paste additional co-author panels here as required.

Chapter 3

Thermal refraction: implications for subglacial heat flux

Abstract

In this study, we explore small-scale ($\sim$1 to 20 km) thermal-refractive effects on basal geothermal heat flux (BGHF) at subglacial boundaries resulting from lateral thermal conductivity contrasts associated with subglacial topography and geologic contacts. We construct a series of two-dimensional, conductive, steady-state models that exclude many of the complexities of ice sheets in order to demonstrate the effect of thermal refraction. We show that heat can preferentially flow into or around a subglacial valley depending on the thermal conductivity contrast with underlying bedrock, with anomalies of local BGHF at the ice–bedrock interface between 80 to 120% of regional BGHF and temperature anomalies on the order of $\pm 15\%$ for the typical range of bedrock conductivities. In the absence of bed topography, subglacial contacts can produce significant heat flux and temperature anomalies that are locally extensive ($>$10 km). Thermal refraction can result in either an increase or decrease in the likelihood of melting and ice sheet stability depending on the conductivity contrast and bed topography. While our models exclude many of the physical complexities of ice behaviour, they illustrate the need to include refractive effects created by realistic geology into future glacial models to improve the

prediction of subglacial melting and ice viscosity.

3.1   Introduction

Geothermal heat flux at the base of ice sheets (basal geothermal heat flux, BGHF) is a critical boundary constraint on ice sheet models because it plays a key role in the basal temperature and thermal gradients within glaciers (Pittard et al. 2016). Accurate models of BGHF are necessary to predict subglacial melting rates, flow velocities in continental ice sheets, and identify regions of extremely old ice (Pittard et al. 2016, Larour, Morlighem, Seroussi, Schiermeier & Rignot 2012, Liefferinge & Pattyn 2013, Parrenin et al. 2017). Despite the importance BGHF, there are very few direct estimates aside from a few core sites (e.g., Parrenin et al. 2017) and estimates made using subglacial lakes (Siegert & Dowdeswell 1996).

Heat flux at the base of the Antarctic ice sheet is poorly constrained, leading many glacial modelers to use simple BGHF estimates to estimate temperature at the base of the Antarctic ice sheet (Llubes et al. 2006, Larour, Seroussi, Morlighem & Rignot 2012). Uncertainty in BGHF results in subglacial temperature models, that cannot accurately predict subglacial melting. While more recent BGHF models derived from seismic tomography and Curie depth estimates are available (An et al. 2015, Martos et al. 2017, Lösing et al. 2020, Shen et al. 2020), these models are not of sufficient resolution to observe local thermal variations that may be significant to glacial processes (Liefferinge & Pattyn 2013). These processes include the raising or lowering of the strain rate of ice (Goldsby & Kohlstedt 2001), the formation of fast sliding ice streams (Engelhardt 2004), and the formation of subglacial lakes in regions not defined by basic 1-D thermal gradients (Llubes et al. 2006). Furthermore, to estimate BGHF, these geophysical models rely on simple estimates of crustal heat production and thermal conductivity that are poorly constrained. In this study, we focus on the implications of shallow differences in thermal conductivity on temperature and heat flux at the ice–bedrock interface.

Heat moves from the lithosphere to the surface via the path of least resistance (Beardsmore & Cull 2001), which is predominantly vertical due to the difference in temperature
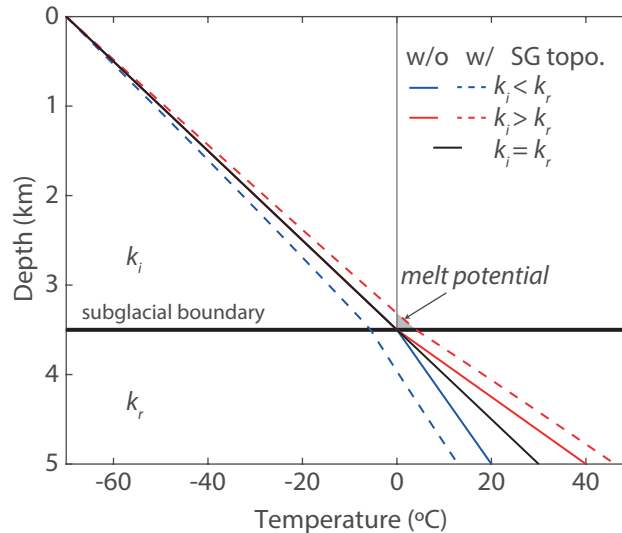
Figure 3.1: Thermal refraction as a result of a conductivity contrast between ice and bedrock. The solid lines are for a 1-D temperature model where the underlying bedrock is more conductive than the ice (blue), less conductive (red), and equal (black). The dashed lines are computed for a 2-D temperature model through the center of a Gaussian-shaped valley (same models in Fig. 3.5). Because we do not factor in latent heat effects, temperatures above the melting point can be considered a melt potential (grey).

between the base of the lithosphere and the surface. Surface topography and lateral variations in composition cause the flow of heat to deviate from a straight path, resulting in a horizontal component of heat flux and creating local anomalies (Lees 1910, Lachenbruch 1968). A prior model for heat flux at the base of glaciers assumed the interface could be modelled as a topographic free surface (van der Veen et al. 2007). However, this assumption is physically incorrect because it ignores refraction of heat flux and temperature at the ice–bedrock interface as a result of a finite thermal conductivity of ice.

Thermal refraction distorts local thermal gradients in response to a contrast in thermal conductivity (Fig. 3.1). The effects of thermal refraction have been observed and accurately modelled within and around sedimentary basins (Stephenson et al. 2009, Fuchs & Balling 2016). This refraction effect also has the potential to influence glacial and geothermal processes, as refraction locally focuses heat and temperatures relative to the surrounding area. This redistribution of heat affects viscosity due to its temperature sensitivity (Goldsby & Kohlstedt 2001) and the potential for subglacial melting. Furthermore, this phenomenon also accounts for local heat flux variations in the absence of subglacial topography.

In this study we demonstrate that, with or without subglacial topography, thermal refraction can affect the heat flux at the ice–bedrock interface, alluding to much warmer and cooler sections under the ice sheet. We suggest that thermal refraction creates regions of localized high temperature and heat flux anomalies that can raise melt potential, and may be responsible for subglacial lake formation.

3.2   Background

3.2.1   Topographic effect

The topographic method, originally theorized by Lees (1910) and later expanded by Lachenbruch (1968), accounts for surface heat flux into regions of low topography and away from high topography. van der Veen et al. (2007) proposed that the heat flux across the glacial–bedrock boundary can be described as a free surface and modeled using a topographic method, which they employed to describe the heat flux across the Petermann and Jakobshavn Isbræ subglacial boundaries in Greenland.

While air is very resistive, air currents—unlike ice—can convect thereby rapidly removing heat and creating a relatively constant temperature along the surface topography (i.e. the topographic effect). The result is a compression of isotherms in the vicinity of topographic depressions and associated increase in heat flux (Fig. 3.2). Beneath topographic highs, the opposite occurs, the distance between isotherms increases and heat flows away from the peak. The topographic model has been used by a number of glaciological studies and site planning. For example, in their recommendation for selection of an ice coring site, Passalacqua et al. (2018) suggest avoiding sites above subglacial valleys under the assumption that heat would be drawn into a valley and increasing the possibility of positive melting. In a separate study by Young et al. (2017), the authors assumed topography would increase the potential for subglacial lakes in regions of deeply incised topography.

By using the topographic method, van der Veen et al. (2007) assumed the ice–bedrock boundary can be recast as Earth's free surface (Fig. 3.2) however this assumption is
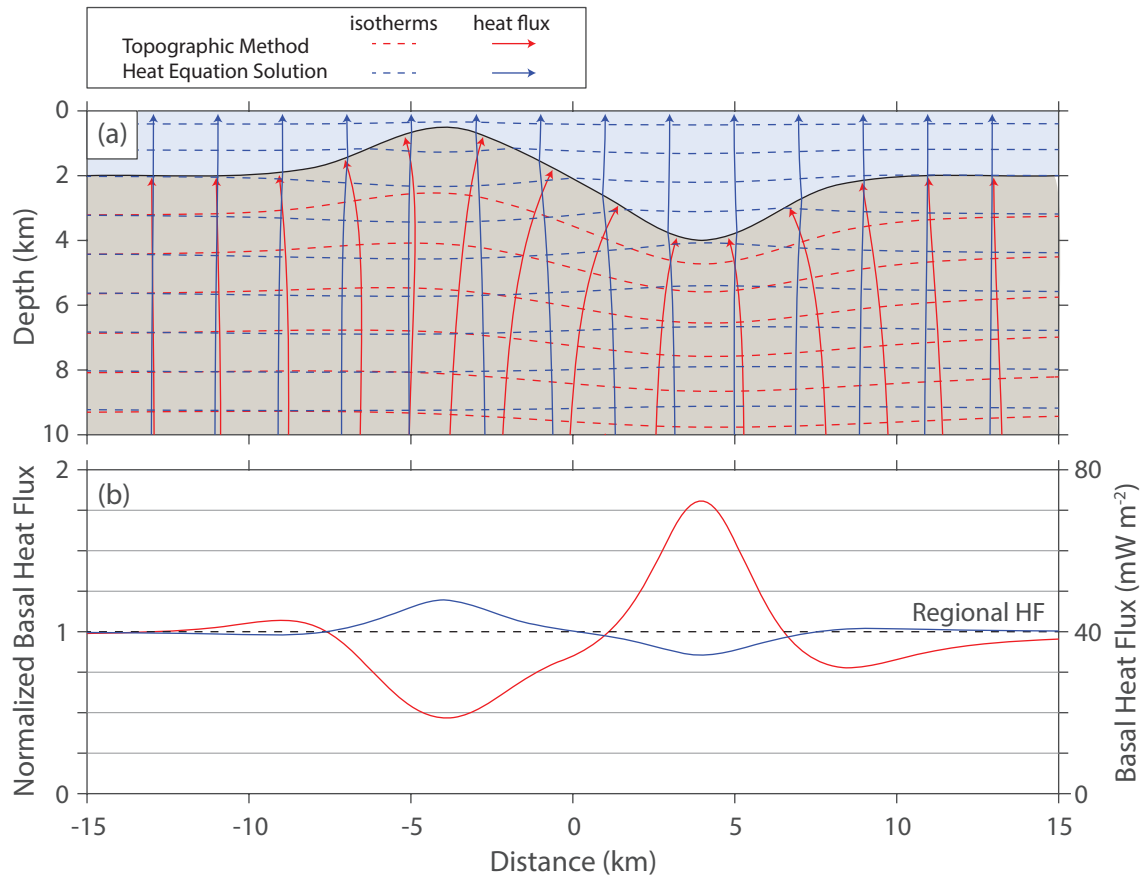
Figure 3.2: A comparison of the topographic method (red) with the finite difference solution (blue) for a subglacial ridge and valley. The ice layer (light blue) is assigned a conductivity of 2 W m^{-1} K^{-1}and the bedrock (light brown) is assigned a conductivity of 3 W m^{-1} K^{-1}. The dashed lines and solid lines in (a) refer to the isotherms and heat flux lines, respectively. The topographic model is undefined in the ice whereas the isotherms extend across both layers in the finite difference model. (b) Basal heat flux anomalies for the topographic (red) and finite difference solutions (blue). The left axis displays the normalized heat flux anomaly (Equation 3.6) whereas the right axis displays the heat flux computed for regional heat flux of 40 mW m^{-2}.

incorrect. For the topographic method to work in glacial systems, ice would need to be much more conductive than the bedrock or convect rapidly, both beyond what is practically possible. Earth materials—including ice—vary in thermal conductivity due to differences in composition, porosity, and pore fluid. A conductivity contrast between ice and bedrock can result in thermal refraction of heat that can produce the opposite effect on heat flow above subglacial highs and valleys as predicted by the topographic method (Fig. 3.2). Therefore, thermal refractive effects must be considered for accurate glacial and ice sheet models.

In this study, we revisit the basal heat flux in response to subglacial topography using the finite difference method, which can account for variations in thermal conductivity.

3.2.2 Thermal conductivity

Ice

The thermal conductivity of Antarctic ice varies considerably as a function of porosity and temperature (Pringle et al. 2007). Pure ice at 0°C has a thermal conductivity of ~2.1 W m^{-1} K^{-1} and at -50°C (typical surface temperature in East Antarctica) ice is more conductive, 2.8 W m^{-1} K^{-1} (Paterson 1994). In practice, the conductivity of glacial ice is lower than the pure ice limit as air bubbles in accumulating snow are trapped as the snow compacts into glacial ice. As snow compacts, it increases in both density and thermal conductivity (Equation 9.3 and 9.4 in Paterson 1994). Using density data from Kuivinen & Koci (1982), we can estimate the upper and lower bounds of glacial ice thermal conductivity, which can be as low as 0.5 W m^{-1} K^{-1} near the surface and rapidly increases with depth to that of pure ice around 200 m (Fig. 3.3a). Observations of sea ice conductivity compiled by Pringle et al. (2007) are consistent with this theoretical model. A complete set of equations to estimate conductivity of ice with depth is provided in the Appendix A.
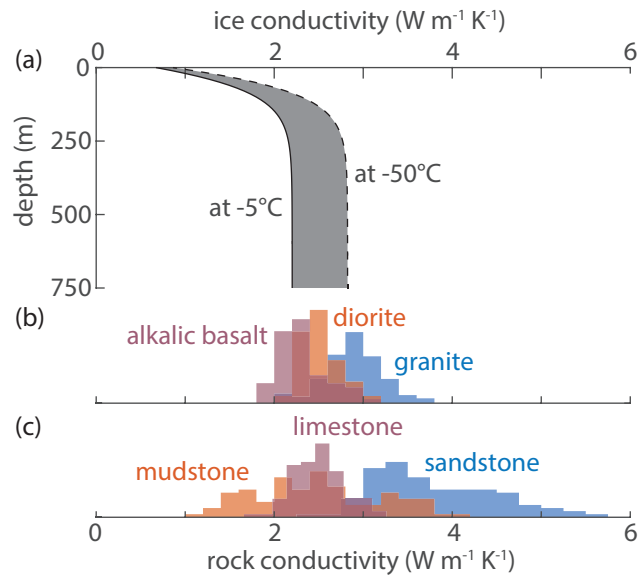
Figure 3.3: (a) Models for the thermal conductivity of ice (see Appendix A). (b) Distribution of thermal conductivities for selected igneous rock types (S. Jennings 2019, and references therein). (c) Distribution of thermal conductivities for selected sedimentary rock types (Fuchs et al. 2013).

Bedrock

The vast array of rock compositions is associated with significant variations in thermal conductivity of about 5 W m^{-1} K^{-1} (Fig. 3.3b,c). Porosity and pore fluid compositions further broaden the range of conductivities in shallow bedrock. Unweathered plutonic rocks have a relatively well-defined conductivity range from 1.8 W m^{-1} K^{-1} for alkali basalts up to 3.8 W m^{-1} K^{-1} for granites (S. Jennings 2019). By contrast sedimentary rocks have much larger variations in conductivity ranging from 1 W m^{-1} K^{-1} for mudstones to 5.25 W m^{-1} K^{-1} for quartz-rich sandstones (Fuchs et al. 2013). This large conductivity range for sedimentary rocks is related to the large range of porosities and quartz fraction. Quartz has a conductivity of 6 to 8 W m^{-1} K^{-1} whereas most common rock forming minerals have conductivities < 3 W m^{-1} K^{-1}.

In general, most rock types will have thermal conductivities higher than that of ice and those with lower conductivities are likely to be easily eroded by moving ice. In Figure 3.3, we compare the thermal conductivity of ice with that of a few common igneous and sedimentary rocks. The median thermal conductivity of the rocks shown are similar to or above the asymptotic thermal conductivity of ice, but there are a significant number

of rocks that have conductivity lower than ice. Therefore, it is important to consider the conductivity contrast between rock and ice in order to produce accurate models of heat flow.

Greenland and Antarctica are sufficiently large with lengthy and diverse tectonic histories (White et al. 2016, Harley et al. 2013). Therefore, one can reasonable expect a very large range of rock types similar to what one may find on any other continent. There are some regions where sufficiently large exposures of rocks outcrop, generally near the coasts, that can be used to model the subsurface geology allowing one to produce accurate models of thermal conductivity. There are some subglacial basins beneath Antarctica where one can expect relatively low thermal conductivity sediments juxtaposed against crystalline rocks with significantly higher thermal conductivity. One may also find that crustal sutures are regions where significant contrasts in rock types and possibly conductivity. However, there are no thermal conductivity measurements specific to rocks exposed in Antarctica.

Some thermal studies estimate thermal conductivity using various mixing formulae in combination with modal mineralogy. Another possibility is the use of bulk geochemistry to estimate thermal conductivity (S. Jennings 2019). Bulk geochemistry data advantageous as it is often widely available where bedrock is accessible. While these techniques are physically sound and frequently accurate (e.g., Fuchs et al. 2018, Ray et al. 2015, Chopra et al. 2018), they require in-depth knowledge of the bedrock and thus have limited utility for most sub-glacial heat flux studies.

In reality, the rock types are beneath much of Greenland or Antarctica are unknown. When access bedrock is not possible, empirically derived covariance relationships between thermal conductivity and other petrophysical parameters such as P-wave velocity and density may be used to estimate thermal conductivity (e.g., Hartmann et al. 2005, Sundberg et al. 2009). However, such regional settings are not geographically transferable as they typically depend on site specific parameters that are often not discernible without access to bedrock samples. A recent study by S. Jennings (2019) developed a model to estimate thermal conductivity from P-wave velocity from a global set of 340 non-porous igneous

rocks,

$$k(V_p) = 0.5822V_p^2 - 8.263V_p + 31.62, \tag{3.1}$$

with an accuracy of 0.31 W m^{-1} K^{-1}. Therefore, it may be possible to remotely estimate the thermal conductivity of bedrock without direct access to the geology.

Because of the broad range of geologic environments and thermal conductivity contrasts possible beneath ice sheets, we have chosen to illustrate the range of refractive effects on simplified geologic structures rather than focus on any particular locality.

3.3 Methods

3.3.1 Topographic solution

The topographic method developed by Lees (1910) and Lachenbruch (1968) uses a series of planes and slopes to compute the topographic perturbation to the background thermal field. However, this method is cumbersome and more difficult to implement than an alternative formulation based on Fourier series proposed by Blackwell et al. (1980). Both methods assume a homogeneous thermal conductivity medium and produce similar estimates for the topographic disturbance to the heat flow field. Therefore, due to its ease of use, we prefer the topographic method based on Fourier series.

The topographic effect on temperature at depth for a known temperature distribution along an uneven surface, $T(x,0)$, temperature can be computed by

$$T(x,z) = T(x,0) + \frac{Q}{k_r}z + \sum_{n=0}^{M} e^{-2\pi nz/\lambda}\left[A_n \cos\left(\frac{2\pi nx}{\lambda}\right) + B_n \sin\left(\frac{2\pi nx}{\lambda}\right)\right], \tag{3.2}$$

at a distance x along a profile and a depth z relative to the surface ($z(x) = 0$), where Q is the regional heat flux defined in the absence of topography, k_r is the thermal conductivity of bedrock, λ is the width of region of observation, and A_n and B_n are Fourier coefficients (Blackwell et al. 1980). The Fourier coefficients can be determined by inversion of a surface temperature at a set of known or estimated points (Henderson & Cordell 1971). The local (topographically perturbed) heat flux, $\mathbf{q}$, is then determined by Fourier's law

applied to the equation above in both the horizontal ($\hat{\mathbf{x}}$) and vertical ($\hat{\mathbf{z}}$) directions i.e.,

$$
\begin{aligned}
\mathbf{q}(x,z) = & \left\{ \frac{2\pi k_r}{\lambda} \sum_{n=1}^{M} n e^{-2\pi n z/\lambda} \left[B_n \cos\left(\frac{2\pi n x}{\lambda}\right) - A_n \sin\left(\frac{2\pi n x}{\lambda}\right) \right] \right\} \hat{\mathbf{x}} \\
& + \left\{ Q - \frac{2\pi k_r}{\lambda} \sum_{n=1}^{M} n e^{-2\pi n z/\lambda} \left[A_n \cos\left(\frac{2\pi n x}{\lambda}\right) + B_n \sin\left(\frac{2\pi n x}{\lambda}\right) \right] \right\} \hat{\mathbf{z}}.
\end{aligned}
\tag{3.3}
$$

The topographic method is attractive because it does not rely on detailed information about the bedrock if the equations are recast in terms of the thermal gradient, $\Gamma = Q/k_r$, such that the equations do not explicitly contain the thermal conductivity.

The topographic method fails to account for the presence of ice and as a result will not produce an accurate refractive effect. Therefore, we resort to solving the heat equation that incorporates a layer of ice over bedrock using a finite difference method. To demonstrate the impact of a glacial layer on the heat flux at the ice–bedrock interface, we solve the 2-dimensional, steady-state heat equation without sources,

$$
\nabla k \cdot \nabla T + k \nabla^2 T = 0,
\tag{3.4}
$$

where k and T are the conductivity and temperature, respectively, at a specific point in the medium. We solve this form of the thermal diffusion equation using successive over-relaxation applied to a finite difference approximation over a 2-D subglacial cross-section with cell sizes of $\sim 0.01 \times 0.01$ km^2 with the following boundary conditions:·

- fixed surface temperature, $T_s(x)$;

- fixed temperature at the vertical boundaries consistent with 1-D model; and

- fixed heat flux, Q, on the lower boundary.

To reduce the number of iterations and shorten convergence time, we solve a coarse grid first and progressively double the resolution until the target resolution is attained. The convergence criteria is set to 1×10^{-3} °C for the maximum temperature change of any cell during an iteration. To estimate heat flux, we apply Fourier's Law by differentiating

the temperature grid and multiplying by thermal conductivity. We then interpolate the temperature and heat flux at the ice-rock boundary.

To extend the utility of our calculations, we recast our results in terms of a non-dimensionalized temperature and heat flux. The use of non-dimensional quantities is independent of the regional heat flux and surface temperature chosen for the model and thus do not limit our results to the specific examples demonstrated in this study. The non-dimensionalized temperature, θ, and heat flux, Φ at the ice–bedrock boundary are given by

$$\theta(x) = \frac{T_b(x) - T_{b,1\mathrm{D}}(x)}{T_{b,1\mathrm{D}}(x) - T_s}, \tag{3.5}$$

$$\Phi(x) = \frac{|q_b(x)|}{q_{b,1\mathrm{D}}}, \tag{3.6}$$

where T_b and $|q_b|$ are the magnitude of temperature and heat flux at the boundary, and $T_{b,1\mathrm{D}}$ and $q_{b,1\mathrm{D}}$ is the boundary temperature and heat flux for the 1-D case associated with each vertical column across the section. For our models, $q_{b,1\mathrm{D}}$ is equal to the regional heat flux, Q, and $T_{b,1\mathrm{D}} = T_s + Qh/k_i$, where h is the ice thickness.

In order to emphasize the effect of thermal refraction, we have made a number of assumptions to the heat flux equation. The above formulation ignores the influence of basal shear heating that is likely to dominate in regions with significant ice transport. In such cases, the geothermal heat flux contributions to the ice sheet are probably insignificant. We also ignore advection within the ice, which will affect the upper portion of the geotherm resulting in nearly isothermal temperatures at the surface (e.g., Dahl-Jensen et al. 1998). As a result, the top of our models could be considered to begin at the point for which the ice has reached a conductive thermal profile. Advection near the base of thick ice may also have an effect and would normally be taken into account during modeling. We also ignore latent heat effects in instances where the models predict temperatures in excess of the melting point of ice (e. g., Fig. 3.1). Such temperatures can be considered as melt potential instead, where in reality, temperatures would be fixed to the melting temperature at the base of the ice and reducing temperatures within the overlying glacial

column. Because we are simply demonstrating the effect of thermal refraction, it is the relative—not absolute—temperature difference that is important. The last assumption we make is that the crust contains negligible heat generation whereas continental crust contains significant radioactive heat generation that contributes to curvature in the geotherm (Chapman 1986). However, the effect is small enough in the shallow Earth that it can be reasonably ignored.

3.3.2   Model geometries

To demonstrate how thermal refraction effects the flow of heat in glacial environments we construct the following models: (1) a Gaussian-shaped valley and (2) a subglacial geologic contact below a flat horizontal ice sheet. We have chosen these two basic geometries because they can be easily tailored to produce a wide range of common geologic and geomorphic features. To prevent boundary effects on calculations, model domains were typically set to approximately 10 times the width and depth of the subglacial topographic features.

Gaussian valley

A Gaussian-shaped sub-glacial valley is presented to illustrate the range of thermal refractive effects in response to changes in thermal conductivity and geometry (e.g. Fig. 3.4a). The valley is constructed by assigning a regional ice sheet thickness, h, a width, w, and a depth, d (Fig. 3.4a). The ice is assigned a uniform thermal conductivity, k_i, of 2 W m^{-1} K^{-1} and the bedrock conductivity is constant for each model.

Subvertical geological contact

Refraction also happens where there is no topography along the ice–bedrock interface when a geological contact juxtaposes rock types with differing thermal conductivity (Fig. 3.4b). To demonstrate this effect, we present a simple model for a geological contact below the ice. The model as shown in Figure 3.4b can be thought of as a fault-bounded sedimentary basin with a thickness, d, and an acute contact angle δ measured from the horizontal. In
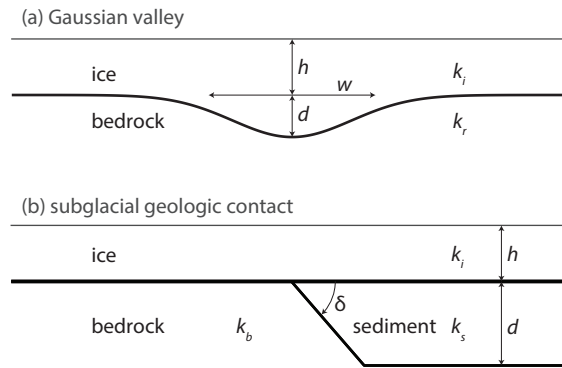
Figure 3.4: Model setup and parameters used to model thermal refraction. Two classes of models are explored: (a) subglacial valley in a Gaussian shape and (b) subglacial contact beneath a flat subglacial surface.

this case, there are two bedrock conductivities, one for the sedimentary basin, k_s and one for the surrounding bedrock, k_b.

3.4   Results

3.4.1   Gaussian valley

The results of the finite difference solution are presented in Figure 3.5 for a bedrock conductivity of 1.5 and 3 W m^{-1} K^{-1}, respectively. When $k_i > k_r$, heat preferentially flows into the valley as it represents the easiest path to the surface (Fig. 3.5a). As a result, the isotherms bend away from the valley creating higher temperatures in the ice above the valley and lower temperatures in the bedrock below. However, relative to a series of one-dimensional vertical temperatures stitched across the profile, temperature is higher both above and below the valley (Fig. 3.6a). The valley flanks have anomalously low temperatures with slightly negative side lobes. The shape of the heat flux anomaly is similar to the temperature anomaly (Fig. 3.6b).

When the conductivity contrast is reversed, $k_i < k_r$, the heat flux and temperature anomalies both reverse polarity (Fig. 3.5). In this scenario, the isotherms bend toward the valley as heat flows around the valley.

Refraction can reduce or increase the difference between the valley flank and valley base temperatures, but temperatures will always be higher at the valley base than the flanks
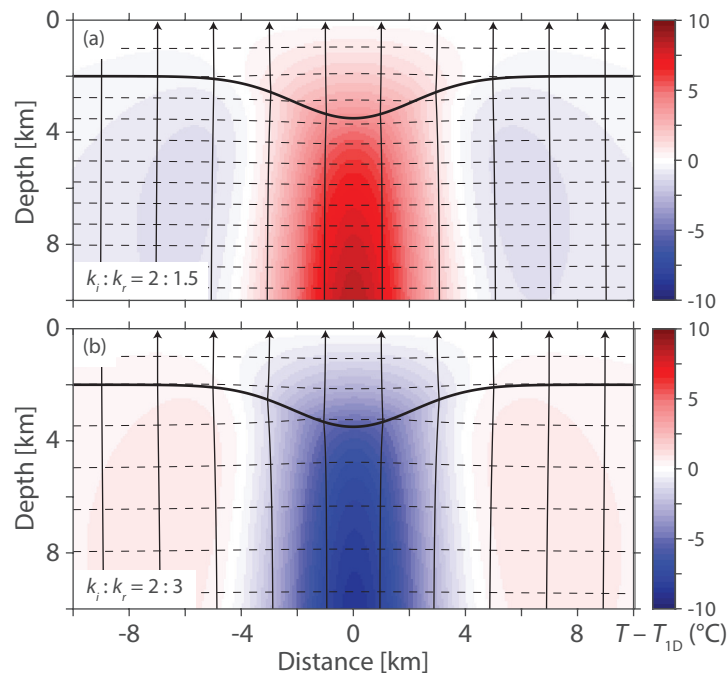
Figure 3.5: Thermal refraction due to a Gaussian-shaped valley. The models are computed for a thermal conductivity contrast of ice to rock, $k_i : k_r$, of (a) 2:1.5 and (b) 2:3. Geometric parameters h, w, and d are used to define the ice thickness, valley width, and valley depth, which are 2, 6, and 1.5 km, respectively. Isotherms are indicated by dashed lines and vector streamlines indicate the path of heat flow to the surface. The temperature anomaly is shown in the background, computed by subtracting the 1-D temperature field at each point along the profile from the model temperatures (numerator of Equation 3.6).
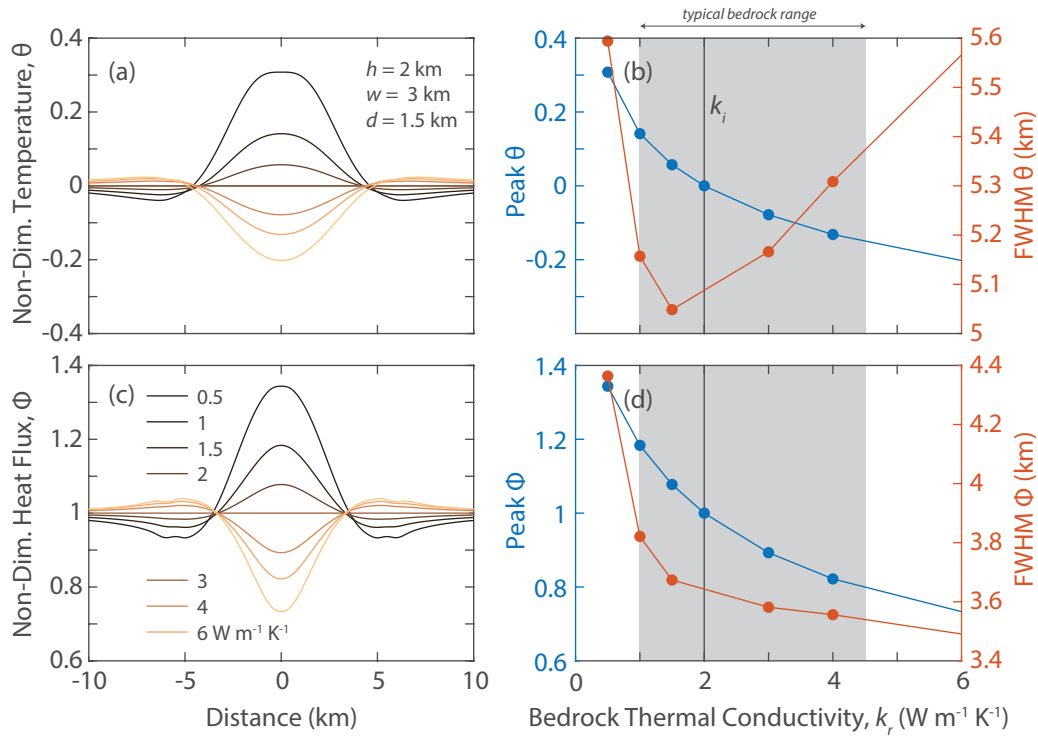
Figure 3.6: Basal temperature anomalies (a,b) and basal heat flux anomalies (c,d) across a Gaussian-shaped valley as a function of bedrock thermal conductivity. The models are computed for the same geometry in Fig. 3.5. (a,b) Profiles at the ice–bedrock interface. (c,d) The value of the central peak (blue) and full-width at half maximum (orange). The value of ice conductivity, k_i, is indicated by the vertical line and grey field indicates the range of conductivity for most rocks (c,d). Non-dimensional temperature and heat flux definitions are given in Equation 3.6. Because of a heat flux discontinuity at the boundary, the heat flux is estimated by averaging the flow just above and below the boundary to reduce numerical noise.

as a result of a positive thermal gradient with depth. However, the non-dimensionalized heat flux anomaly is related to an increase or decrease in temperature with respect to the vertical 1D temperature field, which preserves the sign of the absolute heat flux anomaly.

The magnitude of the basal temperature and basal heat flux anomalies vary smoothly as a function of the thermal conductivity contrast between the ice and rock (Fig. 3.6). For the bedrock conductivities chosen for this model, the basal temperature anomalies range from -0.2 to 0.3. The basal heat flux anomalies can vary between 0.7 to 1.3 as a fraction of the regional BGHF. However, this range is probably more extreme than most settings beneath thick ice, which are more likely to range from -0.15 to 0.15 for basal temperature anomalies and from 0.8 to 1.1 for basal heat flux anomalies (Fig. 3.6b,d).

The geometry of the Gaussian basin has an effect on the basal thermal anomalies. We computed 112 separate models with varying bedrock conductivity, ice thickness, valley width, and valley depth to examine the effect of geometry on the basal thermal anomalies (Fig. 3.7). An increase in ice thickness and valley width reduce the magnitude of the refraction effect. However, the reduction in non-dimensionalized magnitude is negligible as a function of ice thickness within the typical range for most rock types. In contrast to the other geometric parameters, an increase in valley depth results in an increase in the severity of the refractive effect.

3.4.2   Subglacial geologic contact

For the subglacial model presented in Figure 3.8 with $k_b > k_s$, the heat preferentially flows around the basin near the subvertical contact with the bedrock. This contrast results in a decrease in heat flux at the western edge of the basin and an increase in heat flux through the bedrock to the west of the contact. Isotherms however, result in higher temperatures in the basin but lower than expected from a 1D model. On the bedrock side, temperatures are increased relative to a 1D model. Though the disturbances to the thermal field are largest below the ice, there is an effect on temperature and heat flux within the ice sheet itself.

As with the valley model, model geometry has a significant effect on the thermal
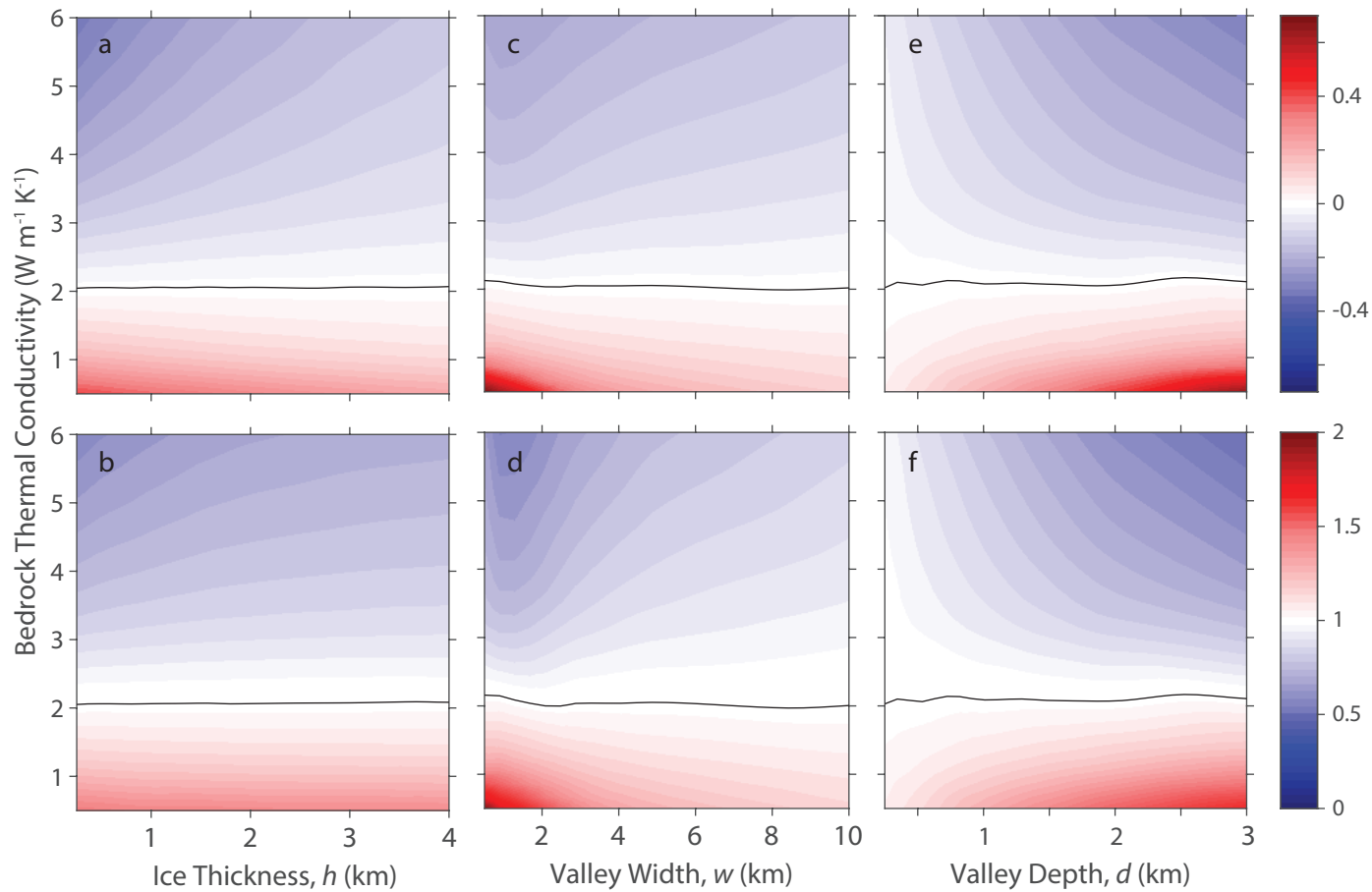
Figure 3.7: Basal temperature anomalies (a,c,e) and basal heat flux anomalies (b,d,f) across a Gaussian-shaped valley as a function of bedrock thermal conductivity and model geometry. Geometry parameters are defined in Figure 3.5. Each pair of temperature heat flux plots are computed with geometry and ice conductivity given in Figure 3.5. The black contour in each plot identifies the estimated zero anomaly.
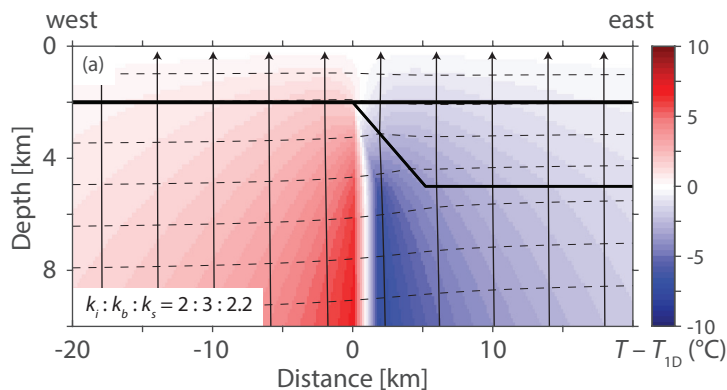
Figure 3.8: Thermal refraction due to a geologic contact beneath an ice sheet. The model is computed for a thermal conductivity contrast of ice to the two bedrock layers, $k_i : k_b : k_s$, of 2:3:2.2. Geometric parameters h, d, and δ are used to define the ice thickness, basin depth, and contact dip angle, which are 2 km, 3 km, and 60°, respectively. Isotherms are indicated by dashed lines and vector streamlines indicate the path of heat flow to the surface. The temperature anomaly is shown in the background, computed by subtracting the 1-D temperature field at each point along the profile from the model temperatures (numerator of Equation 3.6).

anomalies. In Figure 3.9, we compute the thermal anomalies for a variety of contact angles using the same conductivities and basin depth as in Figure 3.8. The anomalies are asymmetric as a result of the both the finite depth of the basin and the subvertical dip. The extrema slowly change with the dip angle except at low dip angles ($<10°$) that rapidly approach zero (Fig. 3.8). The peak to peak distance also increases dramatically at low angles (Fig. 3.9c,d). The basal heat flux anomalies and basal temperature anomalies are as large for the fault model as similar bedrock conductivity models for the Gaussian valley.

The conductivity ratio between the basin and bedrock determines the magnitude of the thermal anomalies, not the absolute conductivities. Figure 3.10 shows the results for 112 subglacial contact models computed with a range of basin and bedrock thermal conductivities. Lines of constant magnitude for both temperature and heat flux anomalies (colors in Fig. 3.10) follow lines of constant $k_s : k_b$ ratio, which demonstrates that the magnitude of the refraction effect is independent of the absolute conductivities. For $k_s : k_b$ ratios <1, the maximum basal temperature anomaly and basal heat flux anomaly are on the bedrock side of the contact where as the maximum and minimum swap sides when $k_s : k_b$ is >1, i.e., the positive anomaly is located on the conductive side of the contact.
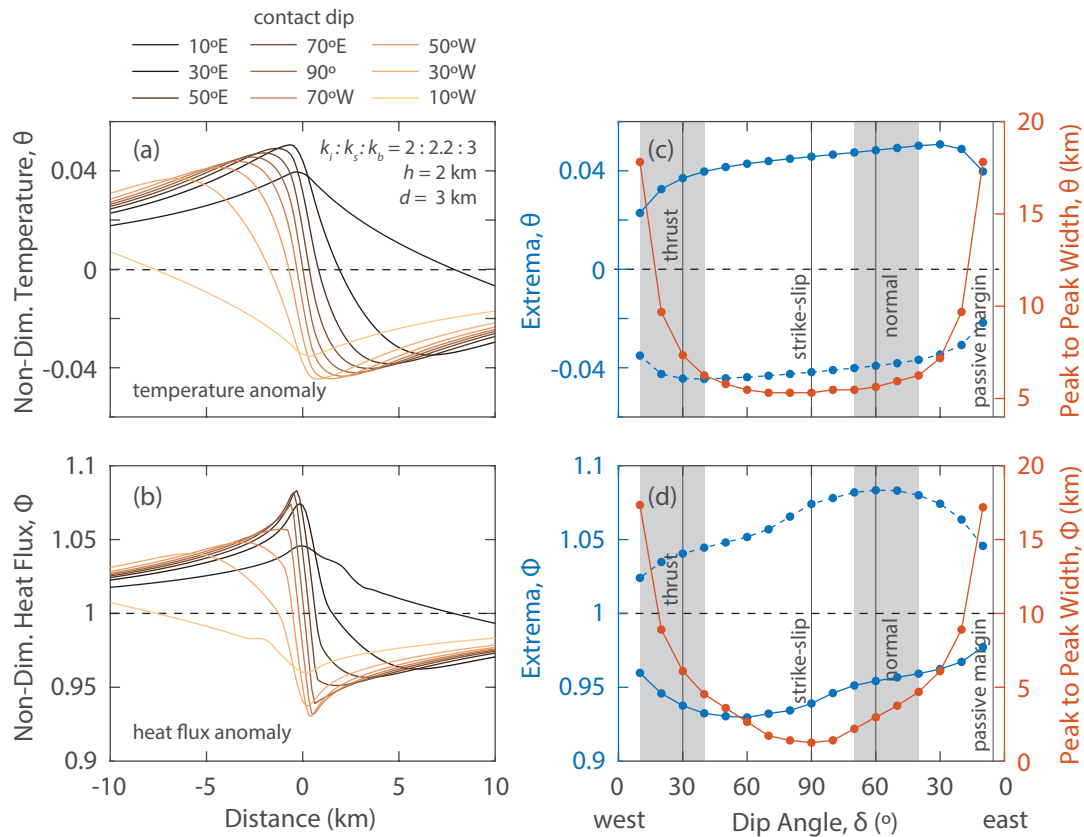
Figure 3.9: Basal temperature anomalies (a,c) and heat basal flux anomalies (b,d) across a geologic contact as a function of contact dip angle. The geometry is defined in Figure 3.8, where dip angle is measured as an acute angle to the surface with dip direction denoted as to the east (right) or west (left). Although geologic contacts can be rotated into any angle through tectonic processes, we have labeled the common angles associated with unrotated fault types and passive margin slopes.
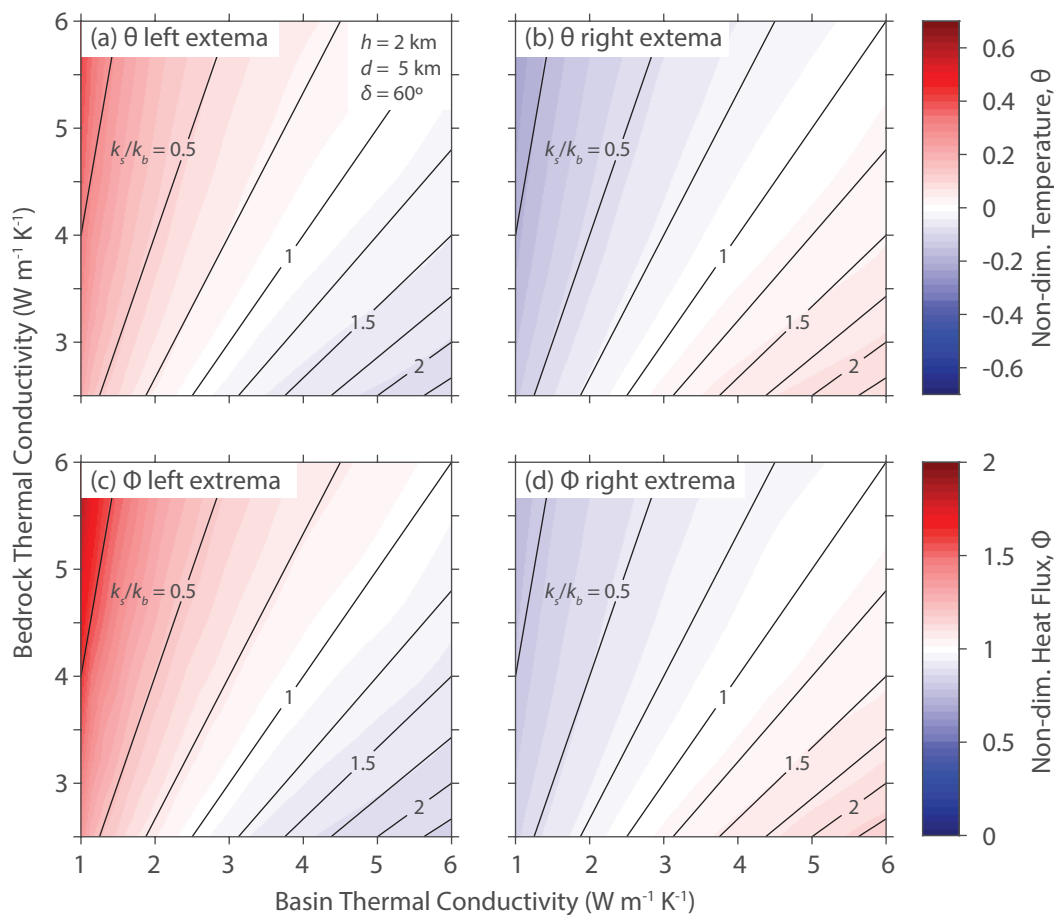
Figure 3.10: Basal temperature anomalies (a,b) and basal heat flux anomalies (c,d) across a geologic contact as a function of bedrock and sedimentary basin conductivity. The geometry is shown in Figure 3.8. Normalized temperature (a,b) and heat flux (c,d) extrema for a geologic contact with 60° dip. Contours are drawn for conductivity ratios of basin (k_s) to bedrock (k_b). Ice conductivity is 2 W m^{-1} K^{-1} for both models. Extrema on the bedrock side of the contact (a,c) and basin side (b,d). The black contour in each plot identifies the estimated zero anomaly. Each pair of temperature heat flux plots are computed with geometry and ice conductivity given in Figure 3.8.

3.5 Discussion

3.5.1 Topographic vs. finite difference solutions

To compare the topographic model and the finite difference solution, we have produced a subglacial topographic profile across a ridge and hill (Fig. 3.2). The topographic method is computed with a constant surface temperature as implied by the model produced by van der Veen et al. (2007), though it is unlikely to be true. Isotherms from the topographic method are expanded beneath the ridge and heat flux is decreased whereas below the valley isotherms are compressed and heat flux is increased (Fig. 3.2a). The overall topographic effect on heat flux predicts large local variations of nearly 50 to 175% compared to the regional heat flux (Fig. 3.2b).

The finite difference solution will be dependent upon the thermal conductivity of the ice and bedrock, but will result in a smaller disturbance to the heat flux field at the base of the ice. In Figure 3.2, we use a thermal conductivity contrast of 2:3 between the ice and bedrock layers. In this case, the polarity of the anomaly is reversed relative to the topographic solution and considerably smaller in magnitude, creating anomalies no larger than ±25%. If the conductivity contrast is reversed the same polarity can be obtained for the finite difference solution, but the thermal conductivity contrast would need to be at least 10:1 to obtain similar magnitude anomalies as the topographic solution. Such a case can be easily rejected as geologically unrealistic.

The polarity of thermal anomalies computed using the topographic solution can be reversed only by two unrealistic scenarios: a negative regional heat flux or by imposing certain surface temperature profiles. A negative heat flux, heat flowing from the surface into the Earth, is generally unreasonable except as a result of diurnal and climatic warming—both extend less than a few 10's of meters into the subsurface and are transient. Changing the surface temperature profile is possible, but requires a priori knowledge. If the surface temperature is set properly, the topographic solution will be the same as the finite difference solution only when there are no subsurface variations in thermal conductivity. Because we rarely know the basal temperature along the glacier bed a priori, this

is unrealistic.

The topographic solution applied to a subglacial boundary also fails to accurately predict basal heat flux anomalies in many geological settings. The finite difference solution predicts zero thermal anomalies when thermal conductivity of ice and bedrock are equal, irrespective of the bed topography (Fig. 3.7). The topographic solution will also not yield a thermal anomaly where there is no bed topography, but a lateral thermal conductivity contrast exists. As discussed above, the finite difference solution predicts significant thermal anomalies in such cases (Fig. 3.8).

3.5.2   Implications for ice viscosity and subglacial melting

Both the viscosity of ice sheets and the potential for melting are effected by temperature and heat flux anomalies created by thermal refractive effects. As our models predict basal temperature anomalies that extend into glaciers and ice sheets, we expect an effect changes to viscosity and melt potential. For instance, glaciers weaken in response to heating (Perol & Rice 2015) and our models predicts both heating and cooling in response to thermal refraction effects. As a result, we expect refraction to stabilize glaciers in some regions while weakening in others. While our discussion below focuses on the potential for melting, the effects have a broader effect on viscosity.

Our valley models suggest that subglacial melting is easier for some geometries and conductivity contrasts than others. Melting will always occur most readily at the base of a valley where temperatures are highest, but deep, narrow valleys where the thermal conductivity of the bedrock is less than ice will result in enhanced melting (Figs. 3.1, 3.6 and 3.7). Conversely, valleys where the bedrock conductivity is higher than the ice will result in a reduction of melt potential (Figs. 3.1 and 3.6). The latter model is in direct contrast to the predictions by the topographic method. Because thermal conductivity is generally greater in bedrock than ice, we suggest ice sheets will more likely be stabilized by topographic depressions (Fig. 3.2).

Though we have generally worked in non-dimensional units, we can place the magnitude of temperature and heat flux anomalies in context. In East Antarctica and Green-

land where the ice is generally 2 km thick or above, 40 to 50 mW m^{-2} is a reasonable heat flow for similar aged terranes (Lucazeau 2019), and for a bedrock conductivity of 3 W m^{-1} K^{-1} ($\theta = 0.1, \phi = 0.9$), the estimated heat flux anomaly is -4 to -5 mW m^{-2} and temperature anomalies 2 to 2.5 °C. For bedrock conductivities of 4 W m^{-1} K^{-1}, the anomalies would be twice these values. While these numbers are not large, they could be sufficient to suppress melting and increase viscosity. Likewise, for conductivities lower than ice, the magnitudes will be similar, but opposite in sign.

Subglacial ridges have thermal anomalies opposite in polarity to subglacial valleys (Figure 3.2). If melting were to occur, it would happen on the lower slopes of the high topography where thermal conductivity of the bedrock is less than the ice. However, the potential is likely to be low because the basal temperature anomaly side lobes have relatively small magnitudes.

Whereas melting is more likely in some valley scenarios, the mere presence of a subglacial geologic contact raises the melt potential even in the presence of no subglacial topography. A positive temperature anomaly is created irrespective of a higher thermal conductivity in the bedrock or basin, always creating the positive anomaly on the conductive side of a contact (Fig. 3.10a,b). Furthermore, the magnitude of the temperature anomaly is relatively constant for all but shallow dip angles <20°, raising the potential for melting under a wide variety of geometries (Fig. 3.9). Such short wavelength variations in viscosity could results in folding of the ice sheet as it flows over such contacts (Bons et al. 2016).

There is a potentially large difference in the spatial scale of melting and viscosity contrasts for the cases discussed above. Melting of ice beneath topographic lows is likely to be constrained spatially relative to a narrow region at the base of a valley (Fig. 3.6). Next to topographic highs, the spatial scale of broader but likely to be small in magnitude. Above geologic contacts, temperatures can remain significantly elevated for relatively large distances >10 km across strike on the high conductivity side (Fig. 3.9).

In most cases, the refraction effect will occur in regions where melting will not occur but viscosity will still be affected. In regions where melting occurs, our temperature

estimates will be incorrect because melting will keep temperatures fixed at the melting point. In such cases, the melt rate can be estimated from the difference between the estimated BGHF and the heat flux at the surface,

$$\frac{dh}{dt} = \frac{k_i \Delta T_e}{\rho_i h L},$$
(3.7)

where ΔT_e is the excesses temperature (i.e., estimated temperature anomaly above the ice's melting point at the base of the ice sheet), k_i and ρ_i are the conductivity and density of the ice, h is the thickness of the ice sheet, and L is the latent heat.

3.6   Conclusions

We demonstrate the effect of heat refraction at the base of ice sheets in the presence of subglacial topography and above geological contacts. Previously proposed topographic-based models for heat flux across a subglacial boundary are physically incorrect as they make incorrect assumptions about the thermal conductivity of ice. In many cases—specifically where bedrock is more conductive than ice—heat flux and temperature will be reduced above topographic depressions, the opposite as predicted by the topographic effect. Thus, it is necessary that future thermal model of ice sheets incorporate lateral variations in thermal conductivity and the resulting thermal refractive effect. Thermal refraction can occur over spatial scales smaller than resolvable by remote sensing estimates (e.g., seismic and Curie depth), but create heat flux and temperature anomalies sufficient to create subglacial melting. Subglacial melt potential may actually be decreased in valleys with thermally conductive bedrock relative to the overlying ice sheet. Changes in melt potential can increase, and viscosity decrease, on the conductive side of geologic contacts even when bed topography is flat. Likewise, ice viscosity is affected by thermal refraction of heat and therefore may influence ice flow velocities near geologic contacts and subglacial topographic features. While our models of ice sheets are simplistic, they illustrate the need to include refractive effects created by realistic geology into future glacial models. Including thermal refractive effects will improve the prediction of subglacial melting and

ice viscosity where heat flux is dominated by geothermal heat flux rather than shear heating at the bed. We suggest that contrary to previous studies, topographic depressions may be regions where thick ice is more stable than previously assumed. The implications in this study are not limited to glacial environments but are applicable to any environment that contains variations in thermal conductivity.

Statement of Authorship

Title of Paper	Compositional controls on the thermal conductivity of igneous rocks and a model for the conductivity of Antarctic crust
Publication Status	☐ Published ☐ Accepted for Publication ● Submitted for Publication ○ Unpublished and Unsubmitted work written in manuscript style
Publication Details	

Principal Author

Name of Principal Author (Candidate)	Simon Robert Willcocks
Contribution to the Paper	Preformed laboratory work, modeling results, generated figures and wrote main paper.
Overall percentage (%)	80%
Certification:	This paper reports on original research I conducted during the period of my Higher Degree by Research candidature and is not subject to any obligations or contractual agreements with a third party that would constrain its inclusion in this thesis. I am the primary author of this paper.
Signature	Date 17/12/2022

Co-Author Contributions

By signing the Statement of Authorship, each author certifies that:

i. the candidate's stated contribution to the publication is accurate (as detailed above);

ii. permission is granted for the candidate in include the publication in the thesis; and

iii. the sum of all co-author contributions is equal to 100% less the candidate's stated contribution.

Name of Co-Author	Derrick Hasterok
Contribution to the Paper	Conceived the idea, proofread paper and figures, generated thermal conductivity map of Antarctica
Signature	Date 20 Nov 2022

Name of Co-Author	Samuel Jennings
Contribution to the Paper	Demonstated equipment and computation softwere. Was also a major source of inspiration for paper.
Signature	Date 28/11/2022

Please cut and paste additional co-author panels here as required.

Statement of Authorship

Title of Paper	Compositional controls on the thermal conductivity of igneous rocks and a model for the conductivity of Antartic Crust
Publication Status	☐ Published ☐ Accepted for Publication ● Submitted for Publication ☐ Unpublished and Unsubmitted work written in manuscript style
Publication Details	

Principal Author

Name of Principal Author (Candidate)	Simon Robert Willcocks
Contribution to the Paper	Prefromed laboratory work, modeling results, genrated figures and wrote main paper.
Overall percentage (%)	80%
Certification:	This paper reports on original research I conducted during the period of my Higher Degree by Research candidature and is not subject to any obligations or contractual agreements with a third party that would constrain its inclusion in this thesis. I am the primary author of this paper.
Signature		Date	17/12/2022

Co-Author Contributions

By signing the Statement of Authorship, each author certifies that:

    i.   the candidate's stated contribution to the publication is accurate (as detailed above);

    ii.   permission is granted for the candidate in include the publication in the thesis; and

    iii.   the sum of all co-author contributions is equal to 100% less the candidate's stated contribution.

Name of Co-Author	Jacqueline Halpin
Contribution to the Paper	Supplied samples and measured major element compositions
Signature		Date	6/12/2022

Name of Co-Author	Jessica Walsh
Contribution to the Paper	Measured major element compositions
Signature		Date	28/11/2022

Please cut and paste additional co-author panels here as required.

Chapter 4

Compositional controls on the thermal conductivity of igneous rocks and a model for the conductivity of Antarctic crust

Abstract

Thermal conductivity models of the lithosphere are often oversimplified, lacking realistic lateral and vertical variations that distort the temperature field and affect geothermal heat flux estimates. In this study, we employ methods for estimating thermal conductivity within the crust using compositional analyses and seismic velocities and apply them to the continent of Antarctica. We measured the thermal conductivity and density of 49 Antarctic meta-igneous rocks and 4 quartzites using an optical thermal conductivity scanner. The results were combined with >1000 additional global samples, predominately igneous lithologies, to produce separate thermal conductivity models as a function of major elements, modal mineralogy and normative mineralogy. Despite a skew in the residuals, all compositional models result in similar misfit ($\sim$0.4 W m^{-1} K^{-1}) with 95 % of samples within $\pm$20 % of measured conductivities. The major element model is used to

estimate the conductivity of ∼7,000 Antarctic samples with most estimates between 1.8 and 3.0 W m^{-1} K^{-1}. Additionally, we produce a 3D model of thermal conductivity for the Antarctic crust using an empirical seismic velocity–conductivity model. The 3D model shows a general decrease in conductivity with depth and an anomalously high thermal conductivity beneath the South Pole. The predicted lateral variations can be applied to existing geophysical proxy estimates of lithospheric temperatures to improve geothermal heat flux (GHF) models of Antarctica.

4.1   Introduction

Geothermal heat flux (GHF) is an important boundary condition that affects the mass transport of and melting of ice sheets (e.g. Reading et al. 2022). Many studies attempt to estimate GHF using a variety of geophysical proxies and statistical methods (An et al. 2015, Martos et al. 2017, Lösing et al. 2020, Shen et al. 2020, Stål et al. 2021). However, the thermal properties of the Antarctic crust are poorly constrained due to limited accessibility of samples, which results in large uncertainties in GHF that are often not incorporated into the reported uncertainties. One such property, thermal conductivity, is needed to determine the heat flux from thermal gradients (Chapman 1986). Lateral variations in thermal conductivity also have the potential to create refractive effects that distort thermal fields (Swain 2019). These distortions can create heat flux anomalies of ±20 % and temperature anomalies of ±15 % around the regional values into the base of an ice sheet (Willcocks et al. 2021).

Thermal conductivity cannot be remotely sensed; therefore, we must rely on estimates of thermal conductivity. Lösing et al. (2020) was able to generate a map of estimated thermal conductivity along the Antarctic peninsular by using maps of heat production, Curie depth as well as their own model of geothermal heat flux. However, most studies of Antarctic GHF, i.e., those that use forward modelling approaches, use assumed values based on a uniform crustal structure (Maule 2005, An et al. 2015, Martos et al. 2017), but there can be significant lateral variations in thermal conductivity depending on the composition of the crust (S. Jennings 2019). Statistical methods can provide a robust

alternative to the need for thermal conductivity estimates by using statistical correlations between geophysical characteristics and GHF trained on one or more continents and then applied to Antarctica (Shen et al. 2018, Lösing et al. 2020, Stål et al. 2021). Such methods tend to revert to the mean value of the GHF distribution and do not accurately capture the lateral variability of GHF as a result. Hence it is critical to have accurate spatial models of thermal conductivity variations in order to improve GHF estimates.

One way to improve thermal conductivity estimates is by exploiting its relationship with physical properties that are easier to sense remotely (e.g., density and seismic velocity). For plutonic rocks, composition is the primary factor for controlling thermal conductivity (Clauser & Huenges 1995). Additional factors such as temperature, pressure (Horai & Susaki 1989), anisotropy (Davis et al. 2007), and density (Veiseh et al. 2009) can affect the overall thermal conductivity of plutonic rocks. With many factors affecting thermal conductivity, constructing a predictive model requires observations on a broad array of rock samples. S. Jennings (2019) compiled thermal conductivities, densities and compositions (both chemistry and mineralogy) of 340 plutonic rocks. Their study developed, via linear regression, a relation between thermal conductivity and composition.

In this study, we measure the thermal conductivity and density of 49 Antarctic rock samples. Combining our observations with an updated database, we model the effect of composition on thermal conductivity and update empirical relationships for conductivity with density and seismic velocity. We apply the velocity–conductivity relationship to a tomographic model of the Antarctic crust producing a 3D model of thermal conductivity that can be used to improve estimates of GHF.

4.2 Background

4.2.1 Existing data

Most studies that examine the effect of composition on thermal conductivity have explored the mineralogical influence (Brigaud & Vasseur 1989, Clauser & Huenges 1995, Ray et al. 2006, Hasterok & Chapman 2011, Fuchs et al. 2018, Chopra et al. 2018, Ye et al. 2022).

This method is required to predict thermal conductivity for low-porosity crystalline rocks, as minerals themselves each have an intrinsic conductivity that contribute to the bulk conductivity (Clauser & Huenges 1995). However, modal mineralogy is not often reported with studies of rock samples making it difficult to predict conductivities for a large number of samples en masse. Furthermore, there are thousands of rock forming minerals, though only a few dozen are common, and fewer still have been sufficiently analyzed for thermal conductivity (Marfunin 2011).

In contrast, major element geochemistry is commonly reported for a wide range of rock types, making it ideal for estimating thermal conductivity. Some studies have collected major element analyses along with thermal conductivity (Table 4.1), though not to develop predictive models of conductivity. Only S. Jennings (2019) has used major element chemistry to develop a method for predicting thermal conductivity of igneous rocks. While this method is not as accurate as using mineralogy, the differences of thermal conductivity estimates are within typical uncertainties ($\pm 10\%$ S. Jennings 2019).

We have compiled the thermal conductivity, major oxide, and modal mineralogy of 1,178 rock specimens. The original database compiled by S. Jennings (2019) included 462 samples ranging in composition from ultramafic to felsic and predominantly consists of igneous and meta-igneous samples with low porosity (Table 4.1). There are five meta-sedimentary samples, all quartzites, that are included to extend the SiO_2 range to higher values than typically found within igneous rocks (Figure 4.1). We have added 716 data from an additional three studies (Ray et al. 2021, Coletti et al. 2021, Rhodes et al. 2013). These new studies increase the number of mafic samples, which previously represented less than 10% of the Jennings et al. database. S. Jennings (2019) was careful to exclude highly foliated samples from their work to reduce the potential for thermal conductivity anisotropy. In contrast, many of the data from Rhodes et al. (2013) are foliated gneisses and were anisotropic. They made multiple measurement in different locations on the sample to estimate a bulk conductivity.

Previous observations of conductivity demonstrate a systematic variation with major

Table 4.1: A brief description of the samples used to develop compositional-based conductivity models in this study. Sample quantities in bold have been added to the existing database as part of this study.

Study	No. Samples	Description
Horai & Baldridge (1972)	11	assorted plutonic rocks ranging from ultramafic to felsic originating in the US and Canada
Maqsood et al. (2004)	19	granites from the Shewa–Shahbaz Garhi volcanic complex, Pakistan
Ray et al. (2015)	26	Archean granitoids and gneiss from Bundelkhand Craton, central India
Chopra et al. (2018)	21	Archean granitoids (granite to diorite) from Bundelkhand Craton, central India
Fuchs et al. (2018)	45	plutonic origin ranging from granite to gabbro; multiple sites globally
S. Jennings (2019)	340	mostly plutonics ranging from granite to peridotite, 9 volcanics and 4 quartzites; multiple sites globally
Ray et al. (2021)	**34**	alkali/biotite granite and granodiorite/metasomatised granodiorite from India sheild Archaean cratons
Coletti et al. (2021)	**7**	granites, tonalites, syenite and gabbro from Italian quarries
Rhodes et al. (2013)	**675**	plutonic, volcanic and mid- to high grade metamorphic rocks from Connecticut (242 samples) and Massachusetts, USA (432 samples)
This study	**49**	plutonic and meta-igneous rocks and five quartzites from East Antarctica

element composition S. Jennings (2019). The clearest trend is an increase in conductivity with weight percent SiO_2 (Figure 4.1). As many elements (Al_2O_3, FeO, MgO, and CaO) show some correlation with SiO_2, there are also variations in thermal conductivity with these major oxides (Figure 4.1). S. Jennings (2019) utilised these trends to develop a multilinear regression between thermal conductivity and major oxide compositions. We use these same trends in this study with the addition of a larger database (n = 1,178 rock specimens).

4.2.2   Antarctic samples

Compared with other continents, bedrock samples from the Antarctic region are difficult to source due to the remoteness and coverage by a 3 to 4 kilometer thick ice sheet (Fretwell et al. 2013). Current thermal conductivity measurements on the continent have mostly
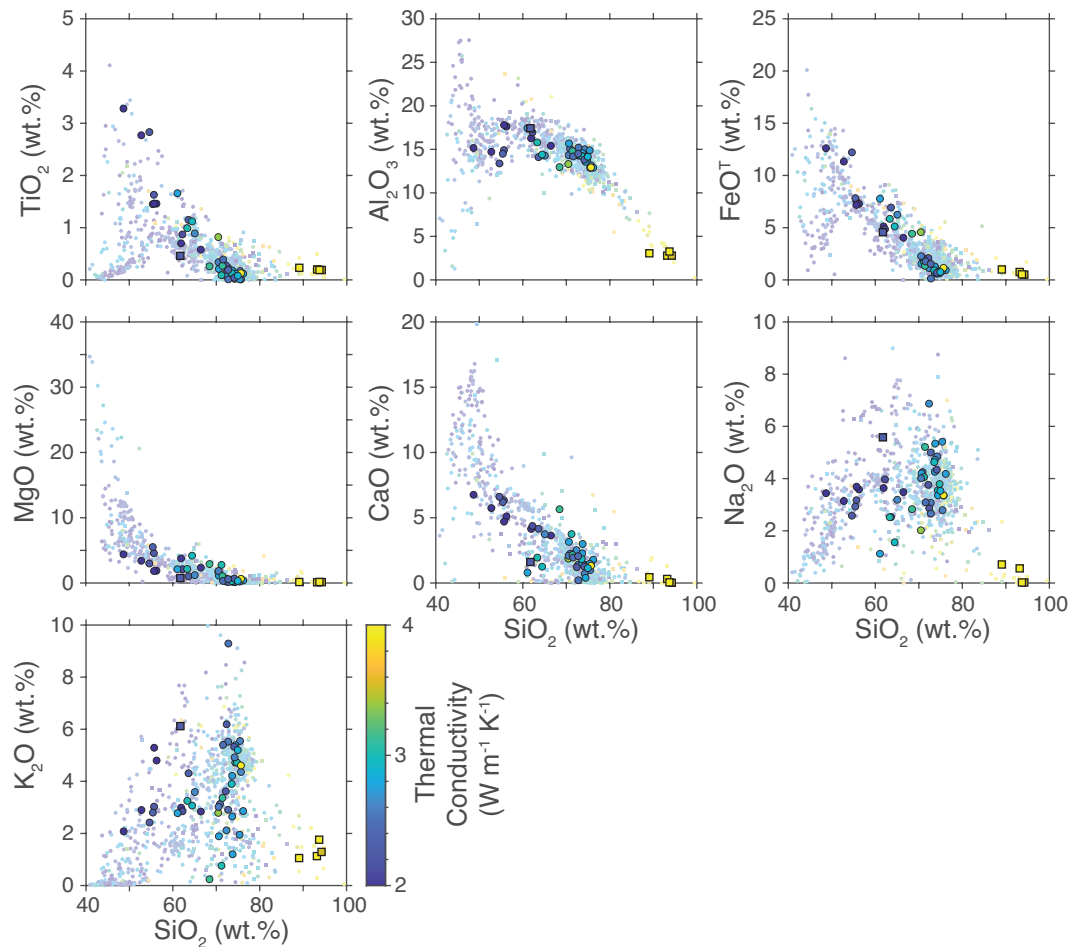
Figure 4.1: Harker diagrams showing the distribution of sample compositions with respect to weight percent SiO_2, normalized to account for loss on ignition. Samples are colored by thermal conductivity. Antarctic samples are displayed with larger marker sizes with a black outline. Round markers indicate igneous and meta-igneous samples and squares indicate meta-sedimentary samples.

been made on the ice (Pringle et al. 2007, Cameron & Bull 2013) or subglacial sediment rather than lithified rocks (Fisher et al. 2015, Begeman et al. 2017). Although there is no reason to suspect that thermal conductivity will behave systematically differently within Antarctica, we have selected 49 samples to measure thermal conductivity (Table 4.2). Samples were previously collected from exposed outcrops in East Antarctica and archived at The University of Adelaide and The University of Tasmania. There are 44 igneous and meta-igneous samples, most high-grade gneisses, and five meta-sedimentary samples, all quartzites. The grain size varies from fine to coarse, with most fine to medium grained. Individual mineral grains are anhedral in all of the samples. Three-quarters of the samples are light coloured consistent with their predominantly felsic to intermediate composition.

Twenty-three have no clear foliation, four have weak foliation and the remainder foliated and often layered.

[tbh]

Table 4.2: Samples chosen for new density and thermal conductivity (TC) analyses from the Australian Antarctic Territory.

Sample ID	Reference	Locality	Long.	Lat.	Lithology Reported[a]	Protolith[b]	Density (kg m⁻³) dry μ	σ	saturated μ	σ	φ[c] %	TC (W m⁻¹ K⁻¹) dry μ	σ	saturated μ	σ	A[d]
A180181	Sanchez (2021)	Alligator Island	97.7	-66.6	gneiss	granite	2611	7	2618	7	0.44	2.58	0.04	2.79	0.04	1.03
A191192	Sanchez (2021)	Alligator Island	97.7	-66.6	gneiss	granodiorite	2604	7	2631	7	1.67	1.94	0.06	2.44	0.06	0.99
A199200	Sanchez (2021)	Alligator Island	97.7	-66.6	gneiss	diorite	2667	7	2682	7	0.88	1.82	0.07	1.93	0.14	1
A207208	Sanchez (2021)	Alligator Island	97.7	-66.6	orthogneiss	granite	2620	7	2630	7	0.63	2.22	0.06	2.52	0.05	0.94
B1458478	Sanchez (2021)	Bunger Hills	100.6	-66.2	quartz sandstone	quartzite	2547	6	2565	7	1.11	5.03	0.14	5.21	0.1	1.03
B131132	Sanchez (2021)	Bunger Hills	100.6	-66.2	sub-lithic arenite	quartzite	2645	7	2647	7	0.22	5.11	0.11	5.44	0.09	0.98
B328329	Sanchez (2021)	Bunger Hills	100.5	-66.3	sandstone	quartzite	2644	7	2650	7	0.55	2.29	0.04	2.88	0.1	1.01
B330331	Sanchez (2021)	Bunger Hills	100.5	-66.3	quartz arenite	quartzite	2633	7	2639	7	0.57	3.53	0.06	5.22	0.1	1.09
B332333	Sanchez (2021)	Bunger Hills	100.5	-66.3	sandstone	quartzite	2659	7	2659	7	0.02	4	0.94	3.52	0.08	0.99
C1-814A2	Sanchez (2021)	Chick Island	121	-66.8	charnockite	granodiorite	2778	7	2740	7	-1.21*	2.33	0.05	2.36	0.04	0.99
G148149	Sanchez (2021)	Gillies Island	96.4	-66.5	diorite	monzodiorite	2858	7	2868	7	0.54	1.97	0.03	2.14	0.03	0.98
G151152	Sanchez (2021)	Gillies Island	96.4	-66.5	gabbro	monzogabbro	2885	7	2925	7	2.07	1.71	0.02	1.94	0.02	0.89
G157158	Sanchez (2021)	Gillies Island	96.4	-66.5	orthogneiss	diorite	2707	7	2720	7	0.79	2.13	0.07	2.26	0.05	0.94
G160161	Sanchez (2021)	Gillies Island	96.4	-66.5	granite	granite	2543	7	2564	7	1.35	2.25	0.03	2.47	0.04	1
H277278	Sanchez (2021)	Hippo Island	98.2	-66.4	diorite	monzodiorite	2839	7	2839	7	0.02	2.27	0.04	2.25	0.04	0.99
H291292	Sanchez (2021)	Hippo Island	98.2	-66.4	diorite	monzodiorite	2840	7	2842	7	0.11	2.37	0.04	2.26	0.02	1.01
R090091a	Sanchez (2021)	West Ice Shelf	84.1	-67.2	orthogneiss	granodiorite	2728	7	2732	7	0.21	2.64	0.23	2.44	0.18	0.85
T3NTK2	Sanchez (2021)	West Ice Shelf	85.8	-67.1	charnockite	monzonite	2585	7	2800	7	0.24	1.95	0.02	1.95	0.04	0.99
T7NTK2a	Sanchez (2021)	West Ice Shelf	85.8	-67.1	orthogneiss	monzonite	2646	7	2667	7	1.26	1.87	0.03	2.02	0.02	0.98
W142	Sanchez (2021)	Windmill Islands	110.5	-66.3	orthogneiss	granite	2610	7	2614	7	0.23	2.94	0.07	2.7	0.05	1.03
W172	Sanchez (2021)	Windmill Islands	110.5	-66.4	granite	granite	2607	7	2613	7	0.36	2.6	0.05	2.73	0.03	0.99
W180	Sanchez (2021)	Windmill Islands	110.6	-66.2	orthogneiss	granite	2669	7	2672	7	0.14	2.51	0.05	2.55	0.04	1
W185	Sanchez (2021)	Windmill Islands	110.6	-66.4	charnockite	gabbroic diorite	2889	7	2892	7	0.17	2.28	0.08	2.36	0.04	1
335-19	Blight (1975)	Windmill Islands	110.4	-66.2	charnockite	granodiorite	2741	7	2746	7	0.27	3.37	0.07	3.39	0.06	1.08
335-21	Blight (1975)	Windmill Islands	110.4	-66.2	leucogneiss	granite	2645	7	2646	7	0.05	2.67	0.06	2.8	0.05	1
335-30	Blight (1975)	Windmill Islands	110.4	-66.2	leucogneiss	granite	2660	7	2669	7	0.56	2.76	0.03	2.71	0.03	1.05
335-32	Blight (1975)	Windmill Islands	110.4	-66.2	migmatite gneiss	granite	2532	7	2609	7	5.14	2.63	0.05	2.83	0.05	0.99
335-35	Blight (1975)	Windmill Islands	110.4	-66.2	leucogneiss	granite	2641	7	2646	7	0.35	3.02	0.06	3.05	0.07	1.04
335-50	Blight (1975)	Windmill Islands	110.4	-66.2	layered gneiss	granodiorite	2676	7	2685	7	0.54	2.78	0.07	2.81	0.06	0.94
335-74	Blight (1975)	Windmill Islands	110.4	-66.2	migmatite gneiss	granite	2617	7	2628	7	0.7	2.61	0.06	2.75	0.08	1.1
335-83	Blight (1975)	Windmill Islands	110.4	-66.2	migmatite gneiss	diorite	2797	7	2826	7	1.64	2.78	0.06	2.95	0.04	0.91
335-100	Blight (1975)	Windmill Islands	110.4	-66.2	ribbon gneiss	granite	2647	7	2647	7	0.004	2.74	0.04	2.7	0.04	0.98
335-113	Blight (1975)	Windmill Islands	110.4	-66.2	ribbon gneiss	granite	2645	7	2655	7	0.61	2.74	0.05	2.83	0.04	1.03
335-160	Blight (1975)	Windmill Islands	110.4	-66.2	layered gneiss	granodiorite	2657	7	2790	7	8.01	3.13	0.05	3.08	0.06	1.01
335-321	Blight (1975)	Windmill Islands	110.4	-66.2	layered gneiss	granodiorite	2683	7	2685	7	0.13	3.01	0.06	3.03	0.08	1.06
335-375	Blight (1975)	Windmill Islands	110.4	-66.2	leucogneiss	granite	2624	7	2620	7	-0.1*	2.74	0.29	2.7	0.05	0.9
335-380	Blight (1975)	Windmill Islands	110.4	-66.2	layered gneiss	granite	2675	7	2675	7	0.01	2.58	0.06	2.59	0.05	1.03
335-400B	Blight (1975)	Windmill Islands	110.4	-66.2	aplite	granite	2621	7	2622	7	0.07	2.81	0.03	2.9	0.03	0.98
335-402	Blight (1975)	Windmill Islands	110.4	-66.2	migmatite gneiss	granodiorite	2788	7	2789	7	0.047	2.96	0.05	2.88	0.06	0.98
335-502	Blight (1975)	Windmill Islands	110.4	-66.2	pegmatite	granite	2456	7	2580	7	9.18	2.53	0.04	2.78	0.04	0.99

355-1	Blight(1975)	-66.2	110.4	Windmill Islands	leucogneiss	granite	2620	7	2625	7	0.32	2.97	0.06	2.75	0.05	1.04
355-44	Blight(1975)	-66.2	110.4	Windmill Islands	migmatite gneiss	granite	2630	7	2636	7	0.4	2.73	0.04	2.81	0.08	1.01
355-82	Blight(1975)	-66.2	110.4	Windmill Islands	granite gneiss	granite	2671	7	2678	7	0.4	3.1	0.07	2.67	0.05	0.85
355-122	Blight(1975)	-66.2	110.4	Windmill Islands	ribbon gneiss	granite	2620	7	2624	7	0.28	4.06	0.21	3.55	0.05	1.07
355-144	Blight(1975)	-66.2	110.4	Windmill Islands	granite gneiss	granite	2583	7	2590	6	0.41	2.31	0.06	2.52	0.05	0.93
335-313	Blight(1975)	-66.2	110.4	Windmill Islands	layered gneiss	granite	2626	7	2631	7	0.34	2.49	0.04	2.82	0.06	1.06
355-324	Blight(1975)	-66.2	110.4	Windmill Islands	gneiss	granite	2620	7	2608	7	-0.43*	2.44	0.06	2.57	0.04	1.02
355-495	Blight(1975)	-66.2	110.4	Windmill Islands	leucogneiss	granite	2609	7	2625	7	0.98	2.88	0.04	2.77	0.05	1.02
355-519	Blight(1975)	-66.2	110.4	Windmill Islands	migmatite gneiss	granodiorite	2790	7	2795	7	0.289	3.02	0.09	2.86	0.05	0.97

[a] Lithology reported in reference publication.

[b] Lithology computed from major element chemistry using a TAS scheme for igneous protoliths (Middlemost 1994) and the Sandclass scheme for sedimentary protoliths (Herron 1988).

[c] Porosity; negative porosity estimates likely resulted from a small loss of mass during saturation.

[d] Anisotropy factor, defined as the ratio of parallel conductivity to perpendicular conductivity

Compositions of the Antarctic samples are typical of the distribution of rocks within the existing S. Jennings (2019) database. Exception include three mafic igneous samples with high TiO_2 (> 3 wt.%) and five quartzites with SiO_2 >85 wt.%, none of which have equivalents in the larger database (Figure 4.1). The majority of our samples are felsic with SiO_2 in the range of 60–75 volume %. Most other oxides range from 1 to 20 wt.% of the samples composition and decrease with an increasing in SiO_2. The exceptions to this trend are K_2O and Na_2O which appear to trend up with increasing SiO_2, peaking at 7 wt.% around 75 wt.% SiO_2.

Modal mineralogy of the Antarctic samples indicate quartz and plagioclase are the most prominent minerals, making up around 50 to 75 volume% of most samples (Supplementary Material). Orthoclase makes up anywhere from 0 to 25 volume%, although some samples have percentages as high as 60 volume%. Biotite and pyroxene are found in most samples to be about 10 volume% or less, with the exception of a few outliers. Garnet and hornblende are only found in a few samples and rarely above 5 volume%. None of the Antarctic samples contain observable olivine. In the QAP ternary system, we find the majority of samples range from monzogranite to tonalite, with only one syenitic sample and three quartz diorites (Figure 4.2 A).
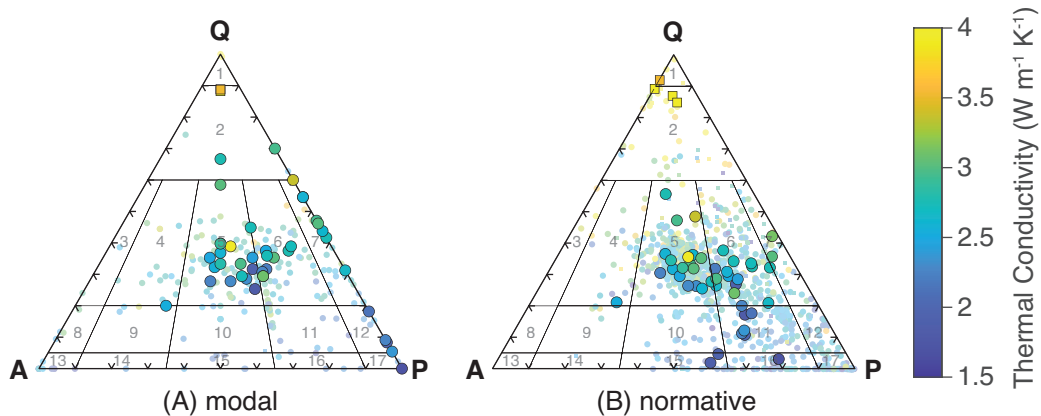
Figure 4.2: Sample compositions in the quartz–plagioclase–alkali feldspar (QAP) ternary system shown for (A) modal and (B) CIPW normative mineralogy. Igneous and meta-igneous samples are displayed as circles and meta-sedimentary samples as squares. Numbered fields: 1, quartzolite; 2, quartz-rich granitoid; 3, alkali granite; 4, syeno-granite; 5, monzogranite; 6, granodiorite; 7) tonalite; 8, alkali-feldspar quartz syenite; 9, quartz syenite; 10, quartz monzonite; 11, quartz monzodiorite/monzogabbro; 12, quartz diorite/quartz gabbro; 13, alkali feldspar syenite; 14, seyenite; 15, monzonite; 16, monzodiorite/monzogabbro; and 17, diorite/gabbro.

Not all of the samples in the geochemical database include modal mineralogy there-fore, we also compute the normative mineralogy using a CIPW norm (Verma et al. 2003). Normative quartz using this method is similar to modal quartz, but the feldspar composi-tions tend to be more alkali than observed (Figure 4.2 B), though plagioclase (albite and anorthite) are still more common.

4.3 Methods

4.3.1 Density

Density is determined for each samples using Archimedes' principle.

$$\rho_{\text{sample}} = \rho_{\text{water}} \frac{m_{\text{air}}}{m_{\text{air}} - m_{\text{water}}} \tag{4.1}$$

where ρ_{water} is the density of water at room temperature, and m is the mass of the sample. Sample masses were measured using a Satorius Entris 4201I-1S balance. The samples were weighed in both air on the top of the scale and in water by hanging the sample below the scale on a nylon string and completely submerged in a tank of water. Uncertainty was calculated using standard error propagation from the scale precision ($\pm$ 0.01 g) for mass uncertainties and the uncertainty in the water density, which was approximated by as $\pm$ 1.16 kg m^{-3} from known water density variations between 20 °C and 25 °C.

Samples were measured for density both dry and water saturated to estimate porosity. Samples were saturated in a vacuum for a minimum of 4 hours to fill externally-connected porosity. After removing samples from the vacuum, the samples were stored submerged in water to ensure pore spaces remain filled. As small grains or chips may fall off the sample during saturation, the porosity estimates should be considered a minimum estimate. The samples were dried and remeasured after saturation to minimize such issues.

4.3.2   Thermal Conductivity

Thermal conductivity measurements were performed using an optical thermal conductivity scanner (Lippmann and Rauen TCS) following the procedure outlined by S. Jennings (2019). To ensure uniform absorption of heat, all 49 samples were taped along a flat surface using black 3M Scotchcal Graphic Film 50™ and then placed above a set of optical scanners and a heat source.

Calibrated standards were measured at the start and end of each run. Two standards were used: a gabbro ($k = 2.37$ W m^{-1} K^{-1}) for the majority of analyses and a titanium alloy ($k = 5.94$ W m^{-1} K^{-1}) for samples with higher conductivity. Each sample was measured three times to reduce uncertainty, then rotated 90° and measured an additional three times to test for anisotropy. From these values, we determined the arithmetic mean thermal conductivity and the uncertainty of the samples (table 4.2).

Thermal conductivity was measured on the samples in both dry and water-saturated states. Dry conductivities were determined first. Saturated conductivity was collected using the same procedures as the dry samples. In some cases, saturation affected the tape adhesion creating an additional source of error for these measurements. We, therefore, consider saturated conductivities to be inaccurate.

4.3.3   Linear Analysis

We use linear-least squares regression to produce a multivariate model for conductivity with chemical composition and mineralogy. This approach differs from most studies that routinely forward model the conductivity from estimates of mineral conductivities (e.g., Chopra et al. 2018, Ye et al. 2022). Instead, the inverse approach is a novel way to estimate the conductivities of individual constituents. S. Jennings (2019) tested several common mixing relationships for thermal conductivity and determined the lowest misfit was obtained using geometric mixing. We use a geometric mixing relationship to approximate the observed conductivity (S. Jennings 2019),

$$\log k_{\mathrm{obs},j} \approx \sum_i v_{ij} \log k_i, \tag{4.2}$$

from the thermal conductivity of the individual constituents, k_i, with a mass or volume fraction v_{ij} for the j-th sample. The constituents are modeled independently using major element oxides, mineral modes and normative mineralogy, with associated mass, volume and mass fractions, respectively. To reduce the influence of samples with large uncertainties on the fit, we apply a weighting factor using a diagonal matrix, $\mathbf{W}$, with values $w_{ii} = \sigma_i^{-2}$, where σ_i is the standard deviation associated with $k_{\mathrm{obs},j}$. Samples without reported standard deviations were set at 0.058 W m^{-1} K^{-1} ($\sim$2.5%). We solve for the $\log k_i$ coefficients using a weighted linear least squares formulation,

$$\mathbf{m}_{LS} = (\mathbf{G}^{\mathrm{T}}\mathbf{W}\mathbf{G})^{-1}\mathbf{G}^{\mathrm{T}}\mathbf{W}\log\mathbf{k}_{\mathrm{obs}}, \tag{4.3}$$

where $\mathbf{G}$ represents a M $\times$ N matrix of mass/volume fractions normalized such that they sum up to 1. The 95% confidence interval is computed for the modeled constituent conductivities by

$$\Delta\mathbf{m}_{LS} = 1.96\,\mathrm{diag}\left((\mathbf{G}^{\mathrm{T}}\mathbf{W}\mathbf{G})^{-1}\right)^{1/2}. \tag{4.4}$$

We normalize all the major element oxide data to anhydrous conditions before modelling conductivity. For the mineralogy-based models, there are minor/accessory phases that are included in the mineral assemblage. Because very few samples contain all of the accessory minerals, the mass and volume fractions are normalized to exclude the minor phases from the regression.

4.4 Results

4.4.1 Measurements

Density measurements of Antarctic samples indicate low porosity, <2%, though three samples had porosity 5–10% due to fractures (335-32, 335-160, and 335-502, Table 4.2). Densities range from 2456 kg m^{-3} for the granitic sample 335-502 to 2885 kg m^{-3} for sample G151152 of monzogabbroic composition. Densities for each of the samples are consistent with the typically reported ranges (2500 to 3100 kg m^{-3}) for plutonic and

meta-igneous rocks (Hasterok & Webb 2017, S. Jennings 2019).

The majority of Antarctic samples have thermal conductivity values which lie between 2.4 to 3 W m^{-1} K^{-1}, with quartz-rich samples typically higher, 4 to 5 W m^{-1} K^{-1} (Table 4.2). Six samples have relatively low thermal conductivities <2 W m^{-1} K^{-1}, though these samples have neither high porosity nor significant anisotropy. Anisotropy factors computed by the ratio of perpendicular to parallel thermal conductivity are close to 1 for most samples. Only three samples have anisotropy factors <0.9: G151152, R090091a, and 355-82, indicating a 10% difference in the conductivity between the maximum and minimum directions. Our samples were cut with one flat face nearly perpendicular to the foliation planes—if present (17 samples), so we did not measure the conductivity along the third spatial axis. Therefore, the anisotropy factors may not identify the largest anisotropy for foliated samples, though the conductivity along the third axis is unlikely to differ significantly from our observations due to the low porosities and planar foliation of these samples.

There is a slight increase in thermal conductivity for most samples when water saturated, though the dry and saturated measurements are poorly correlated (Table 4.2). Saturated conductivities should be higher than dry measurements, yet 16 of our samples have lower saturated conductivities. There are several potential causes for the poor correlations and lower saturated conductivities. First, many of the conductivities are within the uncertainty of our measurements, likely due to our very low sample porosities ($<2\%$). Second, there is uncertainty from slight differences in scan lines between the dry and saturated measurements of a sample. Third, partial surface drying of saturated samples occurs during the short duration of sample preparation and measurement, which can affect the quality of saturated measurements depending upon the geometry and connectivity of pores. Fourth, the wet surfaces caused poor adhesion of the tape on some samples, reducing the quality of the saturated measurement. Since our samples are generally low porosity and have a $<10\%$ difference—within measurement uncertainty—between the dry and saturated states, we focus our remaining analysis on the dry measurements only.

4.4.2   Compositional control

The thermal conductivity measurements of the Antarctic samples are within the bounds of previous studies for similar composition samples (Figure 4.1). The clearest pattern of thermal conductivity with composition is an increase with increasing SiO_2. An increase in most other oxides tends to correlate with a reduction in the thermal conductivity. One notable exception is MgO, which exhibits a minimum conductivity at $\sim$10 wt.%. Higher conductivities for samples with >10 wt.% MgO result from ultramafic compositions with high percentages of olivine (whose conductivity is >3 W m^{-1} K^{-1} in ambient conditions) (e.g. Horai 1971). Na_2O and K_2O show no clear pattern with thermal conductivity (Figure 4.1). There is a relatively large variance in conductivity for any specific element concentration, including SiO_2.

Mineralogy is highly variable between samples. Many minerals that may have significant modal fractions (>5%) are found in few samples; e.g., olivine in 6%, garnet in 5% and hornblende in 40% of all samples, respectively. These same minerals are generally absent in most samples. The most common constituents are quartz, alkali-feldspar and plagioclase feldspar, each occurring in >78% of samples. Samples with the highest proportion of quartz have the highest thermal conductivities (Figure 4.2). In contrast, samples with low quartz and high plagioclase have the lowest thermal conductivity for both modal and normative mineralogy. There is significant variability and a few samples that clearly appear as anomalies, most notably the ribbon gneiss sample 355-122 (Blight & Oliver 1977) with a conductivity of 4.06 W m^{-1} K^{-1}, $\sim$1 W m^{-1} K^{-1} higher than similar composition samples. Conductivity generally increases as the proportion of olivine increases; however, few samples, and none of ours from Antarctica, contain olivine. Because of the high variability in mineral proportions and relatively similar conductivities for most common rock-forming minerals it is difficult to separate the contributions of individual minerals clearly with simple biplots. Thus, multidimensional regression is required to tease apart the individual contributions accurately.

4.4.3   Inverse modelling

To develop empirical models for thermal conductivity as a function of composition, we combine our 49 Antarctic samples with data from a number of previous studies (Table 4.1). There are 1,073 samples with thermal conductivity estimates and major element data. Normative modes are also calculated for these samples, making the results for these analyses directly comparable. There are many fewer samples with modal mineralogy ($N = 295$). A simple root-mean-square misfit is relatively similar for all three models: 0.39 W m^{-1} K^{-1} for oxides, 0.37 W m^{-1} K^{-1} for modal mineralogy, and 0.39 W m^{-1} K^{-1} for normative mineralogy. Another metric, the reduced χ^2_ν misfit that is minimized to estimate the coefficients, is considerably higher for the modal mineralogy model due to the significantly fewer data: 6.5 for oxides, 8.7 for modal mineralogy and 6.8 for normative mineralogy.

The results of a linear regression between thermal conductivity and major element oxides results in similar oxide coefficients as found by S. Jennings (2019) despite twice as many samples in this study (Figure 4.3A). The only notable difference is are the oxide coefficients SiO$_2$ and FeO, which are >1 W m^{-1} K^{-1}. Uncertainties for the individual coefficients are generally low (95% confidence bounds <1 W m^{-1} K^{-1}), with the exception of the coefficient for total FeO (Figure 4.3 A). The confidence bounds for the total FeO bound is 8 W m^{-1} K^{-1}. Perhaps the multiple oxidation states of iron, which can partitioning into different sites within minerals is partially responsible. Only 193 samples are reported with both FeO and Fe$_2$O$_3$, limiting our ability to produce a precise model. Even so, a simple test on the this subset suggests that partitioning iron will reduce the uncertainty on the iron coefficients, but it does not change the empirical estimate of conductivity or the model accuracy significantly. Therefore, we use the total iron model as it allows for a significantly larger data set for calibration.

The performance of the model is generally within the bounds of the uncertainty of conductivity variability but indicates a possible systematic bias in the residuals (Figure 4.4). The typical variability in thermal conductivity is $\pm$ 10 to 20% for a typical conductivity measurement. Most of the data, 59%, lie within 10% of the measured conductivity and

90% lie within 20% of the observed value. We consider this to be a reasonable result. However, there appears to be a skew in the residuals with low conductivity values more commonly overpredicted and high conductivity values more frequently underpredicted. A similar skew is also found for the modal and normative mineralogy models.

The skew is persistent despite a number of additional tests. None of the standard mixing models, arithmetic, harmonic nor square-root means, improve the result or reduce the skew of the residuals. We formulated models with higher order SiO_2 terms, but there was little effect. Only 339 data include loss-on-ignition (LOI) analyses that can be used to interrogate the effect of water or filter the data. An oxide model produced with LOI has no significant effect on reducing the skew in the residuals. This result suggests that simple linear regression using standard mixing models are not adequately capturing the physical mixing correctly.

Inverting for mineral thermal conductivities performs well despite limited number of data and observational challenges (Figure 4.3B). Residuals for the modal mineralogy model are similar to those for the oxide model (Figure 4.4C). Modal mineral estimates can vary significantly in precision and accuracy (Harvey et al. 1998). Field estimates of hand-sample mineralogy are often low precision with uncertainties of 10 to 20% or greater, even for experienced individuals. Such estimates often ignore trace minerals, i.e., visually $<2\%$, or may simply record occurrence. Estimates derived from analysis of thin sections and instrumental analysis can be more precise, but may be subject to nugget effects that may not be representative of the hand sample. While common trace minerals are often reported their contributions to conductivity are ignored, which may lead to errors or biases in estimated mineral conductivities. Regardless of these challenges, the estimated mineral conductivity values closely match both S. Jennings (2019) and laboratory estimates for several common minerals with the exceptions of pyroxene, garnet and, most notably, quartz. While quartz is very common, the underprediction by 2 W m^{-1} K^{-1} was also noted by S. Jennings (2019) in both modal and normative observations (Figure 4.3). The thermal conductivity of garnet differs between it's different varieties, ranging from 2 to >7 W m^{-1} K^{-1} (Supplementary Table 2). Because there are relatively few samples with

garnet (15), additional data may be required to improve the garnet coefficient.

The normative mineralogy model produces similar results as the modal mineralogy model (Figure 4.3C). Normative mineralogy has the potential to account partitioning of elements between various components in a way that more closely mimics nature compared to major element oxides. S. Jennings (2019) found that the normative model performed better than the oxide model, as minerals with the same elements can have different conductivites. However, the improvement was minor and below our ability to resolve the difference. In this study, the normative model provides a similar RMS misfit. A greater mismatch between modal and normative mineralogy could limit the accuracy of the normative mineralogy model. Our updated dataset incorporates a number of samples of higher metamorphic grade with abundant amphibole, and garnet that are less common in lower grade rocks and cannot be modeled by a CIPW norm. The residuals for the normative model are similar to both the oxide and modal mineralogy models (Figure 4.4C).

4.5   Discussion

4.5.1   Conductivity of Antarctic surface samples

One of the greatest impediments to developing accurate models of GHF for Antarctica from geophysical proxies are laterally and vertically realistic thermal property models for the lithosphere. Since the observed thermal conductivity of Antarctic rock samples follows global patterns and the empirical modelling produces reasonable predictions, we can predict thermal conductivities for Antarctica. Using the oxide model (Figure 4.3A), we estimate the thermal conductivity values for 6,995 Antarctic igneous and meta-igneous samples from the PetroChron Antarctica database (Sanchez et al. 2021). Antarctic samples are largely constrained to coastal regions where outcrops are exposed. These samples generally range from 42 to 78 wt.% SiO_2, with bimodal peaks associated with mafic and felsic compositions (Figure 4.5). Estimated conductivities range from 1.6 to >4W m^{-1} K^{-1}, though most lie between 1.8 and 3 W m^{-1} K^{-1} (Figure 4.5). The distribution is near

unimodal, though there is a slight indication of a lower conductivity bump associated with the mafic SiO_2 peak. The estimated conductivity distribution is reasonable for most of the observed SiO_2 distribution, but likely lacks the appropriate variability and extreme values for the most mafic and felsic compositions due to the skew in the model residuals. Our samples with similar SiO_2 concentration range to the Antarctic geochemical database can have a thermal conductivity as high as 3.5 W m^{-1} K^{-1} or as low as 2.5 W m^{-1} K^{-1} due to other oxides. The average conductivity of the estimated samples is 2.49 ± 0.31 W m^{-1} K^{-1}.

Surface conductivities of Antarctica may be also be skewed by the sampled outcrops. Compositions within the global conductivity dataset are highly skewed towards felsic compositions. Antarctica in contrast, has a greater number of mafic samples relative to felsic ones, resulting in a lower number of high conductivities (Figure 4.5). Basalts and similar mafic lithologies yield primary information about lithospheric-scale processes. As a result, geochemists are notorious for volumetrically oversampling mafic relative to felsic lithologies despite an average granodioritic composition for the upper crust (Rudnick & Gao 2014).

4.5.2 Conductivity of the Antarctic lithosphere

To map the interior of the continent and extend thermal conductivity estimates laterally and vertically, we employ the use of indirect techniques. Density and seismic velocity are viable candidates for extending thermal conductivity to depth as there are existing geophysical models for these parameters across Antarctica (S. Jennings 2019). Comparing the observed conductivities with observed densities, we find a poor relationship between the two (Figure 4.6A), though there is a slight decrease in thermal conductivity as density increases. This is apparent in the moving average, but not the scatter in the data due to the high variability of thermal conductivity for any given density. Additional mafic and ultramafic samples may be helpful for improving a possible density–conductivity relationship.

While we have not measured seismic velocity directly, we can predict the seismic veloc-

ity of the samples using an approach proposed by (Behn & Kelemen 2003). Their model uses major element oxides to predict P-wave velocities and, though they did not provide a model for S-wave velocities, they compute the bulk modulus and density necessary to do so. Applying these velocity predictors, we can see a weak relationship between average thermal conductivity and both seismic velocities (Figure 4.6B and C). We model these velocity–conductivity distributions using third order polynomials:

$$k = -0.505\,V_P^3 + 11.23\,V_P^2 - 82.78\,V_P + 204.5, \tag{4.5}$$

$$k = -6.04\,V_S^3 + 77.44\,V_S^2 - 329.19\,V_S + 467.0, \tag{4.6}$$

where V_P and V_S are the P- and S-wave velocities, respectively. There is a minimum around 6.7 km s^{-1} and 4.2 km s^{-1}, for P-wave and S-wave velocities, respectively (Figure 4.6), which corresponds to intermediate to mafic lithologies (Behn & Kelemen 2003). The empirical relationship increases to low velocities consistent with felsic lithologies and reaches a local maximum at velocities consistent with the mantle for both P- and S-wave models. The empirical relationships reasonably approximate a moving average of the conductivity, giving us a mechanism to estimate thermal conductivity within the crust.

Applying the S-wave velocity–conductivity relationship to a tomography model, we estimate the thermal conductivity throughout the Antarctic crust. We use the S-wave model by Shen et al. (2018), which is derived from Raleigh waves and P-wave receiver functions using ambient noise tomography. Despite missing large regions of East Antarctica, this model was chosen because surface waves models tend to yield more accurate estimates of crustal velocities. Across the entire continent, the thermal conductivity is found to be rather uniform (k = ∼2.8 to 3.1 W m^{-1} K^{-1}) at shallow depths (3–11 km Figure 4.7). Conductivity generally decreases with depth, reducing to values of ∼2.1 to 2.5 W m^{-1} K^{-1} at depths >31 km. In the uppermost crust, the period of Raleigh waves combined with the seismometer spacing limits the horizontal resolution to >50 km, generally. As a result, it is suitable for regional variations, but it is not possible to resolve sharp discontinuities that can produce significant thermal anomalies related to refractive

effects (Willcocks et al. 2021). Some of these variations must exist, as short wavelength anomalies are clearly observable in airborne magnetic anomaly maps (e.g. Golynsky et al. 2018).

At 15 km depth, a distinct region of elevated thermal conductivity is observed across the interior that decreases in area with depth to a focus around the South Pole at ∼23 km depth. These high conductivities may be associated with thick felsic crust or a thick intracratonic basin associated with the lower velocities in the region (Shen et al. 2018). Below 27 km, thermal conductivity once again shows less heterogeneity across the continental crust. The moderately high thermal conductivity ($\sim$2.9 W m^{-1} K^{-1}) that grows in area with depth results from a shallow mantle beneath the West Antarctic Rift.

4.5.3 Improving GHF estimates

Our thermal conductivity model for the Antarctic crust can be used to improve current proxy-based models of GHF. When converting geothermal gradients into heat flux, current models have used uniform values for thermal conductivity across the entire continent (Maule 2005, Martos et al. 2017), or in the case of An et al. (2015), applied a 3-layered thermal conductivity model with no lateral variations. This lack of lateral variation likely results in erroneous GHF. Deviations of 30% or more are possible as our model suggests lateral thermal conductivity variations could be greater than 1 W m^{-1} K^{-1}(Figure 4.7). Our model is based on thermal conductivity under ambient laboratory conditions whereas higher temperatures within the crust tend to rapidly reduce thermal conductivity values by as much as ∼30% (Ray et al. 2021). Thus an adjustment for temperature and pressure effects is necessary when modelling GHF. Pressure tends to cause an increase in thermal conductivity (Horai & Susaki 1989), though the temperature effect is considerably larger.

There are a number of improvements that can be made to the thermal conductivity database that will improve the accuracy of empirical models produced in this study. In addition to pressure–temperature measurements, an emphasis on adding mafic and ultramafic samples could reduce uncertainties in the empirical models. A more in-depth exploration of the skew in conductivity residuals could produce a more accurate set of

compositional-based coefficients. More analyses on Antarctic samples is also desirable since most samples from this study are from a small region in East Antarctica. Lastly, a wider range of meta-sedimentary samples should be considered to improve the application of compositional-based models to a broader range of geological settings.

4.6   Conclusion

We find the thermal conductivities of Antarctic rocks are consistent with similar compositions from other sites globally. Conductivity can be estimated from composition within $\pm 20\%$ of measured values for 95% of samples using a geometric mixing model. The residuals display a skew, overpredicting low conductivities and underpredicting high conductivities, that cannot be removed by using standard mixing models. A linear regression results in the following model for thermal conductivity (k) as a function of oxide concentration (C_{oxide}) in weight fraction,

$$k = \exp\left(1.554\,C_{\mathrm{SiO_2}} - 6.521\,C_{\mathrm{TiO_2}} - 0.255\,C_{\mathrm{Al_2O_3}} + 2.066\,C_{\mathrm{FeO^T}} + 0.547\,C_{\mathrm{MgO}}\right.$$
$$\left. + 0.226\,C_{\mathrm{CaO}} - 2.402\,C_{\mathrm{Na_2O}} - 0.672\,C_{\mathrm{K_2O}}\right)$$

We apply this relationship to nearly 7,000 geochemical analyses in the PetroChron Antarctica database to estimate thermal conductivities for igneous protoliths, resulting in an average conductivity of 2.45 W m^{-1} K^{-1}. Seismic velocities can also be used to predict thermal conductivity vertically throughout the crust. While the method is limited by the resolution of the velocity model, we find a general decrease in thermal conductivity from $\sim$3 W m^{-1} K^{-1} in the shallow crust (3–11 km) to $\sim$2.2 W m^{-1} K^{-1} at depths >31 km. We also predict an anomalously high thermal conductivity centered beneath the South Pole that extends laterally from the Ronne Basin to the McMurdo Peninsula and vertically from 15 to 23 km depth. The lateral variability in thermal conductivity suggests additional variability in geothermal heat flux that is not accounted for by current geophysical proxy-based models. Improvements can be made to the compositional and property-based conductivity models by including temperature and pressure effects on conductivity and

adding additional mafic and ultramafic samples that are poorly represented in the global dataset.
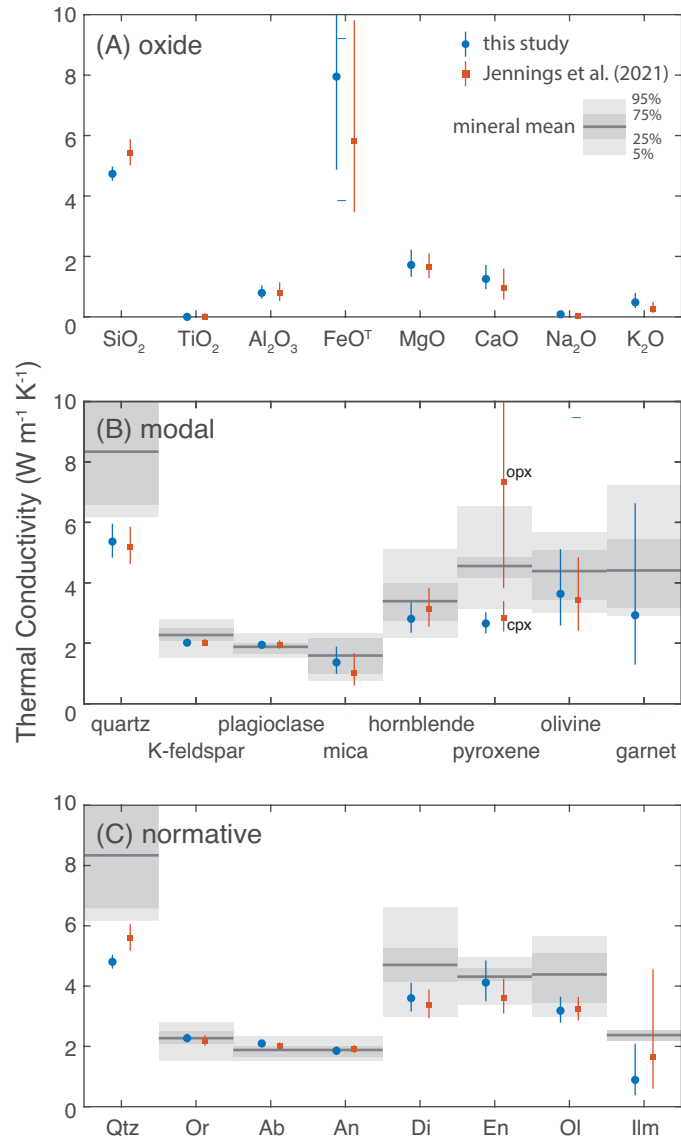
Figure 4.3: Linear regression between observed thermal conductivity and (A) major element oxide concentrations, (B) modal mineralogy and (C) estimated CIPW normative mineralogy using a geometric mixing model. Results from this study in blue circles and samples from S. Jennings (2019) in orange squares. Mineral estimates (Supplementary Table B) are shown in (B) and (C) for comparison with inverted conductivities. Coefficients for all three models are determined in log-space, i.e., $c_i = \log k_i$, and have been converted to linear-space for direct comparison with conductivities.
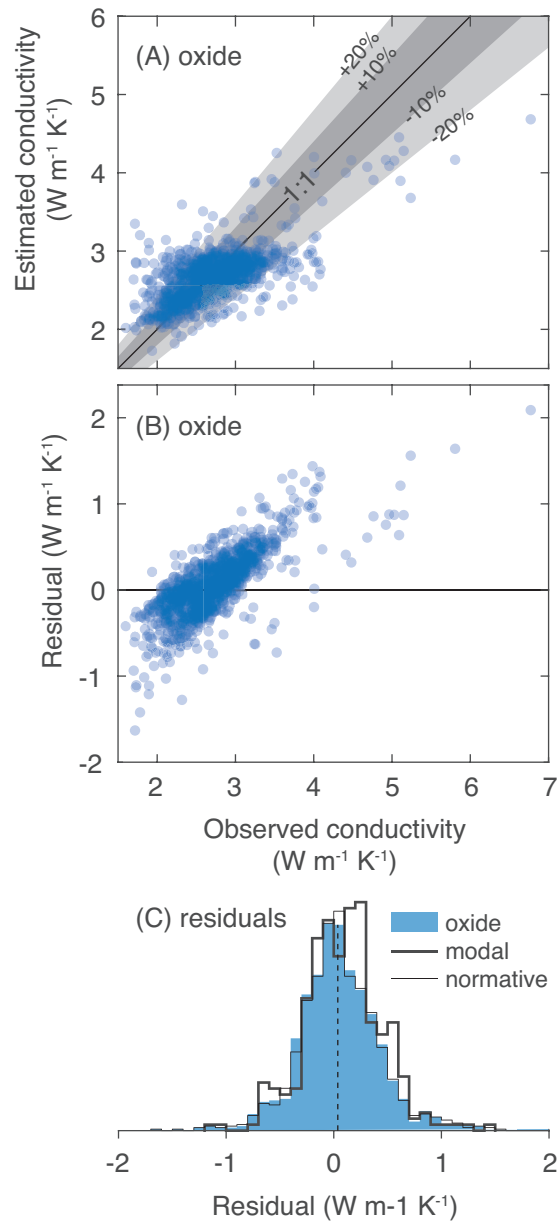
Figure 4.4: Thermal conductivity residuals associated with the linear regression models. (A) Observed and estimated thermal conductivity for the oxide model (Figure 4.3A). (B) Conductivity residuals (observed - predicted) for the oxide model. A skew in the residuals is apparent. (C) Histograms of residuals for all three regression models (Figure 4.3). The median residual for the oxide model is identified by the dashed line. Note that the residual skew is not obvious in (A) nor apparent in (C).
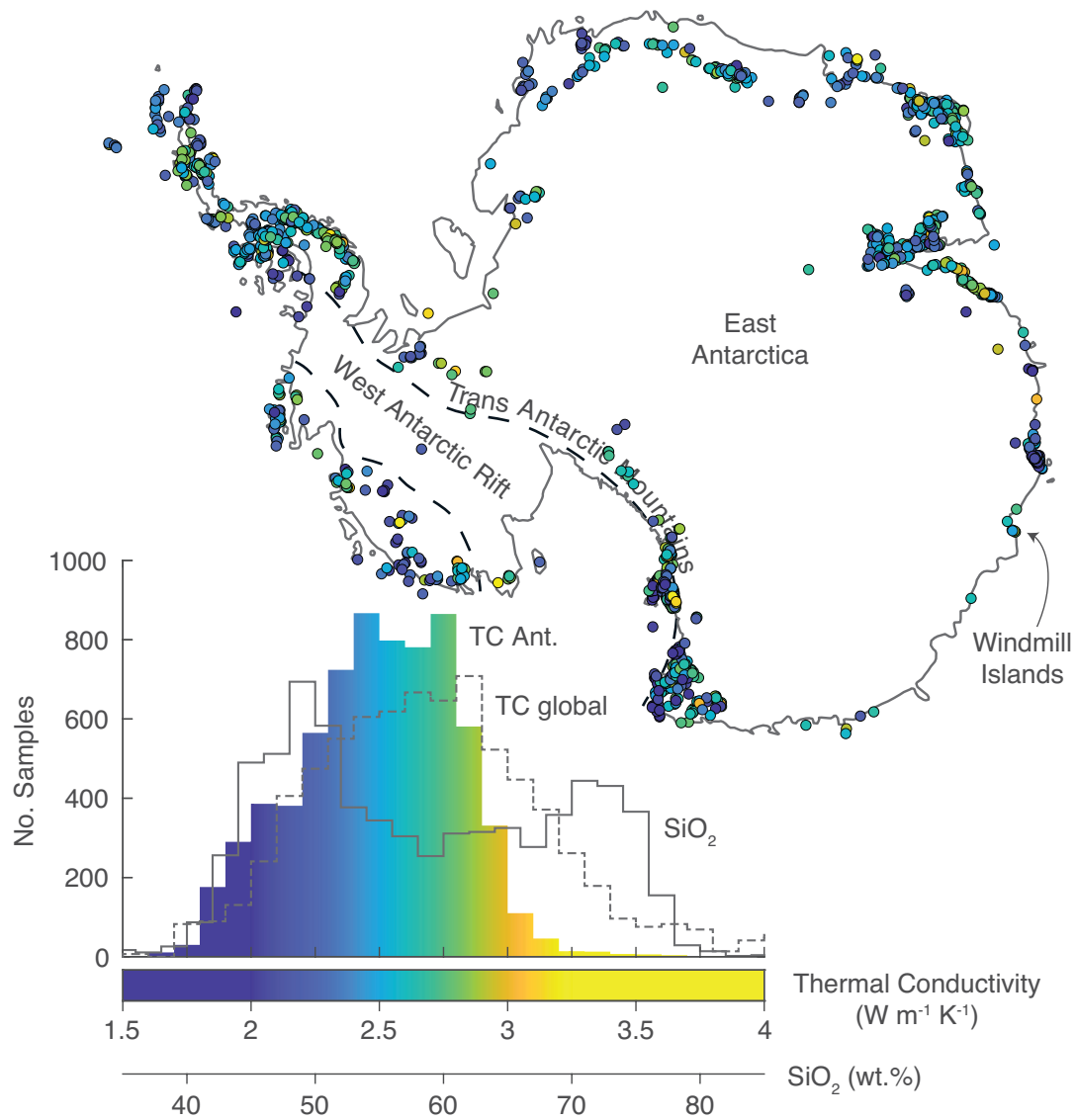
Figure 4.5: Thermal conductivity estimated using the oxide model for igneous protolith compositions from PetroChron Antarctica (Sanchez et al. 2021). Note the distribution of observed conductivity from the global database, shown for reference, has been rescaled.
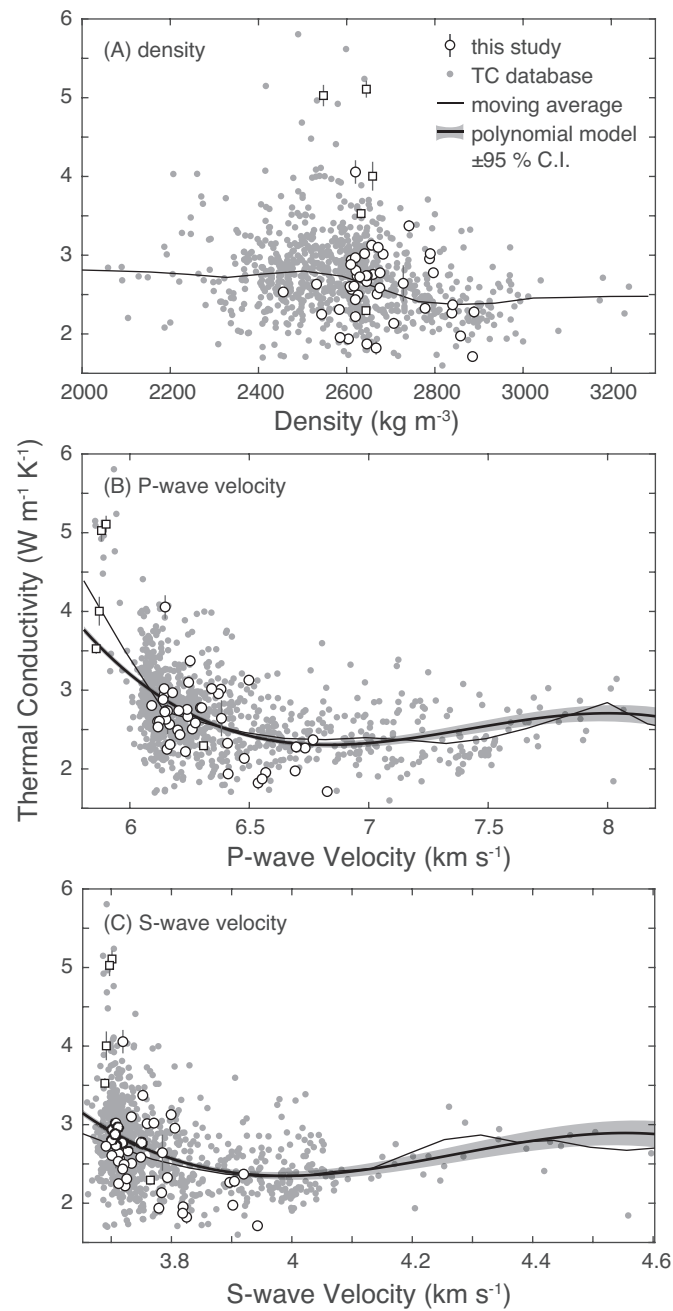
Figure 4.6: Relationship between thermal conductivity and geophysical parameters of A) Density, B) P-wave velocity and C) S-wave velocity. A quadratic model is estimate thermal conductivity from each physical parameter. A moving average shows reasonable agreement with the quadratic model for typical crustal values.
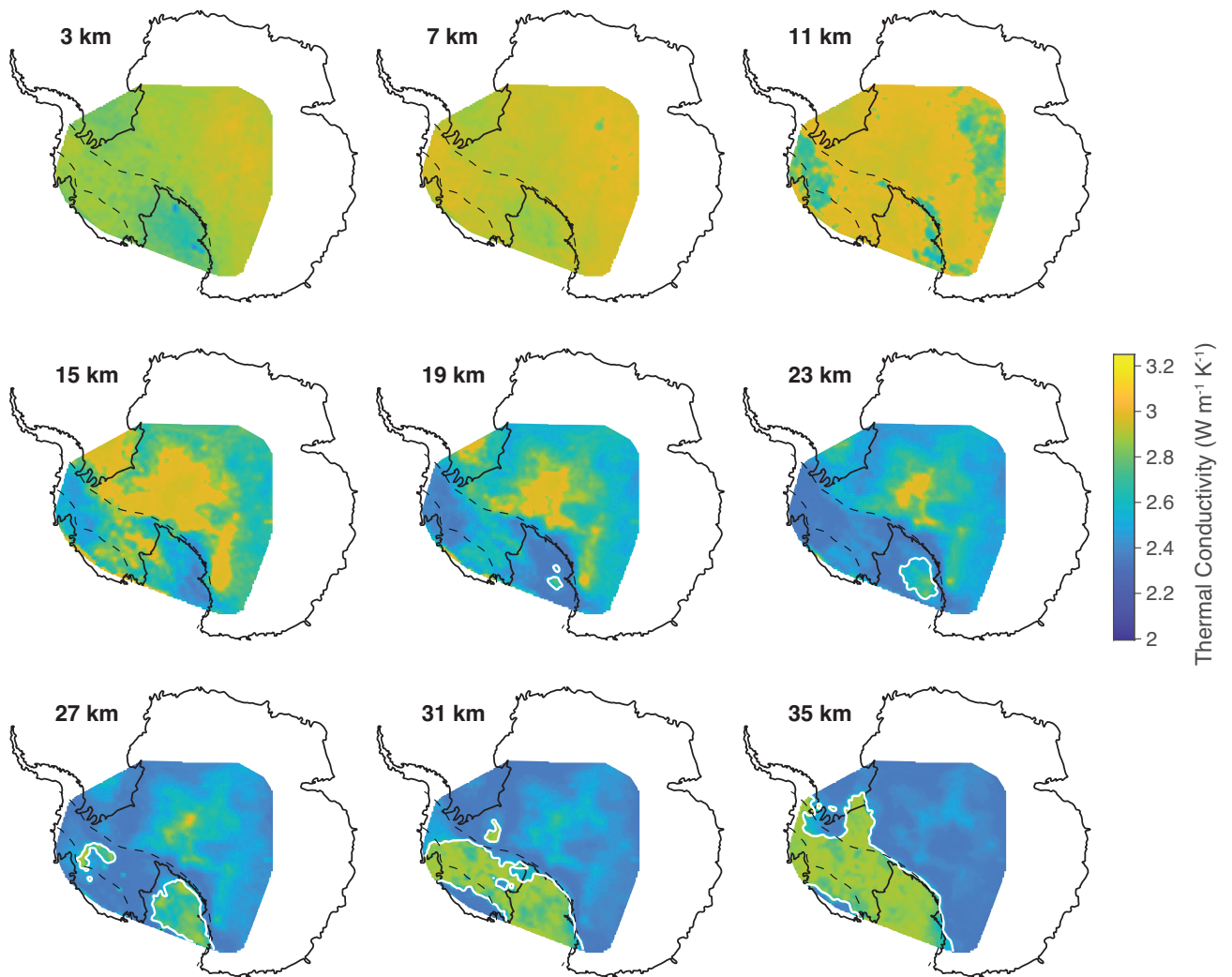
Figure 4.7: Thermal conductivity of the Antarctic crust with depth calculated from a seismic tomography model using Equation 4.6. The white contour encloses regions of below the Moho (Shen et al. 2018).

Statement of Authorship

Title of Paper	Melt constraints on the Geothermal Heat Flux beneath the Antarctic Ice Sheet
Publication Status	☐ Published ☐ Accepted for Publication ☐ Submitted for Publication ● Unpublished and Unsubmitted work written in manuscript style
Publication Details	

Principal Author

Name of Principal Author (Candidate)	Simon Robert Willcocks
Contribution to the Paper	Conceived the idea, developed the basal heat flux constraint, wrote the main paper and generate figures
Overall percentage (%)	90%
Certification:	This paper reports on original research I conducted during the period of my Higher Degree by Research candidature and is not subject to any obligations or contractual agreements with a third party that would constrain its inclusion in this thesis. I am the primary author of this paper.
Signature	Date 17/12/2022

Co-Author Contributions

By signing the Statement of Authorship, each author certifies that:

    i.   the candidate's stated contribution to the publication is accurate (as detailed above);

    ii.   permission is granted for the candidate in include the publication in the thesis; and

    iii.   the sum of all co-author contributions is equal to 100% less the candidate's stated contribution.

Name of Co-Author	Derrick Hasterok
Contribution to the Paper	Supervised the project, proofread and adjusted the final text and figures
Signature	Date 20 Nov 2022

Name of Co-Author	
Contribution to the Paper	
Signature	Date

Please cut and paste additional co-author panels here as required.

Chapter 5

Melt constraints on the Geothermal Heat Flux beneath the Antarctic Ice Sheet

Abstract

Geothermal heat flux (GHF) at the base of ice sheets is an important and poorly constrained boundary condition for glacial dynamics. Geophysical proxy-based methods provide estimates of GHF but yield significant differences between techniques. To evaluate proxy-based GHF estimates, we model the basal heat flux constraint (BHFC)—GHF that will begin to produce melt at the base of the ice sheet. We find most GHF proxy estimates fall below the BHFC across much of Antarctica. While most proxy-estimates satisfy the constraint, GHF must exceed BHFC regions near subglacial lakes to generate melting. Our results indicate current proxy-based GHF underestimates the true GHF at these sites ($\sim$80% of lakes), particularly in East Antarctica. This observation is consistent with studies of GHF in terranes conjugate to Antarctica that are poorly matched by proxy-based GHF estimates. We suggest proxy-based GHF can be improved by allowing for regional variability in crustal thermal properties or by collecting additional GHF observations at key sites to calibrate GHF proxies. We recommend ice sheet models incorporate

higher variability, and greater magnitudes of GHF estimates beneath the East Antarctica ice sheet near lakes.

5.1   Introduction

Temperature is an important control on the dynamics of continental ice sheets due to its effect on the strain rate (Goldsby & Kohlstedt 2001), hardness (Larour, Seroussi, Morlighem & Rignot 2012) and melting of ice (Greve & Blatter 2009). Improving models of these properties are critical to accurately model the dynamics of the Antarctic continental ice sheet as mass loss accelerates due to recent climate change (Rignot 2019). However, temperatures within the ice are uncertain. An important constraint on temperatures within ice sheets is the geothermal heat flux at the ice/rock boundary (Paterson 1994, Llubes et al. 2006). Due to the remoteness of Antarctica and the expense of drilling through a thick ice sheet, direct measurements of the Antarctic Geothermal Heat Flux (GHF) are rare and difficult to collect (Kadir et al. 2013). Only 24 sparsely spaced GHF determinations have been made via temperature profiles through the ice sheet (Guimarães et al. 2020). Furthermore, these models are limited in their accuracy due to convection in the ice (Hughes 2012) and lack of temperature measurements in the underlying bedrock (Mony et al. 2020). Therefore, to produce temperature models with sufficient resolution for ice sheet dynamics, proxies for GHF are often used.

Several indirect (proxy) methods have been developed over the past ca. 20 years to estimate Antarctic GHF. These temperature-sensitive proxy-based methods include, satellite and airborne derived models of Curie depth (Maule 2005, Martos et al. 2017), seismic topography (Shapiro 2004, An et al. 2015), statistical comparisons with similar geological environments external to Antarctica where heat flux is known (Lucazeau 2019, Shen et al. 2020, Stål et al. 2021) and interpolation from measured heat flux locations (Guimarães et al. 2020). While all of these models suggest that East Antarctica has low GHF and West Antarctica has high GHF, there are significant differences in the magnitudes and spatial variations. These differing results often indicate uncertainties in GHF at the base of the Antarctic ice sheet greater than those reported by individual

studies. In reality, there are good reasons to suspect that there are significant anomalies due to observations in conjugate terranes (Pollett et al. 2019), but the correlation with Antarctic models is generally poor.

To improve the accuracy of Antarctic GHF models, we estimate the GHF required to induce melting at the base of the ice sheet in Antarctica. The model is constructed from a one-dimensional solution of the heat flow equation, incorporating advection and basal shear. The modelled result provides an upper bound for GHF in regions where the bed is frozen and a lower bound in the presence of lakes. Using this basal heat flux constraint (BHFC), we evaluate six current proxy-based GHF models for Antarctica. Our results indicate that the GHF proxies generally satisfy the bounds placed on the BGHC model and lake presence, but may underestimate GHF in some regions of East Antarctica.

5.2 Background

5.2.1 Proxy Studies

Geophysical proxies provide valuable estimates of GHF below ice sheets due to the lack of direct measurements, but to create them, assumptions are made that may influence the accuracy. Since Shapiro (2004) first estimated GHF using seismic velocity as a proxy, several studies have indirectly estimated the Antarctic GHF using a variety of methods. As proxy estimates are indirect, any resulting estimate is explicitly biased by the data and/or regions used to develop empirical correlation between the proxy and the property of interest. Biases from unique geological environments and/or additional physical processes, not accounted for in the correlation, can affect the accuracy of a proxy-based estimate. Incorporating these biases into the proxy estimate is often unavoidable due to a lack of a prior knowledge. Below, we detail six GHF models and discuss the potential for each methodology to yield inaccurate results.

The GHF model by Maule (2005) and Martos et al. (2017) estimate heat flux through the magnetic Curie depth estimates. Curie depth provides a constraint on the depth to the Curie isotherm, which typically lies within the crust. The Curie depth is estimated

by examining the spatial variations in spectral content of the lithospheric magnetic field. Maule (2005) estimates the Curie depth from satellite magnetic field observations using the equivalent source dipole method. Martos et al. (2017) estimates Curie depth from airborne magnetics using the defractal spectral technique. The defractal spectral method results in higher resolution, but requires filling the aeromagnetic record gaps using satellite observations. Each magnetic-based proxy models has advantages and drawbacks (Chapter 6, Gard 2021). Most notably, Curie depth estimates are heavily biased by the initial guess, as it is the perturbations about this depth that are more accurately estimated. In both cases, the crustal thickness is supplied as the initial guess, but to produce shallow Curie depths beneath West Antarctica the crustal thickness is arbitrarily halved (Gard & Hasterok 2021). Once Curie depth is determined, heat flux is estimated by computing a geotherm that passes through the surface temperature and Curie temperature (assumed value) at the Curie depth. Producing the geotherm requires additional estimates of the thermal conductivity and heat production in the crust. Both studies assume a uniform model of thermal properties (heat production and thermal conductivity) for the crust across Antarctica. Thus, we can expect additional uncertainty in heat flux resulting from variations in crustal composition. Gard (2021) has estimated the uncertainties resulting from composition to be on the order of 10-20%.

The GHF model from An et al. (2015) uses mantle shear wave tomography, which converts velocities into temperatures using a method similar to Goes et al. (2000). Crustal velocities cannot be used because the effects of temperature are masked by variations in crustal composition. Mantle temperature estimates are extrapolated through the crust, assuming a known subglacial temperature. These 1D, steady-state models are produced by splitting the crust into three layers with generalized thermal conductivity and heat production values based on global averages. These three layers do not include the overlying ice sheet or take into account advection of heat within the ice, or additional heat generated via basal shear/sliding. The seismic-based proxy model by An et al. (2015), much like magnetic-based models, is highly dependent on the crustal properties that were assumed to be laterally uniform throughout the model. Gard & Hasterok (2021) shows the seismic-

based and Curie depth models are strongly dependent on the chosen crustal parameters with Curie depth estimates differing by up to 20 km between models, thus drastically effecting the final results for estimated GHF.

The GHF model Guimarães et al. (2020) estimates the heat flux from near-surface observations. These observations include 78 drill-core wells, 41 sites of recent volcanic activity, 372 subglacial lakes, and 306 sites based on basal temperatures of glaciers. Combining these 793 sites, this model fills in the remaining gaps by interpolating heat flux between the known locales. Heat flux around volcanic regions is estimated by observing the relation between volcanic magma chamber volume and the time elapsed since its formation Smith et al. (1978). Heat flux estimates around subglacial lakes are made using a similar method to Siegert & Dowdeswell (1996) (which will be used later in this study), this method assumes that by subglacial lakes being at the point of phase change in the ice one can accurately assume the basal heat flux must be at the exact rate to melt the ice. To account for regions not close to any of the 793 sites, the model relies on other basal heat flux models to create a continuous map. Since Guimarães et al. (2020) model is highly dependent on site observations, it is susceptible to the uncertainties and bias found in those observations. The use of volcanic sites is potentially questionable as volcanic environments often have much greater GHF estimates than the regional average. For example, their final GHF model includes several sizable regions in West Antarctica that have unreasonably high heat flux, >150 mW m^{-2}. A heat flux of such a magnitude would likely result in regionally extensive melting of the middle and lower crust (Chapman 1986, Hasterok & Chapman 2011). Guimarães et al. (2020) also use the presence of lakes to estimate GHF based on an analytical calculation derived from de Q. Robin (1955), which makes several approximations and assumes constant physical properties throughout the ice sheet that reduce the accuracy of GHF estimates. This uncertainty is most significant where the ice sheet is thin as the properties of ice change considerably in the upper 300 m as porosity of ice is rapidly decreased. Guimarães et al. (2020) method is also valid for passive lake environments where the increase in temperature along a passive thermal gradient reaches the melting point at the base of the ice sheet. However, there are also

active lakes that form as melt water produced elsewhere infills of lower topographic areas
Brocq et al. (2013) regardless of the temperature at the base of the ice sheet.

The GHF model by Shen et al. (2020) estimates heat flux across Antarctica by identi-
fying regions of the continental United States with similar seismic characteristics (velocity
and gradient) at ∼80 km depth. Antarctic GHF is then estimated from the estimated
heat flow of statistically similar regions of the continental United States. Stål et al. (2021)
expands upon the work of Shen et al. (2020) by combining multiple data sets of Antarc-
tic crustal properties and comparing them with Australia's crustal properties to identify
Antarctic heat flux based on Australia's values in regions of similar crustal properties.
When using geophysical characteristics of external regions to estimate heat flux, whether
by statistical correlation or via machine learning methods, it is necessary to choose the
region carefully such that it has physical and chemical characteristics as the region within
Antarctica. Models that use such methods (e.g., Shen et al. 2020, Stål et al. 2021) often use
a single continent to correlate with Antarctica; however, different portions of Antarctica
have affinities to different continents (e.g., Australia, India, southern Africa and possibly
North America; Goscombe et al. 2020), each with their own crustal architecture, mix of
rock types and histories. Such variations are likely to result in differences between the
physical properties of the regions (S. Jennings 2019, Gard et al. 2019) that result in con-
siderable differences in heat flux as observed in conjugate terranes (e.g., Jones 1987, 1988,
Nyblade et al. 1990, Ray et al. 2003, McLaren et al. 2003). South Australia, for example,
is known to have abnormally high heat production and associated heat flux (Hasterok &
Gard 2016, Pollett et al. 2019). Therefore, using Australia as a proxy would result in
much higher heat flux estimates than North America, which has a much less radiogenic
crust (Hasterok & Chapman 2007).

An ensemble model created by averaging many current models for Antarctic heat flux
(Figure 5.1). Such an approach has the advantage of producing more robust averages
where the models agree and reverting to the average where they disagree Burton-Johnson
et al. (2020). The ensemble model (Figure 5.1) shows a high GHF in most of West
Antarctica. There are also two small regional areas of high geothermal heat flux around

the Lambert Graben and Oates Land. In East Antarctica, there is little variability relative to most terranes of similar age on other continents. The estimated standard deviation in East Antarctica indicates minimal uncertainty between the six GHF models, with a standard deviation rarely exceeding $\pm$ 10 mW m^{-2}. The variation between models in West Antarctica is even poorer with an uncertainty exceeding $\pm$ 50 mW m^{-2}, mostly in West Antarctica where heat flux is high. While there are sizable differences between the models (Figure 5.1B), the models indicate GHF in West Antarctica is three to five times greater than East Antarctica.
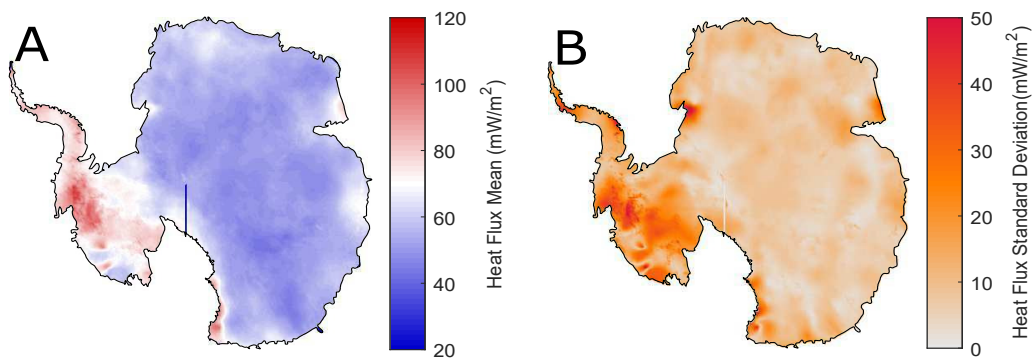
Figure 5.1: A) The mean of all six models heat flux estimates. B) The standard deviation between the six models heat flux estimates.

.

Comparing the heat flow distributions of the Antarctic ensemble with global observations (Davies 2013). The peak of the Antarctic distribution is $\sim$50 mW m^{-2}, $\sim$ 10 mW m^{-2} lower than the global peak (Figure 5.2). The Antarctic distribution of GHF is also narrower than the global distribution with 70% of Antarctica having a basal heat flux value in the range of 45–55 mW m^{-2}. Around 20% of Antarctic is found to have a higher basal heat flux value that 55 mW m^{-2} which represents the elevated GHF regions of West Antarctica Figure 5.1A. This elevated region has a wide spread of GHF values but comes up short of the highest values in the global GHF distribution. Antarctica, specifically East Antarctica, is found to have a narrower distribution of lower heat flux values than the global distribution. These differences could be real, due to a bias in either the global observations to tectonically active regions, or improper calibrations of geophysical proxies used to estimate the Antarctic GHF. Therefore, additional constraints on Antarctic GHF

have the potential to improve the confidence and/or accuracy of Antarctic models.
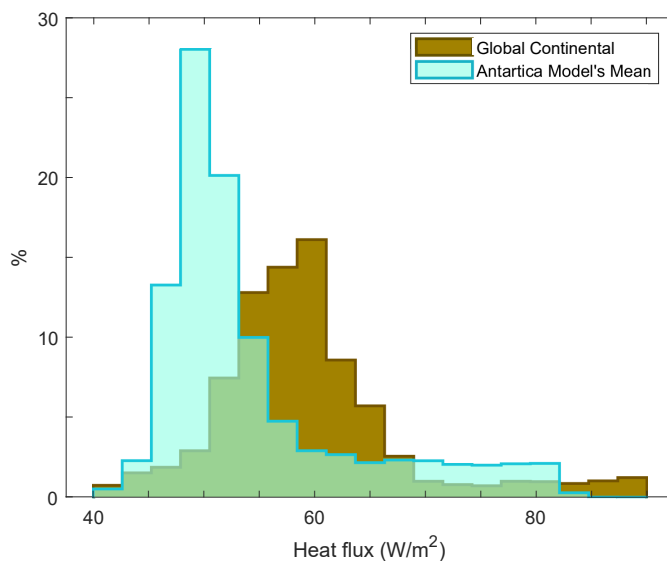
Figure 5.2: The distribution of average of six Antarctic geothermal heat flux models (Maule 2005, An et al. 2015, Martos et al. 2017, Guimarães et al. 2020, Shen et al. 2020, Stål et al. 2021) compared with the distribution of global continental heat flux values (Davies 2013).

Thus far, we have focused mainly on the constraints added by geophysical methods; however, the presence or absence of subglacial lakes also provides a constraint on the GHF at the base of the glacier. In their paper, Siegert & Dowdeswell (1996) used subglacial lakes locations to presume that the temperature at the base of the ice sheet is at the melting point; estimates the heat flux at 77 sites. Over 400 subglacial lakes have been identified beneath Antarctica from a combination of airborne radio-echo-sounding and satellite observations (Siegert 2005). Only 50% of Antarctica has been explored using the airborne method, so there may be many more lakes to be discovered. Furthermore, the method is limited to the $< 0.5\%$ of Antarctica's ice sheet known to lie above subglacial lakes (Siegert 2005).

Despite the limited area covered by subglacial lakes, the method gives us a basis for the basal heat flux constraint (BHFC) in regions where lakes are absent. Since GHF increases with geothermal temperature at the base of the ice sheet (Siegert & Dowdeswell 1996) and $> 99\%$ of Antarctic surface area not above a subglacial lake, temperatures must be less than the melting point, and consequently set the maximum BHFC bound

lest a subglacial lake can form. This study expands upon Siegert & Dowdeswell (1996) to map BHFC across Antarctica and produce a map to compare with existing GHF models. The result allows us to identify regions where Antarctic GHF is over-/underestimated by proxy estimates.

5.3 Methods

Vertical heat flux at the base of the ice sheet (q_b) can be calculated via Fourier law (Mony et al. 2020),

$$q_b = k_b \left(\frac{\partial T}{\partial z} \right)_b, \tag{5.1}$$

where k_b and $(\frac{\partial T}{\partial z})_b$ are the conductivity and thermal gradient at the base of the ice sheet respectably. We estimate the conductivity of ice at the base of the ice sheet using the following relation (Paterson 1994, Llubes et al. 2006),

$$k_b = 2.072 \exp\left(-5.7 \times 10^{-3} \, T_b\right), \tag{5.2}$$

where T_b is the basal temperature. To find the gradient at the base of the ice sheet, we first calculate the gradient throughout the entire ice sheet, which we estimated by solving the heat equation (Paterson 1994),

$$\kappa \frac{\partial T^2}{\partial z^2} - u\frac{\partial T}{\partial x} - w\frac{\partial T}{\partial z} + \frac{\tau_b z}{c_p \rho H}\frac{\partial u}{\partial z} = 0, \tag{5.3}$$

where κ is the thermal diffusivity, u and w are the horizontal and vertical ice velocities respectively, τ_b is the Geothermal shear stress, c_p is the specific heat capacity, ρ is the ice density and H is the thickness of the ice. Since all variables except τ_b and H depend on the temperature of the ice, we calculate the gradient using a ordinary differential equation (ODE) solution (Appendix B.1). We make a few additional assumptions to estimate the thermal gradient, including

- horizontal advection is negligible (Appendix B.1.4);

- minimal contaminates within the ice sheet, which prevents steep surface gradients and unreasonably low GHF caused by low ice conductivity in the upper ice sheet; and

- that refractive effects on heat flux caused by bedrock topography and geological contacts (Willcocks et al. 2021) are negligible.

To solve the ODE, a temperature boundary condition is required at both the surface and the base of the ice sheet.

Only limited surface temperature measurements have been collected across Antarctica, which requires a model to estimate temperatures across much of the continent. Furthermore, it is difficult to construct a meaningful surface boundary temperature due to the systematic increase in surface temperatures due to climate change (Turner et al. 2019). Therefore, we start the temperature profile at a depth (100 m) within the ice sheet that has not yet been affected by recent climate changes (Mony et al. 2020). To find the temperature at this depth, we use the empirical relation by Fortuin & Oerlemans (1990),

$$T_s(^\circ\mathrm{C}) = \begin{cases} -0.014285\,z_e - 0.180\,|L| + 7.405 \pm 3.9 & \text{for } z_e \le 1500 \text{ m} \\ -0.005102\,z_e - 0.725\,|L| + 36.689 \pm 3.5 & \text{for } 200 \le z_e < 1500 \text{ m} \\ -0.943\,|L| + 49.642 \pm 2.2 & \text{for } 200 \le z_e \text{ m,} \end{cases} \tag{5.4}$$

where z_e is the surface elevation (in metres) and L is the latitude (in degrees).

To determine the BHFC, the basal temperatures must be at the pressure melting point of ice in order. Thus, the basal temperature is determined by,

$$T_b = T_m = T_{tp} + \gamma(P_b - P_{tp}), \tag{5.5}$$

where P_b is the pressure at the base of the ice sheet, γ is the Clausius-Clapeyron constant and T_{tp}/P_{tp} is the triple point temperature and pressure of ice respectively.

To incorporate uncertainties in our calculations, a Monte Carlo analysis is used, perturbing each of the variables during each of 250 realisations. Where there are competing

models for parameters (e.g., advection and thermal conductivity), expressions are chosen that yield a larger value of GHF to ensure our model is the uppermost bound for GHF. From these realizations, we determine the BHFC mean and standard deviation at each point in a 10×10 km^2 grid across Antarctica.

5.4 Results

As with many geophysical parameters, there is a clear east-west dichotomy in the BHFC (Figure 5.3). BHFC is relatively low across East Antarctica with the lowest areas of heat flux found beneath the Dome Circle. In contrast, West Antarctica and coastal regions have much higher values of BHFC with the highest regions of BHFC found in the Antarctic Peninsular and the Transantarctic mountains. While West Antarctica as a whole has extremely high values of BHFC, there are small isolated regions of extremely low BHFC with values as low as 40 mW m^{-2}. The pattern of uncertainty is well-correlated with BHFC. The uncertainty in a majority of Antarctic's interior is around 20 mW m^{-2} but is much higher (>4 times) in coastal regions and West Antarctica. This high uncertainty coincides with the larger BHFC found in these regions and is likely driven by large uncertainties in the local input values in these regions, most notability velocity.
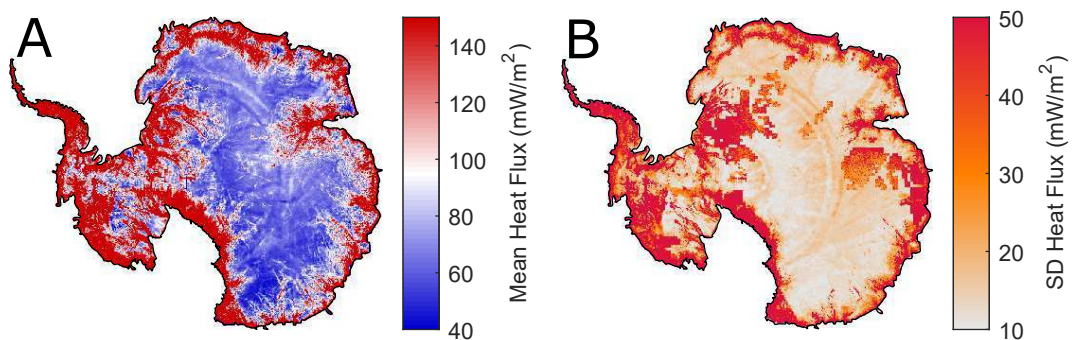
Figure 5.3: A) Basal heat flux constraint (BHFC) (in mW m^{-2}) such that ice at the bedrock boundary will remain frozen. B) Uncertainty in BHFC based on a Monte Carlo uncertainty analysis.

5.4.1   Thermal Profiles

Ice thickness and vertical velocity (advection) are the most important parameters when calculating the BHFC. However, advection has direct effect on the thermal profile whereas ice thickness is a consequence of the thermal state. Much of the interior of the continent has low BHFC values because advection is minimal and true GHF is low, resulting in thick ice. In contrast, coastal regions tend to have high BHFC values because of greater advection and transport of cold surface temperatures deep into the ice sheet, which requires steep thermal gradients to induce melting, especially when the ice is thin. For example, Figures 5.4B and C show thermal profiles in regions of high and low advection, respectively, showing the steeper gradients (high BHFC) at the base of the ice when the advection is high.
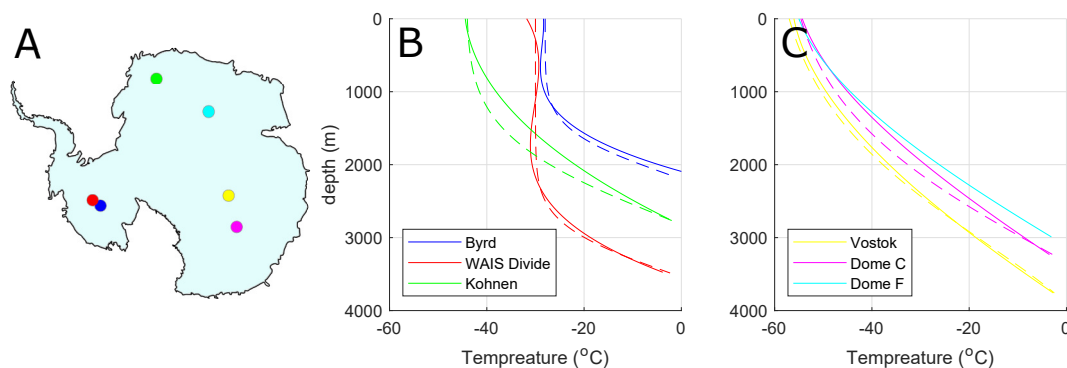
Figure 5.4: Selected drill sites with measured thermal profiles and the thermal profile associated with BHFC computations (Talalay et al. 2020). A) Map of sites B) Thermal profiles of three sites with high vertical advection (solid lines) and the computed thermal profiles from this study (dashed lines). C) Thermal profiles of three sites with low vertical advection (solid lines) and the computed thermal profiles from this study (dashed lines). Note, the profiles computed from this study are associated with the BHFC and should be more extreme than observed.

5.4.2   Comparison To Drill Core Estimates

Drill cores provide valuable validation of the BHFC model. There are 24 drill-core sites where the GHF has been determined by measuring the temperature profiles through the ice sheet (Guimarães et al. 2020). Comparing the difference in these measured results with the maximum interpolated HF at each site location (Table 5.4.2), we find that 17

of 24 sites have values lower than BHFC. The remaining seven sites have values of BHF greater than those of the BHFC of which three are also within the margin of error. BHFC should be higher than the observed GHF in the absence of basal melting and lower than GHF in the presence of lakes.

The BHFC estimates are generally supported by observations. Of the seven sites with elevated heat flux (Table 5.4.2), two are from the same location of Thwaites Glacier located on the coast of West Antarctica where high ice velocity can result in difficult to map geothermal profiles. Four of the sites (Byrd Station, Siple Dome, EPICA Dome C and Upper Vincennes) are within the margin of a single standard deviation of the BHFC showing that such results for GHF are not unreasonable. Unlike the other sites, Concordia Subglacial Lake is a known melting point, and thus its elevated GHF above BHFC is expected.

Among the 17 drill sites with lower GHF than BHFC (Table 5.4.2), only three are above lakes appearing to violate BHFC predictions. Lake Leon and Lake Vida are both suspected to have poor results due to being highly saline coastal lakes that are frequently exposed during the summer months when the ice sheet retreats (Doran et al. 2002), due to these unique properties (such as highly saline water freezing at temperatures as low as $-13\ ^\circ$C) the BHFC model is unusable in accurately constraining GHF. As for the third site, Lake Vostok, the GHF is within one standard deviation below BHFC and perhaps resulting from our prioritising the inputs into BHFC to create a definitive upper bound for GHF across most of Antarctica. Therefore, BHFC may only be skewed too values that are too high in the vicinity of Lake Vostok.

5.5 Discussion

The BHFC works best on proxy-based GHF models in regions where the magnitude and standard deviation of BHFC are low. The best constraints are found in the East Antarctic interior with a few more local regions in West Antarctica. In many regions of West Antarctica and along the coasts, BHFC is a poor constraint because the magnitude and uncertainty is generally higher than reasonable for most continental regions (Figure 5.3).

Table 5.1: The measured geothermal heat flux values in Antarctica (Guimarães et al. 2020) compared to the estimated maximum geothermal heat flux. Site names associated with subglacial lakes are italicized. BHFC values in bold are less than observed heat flux.

Core Site	Lat	Lon	Measured GHF ($mW\ m^{-2}$)	BHFC mean ($mW\ m^{-2}$)	SD ($mW\ m^{-2}$)
DVDP-14/North Fork	-77.54	-161.41	142	$> 10^3$	$> 10^3$
DVDP-12/Lake Leon	-77.63	-162.85	100	$> 10^3$	$> 10^3$
Nagursk-1	-80.78	-47.71	57	69.2	15.8
Nagursk-1.2	-88.37	168.62	54	78.4	10.05
McMurdo	-77.76	-162.28	115	$> 10^3$	$> 10^3$
Thwaites Glacier WA	-75.50	-106.80	114	**63.2**	14.26
Concordia Subglacial Lake	-74.05	-125.05	100	**55.2**	14.74
Dyer Plateau	-70.50	65.00	100	181	54.42
Thwaites Glacier WA	-75.50	-106.80	97	**63.2**	14.26
Lake Vida	-77.82	-161.81	85	$> 10^3$	$> 10^3$
McMurdo Ice Shelf	-77.76	-162.28	82	$> 10^3$	$> 10^3$
Byrd Station	-80.01	119.52	75	**63.3**	10.20
Law Dome	-66.76	-112.80	75	86.5	24.47
Siple Dome	-81.65	148.81	69	**57.6**	14.23
EPICA Dome C	-75.10	-123.40	67	**60.2**	14.65
Upper Vincennes	-73.50	-122.00	65	**57.0**	14.22
South Pole	-90.00	0.00	61	90.9	13.11
Dome F	-75.10	-39.70	59	66.3	11.96
Lake Vostok	-78.45	-106.87	53	62.8	15.11
EPICA Dome C 1	-75.10	-23.40	45	71.3	35.22
Concordia Trench Dome C	-74.05	-125.05	40	54.8	14.64
Dome C Area	-75.12	-123.83	40	60.6	14.75
Lower Vincennes	-73.50	-122.00	40	57.0	14.23
Vestfold Hills Block	-68.68	-78.25	31	$> 10^3$	$> 10^3$

Such high values are the result of rapidly flowing ice. The discussion that follows focuses on regions with moderate BHFC and the accuracy of proxy-based GHF models for Antarctica.

5.5.1 Constraints on Proxy-based GHF Models

To aid with interpretation, we centre the proxy GHF, Q_i, about the mean BHFC, Q_{BC}, and rescale by the standard deviation of BHFC, Q_{SD},

$$Q_{\text{diff}} = \frac{Q_i - Q_{BC}}{Q_{SD}}. \tag{5.6}$$

For example, a value of 1.5 indicates the proxy GHF is 1.5 standard deviations greater than the mean BHFC. This formulation allows us to assess the differences in BHFC and GHF within their uncertainties. Therefore, we do not consider values of GHF greater than BHFC inaccurate except where the values are towards the upper end of the BHFC + 2SD range. To further quantify our results further we establish the following four categories:

- Q1: $Q_{\text{diff}} < -2$, i.e., Q_i falls below BHFC with a confidence of 98%;

- Q2: -2 $\leq Q_{\text{diff}} < 0$, i.e., Q_i falls below the BCHF but lies within the margin of error;

- Q3: $0 \leq Q_{\text{diff}} \leq 2$, i.e., Q_i lies above the BCHF but lies within the margin of error; and

- Q4: $2 < Q_{\text{diff}}$, i.e., Q_i lies above BHFC with a confidence of 98%.

Using the ensemble proxy-based GHF model, we find most regions fall below BHFC as expected (Figure 5.5A). Regions that predict values of Antarctic GHF much lower than BHFC include the Transantartic Mountains, Lambert Graben, Enderby Land, Wilkes Land and the Antarctic Peninsula. Regions that predict values of Antarctic GHF close to or exceeding BHFC include Marie Byrd Land, Dronning Maud Land, west coast of the Amery Ice Shelf and a large region surrounding the Dome Circle. Areas where the Antarctic GHF model is greater than this BHFC are likely overestimated by proxy methods, since basal temperatures would otherwise exceed the melting point.
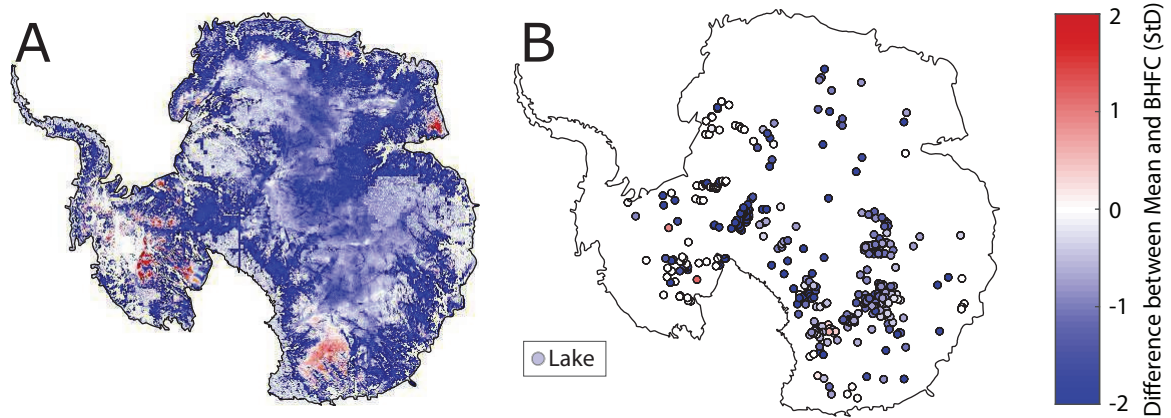
Figure 5.5: A) Difference between the ensemble GHF and BHFC normalized by the BHFC standard deviation (Equation 5.6). Positive values occur where the estimated GHF is greater than BHFC. B) Map of subglacial lake locations and the corresponding difference between the GHF and BHFC at the lake site.

Across all six proxy models Q_{diff} is less than/much less than the BHFC (Table 5.2). Most proxy models exceed the BCHF in <7% of Antarctica's surface area (<14% including Martos et al. 2017). Very few regions exceed BHFC by two standard deviations (Q4 bin, Table 5.2). The majority of regions have Q_{diff} within bin Q2 with roughly one-quarter in bin Q1, regardless of the proxy model. Therefore, we confidently assert that roughly 95% of the Antarctica area predicted by current GHF proxy models satisfies our BHFC. However, in the vicinity of lakes, a proxy-based estimate of the GHF should exceed the BHFC.

Table 5.2: Performance of geophysical proxy-based estimates geothermal heat flux (GHF) relative to the basal heat flux constraint (BHFC) using binned Q_{diff} as defined in Section 5.5.1. The results are presented for the entirety of Antarctica and separately at lake locations as a percentage of total surface area and a percentage of lake sites, respectively.

Model	Antarctica				at lakes		
	Q1	Q2	Q3	Q4	Q1	Q2	Q3
Maule (2005)	35.9	58.4	4.5	0.9	24.6	56.2	19.2
An et al. (2015)	28.1	68.1	3.4	0.1	18.9	60.9	20.2
Martos et al. (2017)	19.6	66.2	12.0	1.7	13.8	54.1	30.1
Guimarães et al. (2020)	23.2	69.4	6.4	0.7	14.5	64.2	20.8
Shen et al. (2020)	27.5	69.0	2.9	0.2	18.7	62.6	18.7
Stål et al. (2021)	22.9	70.0	6.1	0.6	15.7	62.8	21.5
ensemble	24.2	70.6	4.5	0.3	15.8	64.6	19.6

Lakes should occur in regions with elevated Q_{diff}, though few do (Table 5.2). Q_{diff} is

below Q4 at all lakes—none unequivocally above BHFC, regardless of the proxy method. This result is not surprising as melting rates in regions with GHF well above BHFC would be unrealistically high. However, at most 30% of GHF estimates at lakes fall within the Q3 bin (Table 5.2). As we have biased our BHFC to higher values the number could be somewhat higher. Regardless, the relatively few lakes exceeding BHFC is problematic because it implies GHF is insufficient to produce lakes where most exist. There are clear regional differences in Q_{diff} among the clusters of lakes (Figure 5.5B). For instance, Q_{diff} at lakes near the South Pole lie within the Q1 bin, representing an extremely low GHF anomaly. Regions found around Dome C and Lake Vostok are notable for the high density of lakes despite few with GHF close to BHFC. In contrast, most lakes in Coats Land and West Antarctica have values of Q_{diff} close to, or above BCHF.

Most lakes that satisfy BHFC are active lakes (77.22% of lakes with positive Q_{diff}). Active lakes are characterized by their changing water level due to drainage/infill resulting in topographic changes at the surface of the ice sheet (Gray 2005). While active lakes are found across Antarctica (MacKie et al. 2020), they are the majority of lakes in Coats Land and Marie Byrd Land (West Antarctica), which also satisfy BHFC. Passive lakes are formed where the geothermal gradient is high enough to passively melt basal ice. The association of positive Q_{diff} in the vicinity of active lakes and negative at passive lakes runs contrary to their respective hypothesised methods of formation. We interpret poor of proxy-based GHF models with BHFC as an underprediction of GHF near lake occurrences in East Antarctica. Because proxy-based GHF is below BHFC in regions devoid of lakes, the low GHF predictions are predominantly found in some regions. Hence, we argue for greater variability in GHF than proxy-based models currently predict.

Observations of GHF from conjugate terranes are consistent with a larger variability in East Antarctic GHF than currently predicted by proxy-based methods (Figure 5.6). A study by (Pollett et al. 2019) first suggested that paleogeographic reconstructions can be used to predict heat flow across conjugate margins, demonstrating that the correlation between existing proxy-based GHF models poorly matched conjugate heat flux in Antarctica. For instance, The gondwana reconstruction shows observed heat flux is much higher

in eastern Australia than proxies predict in George V Land and Terre Adélie (Figure 5.6). Additionally, the model by Martos et al. (2017) is considerably higher in the Wilkes Basin than observed in the Yilgarn Craton and the model by An et al. (2015) is much higher in the Napier Complex than is observed in southern India. There are several other regions where one or both proxies appear to poorly fit conjugate heat flux observations. Because many of these regional connections are Precambrian terranes, we assume any mantle thermal signal to have long since decayed. Variations in thermal properties, especially heat production, are likely the source of these observed heat flux variations. In fact, Australia has some of the largest variations in continental heat production on Earth (Hasterok & Gard 2016, Gard et al. 2019)—terranes which were once contiguous with ones now beneath the Antarctic ice. Even when statistical correlations of geophysical proxies between continents are used to accurately calibrate heat flux (i.e., Shen et al. (2020) and Stål et al. (2021)), observed heat flux variations can be large despite an accurate mean value assigned to Antarctica (Figure 3A inset, Shen et al. 2020). Because all the proxy-based GHF estimates do not, or cannot account for heat production variability, the heat flux variability in Antarctica is likely underpredicted. This interpretation is consistent with our calculations discussed above.
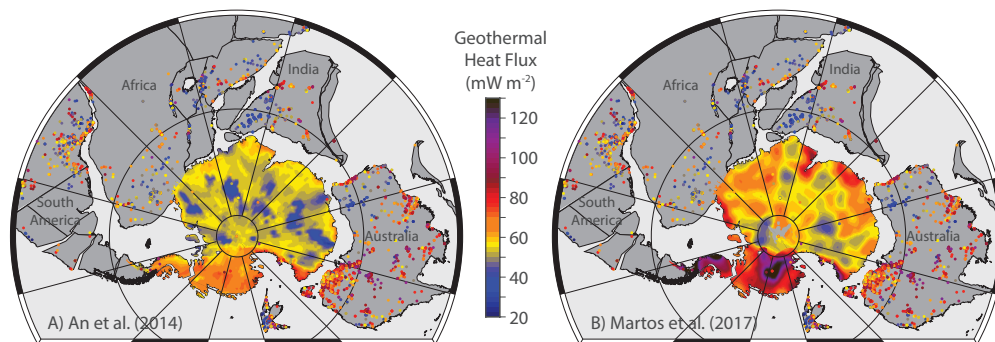
Figure 5.6: The proxy-based GHF models of An et al. (2015) and Martos et al. (2017) compared with GHF observations from conjugate terranes in South America, South Africa, India and Australia. The locations of conjugate continents are shown at 165 Ma (Matthews et al. 2016). Heat flow data from www.heatflow.org. Note the mismatch in heat flow between adjacent regions of Antarctica and conjugate margins.

Local effects can occur below the current resolution of GHF proxies that can also lead to mismatch between BHFC and GHF predictions at lakes. While the large number of lakes detected in regions of insufficient GHF, both the BHFC and GHF estimates use a

grid spacing of 10×10 km the vast majority of lakes have maximum width of less than 5×5 km (Wright & Siegert 2012). Thus, it is possible that localized GHF highs that exceed BHFC due to thermal refraction (e.g., Willcocks et al. 2021) may be missed by the low resolution. Melt runoff transported to regions of low topography further afield could also be found in regions of without elevated Q_{diff}.

Another effect not addressed by the BHFC is the effect of bedrock erosion on GHF (Ehlers 2005). For most of the Antarctica where horizontal velocities are less than 25 m a^{-1} (Figure 5.7) the average erosion is predicted to be less than 2 mm a^{-1} (Cook et al. 2020). For a duration of 20 ka, the erosional effect on heat flow is $<10\%$ (Figure 5d, Ehlers 2005). However, in coastal regions where faster ice velocities are may exceed 100 mm a^{-1} it is necessary to account for the erosional effect to accurately estimate GHF. Since our model does not account for subglacial erosion effects the BHFC can only accurately be applied to the continental interior.
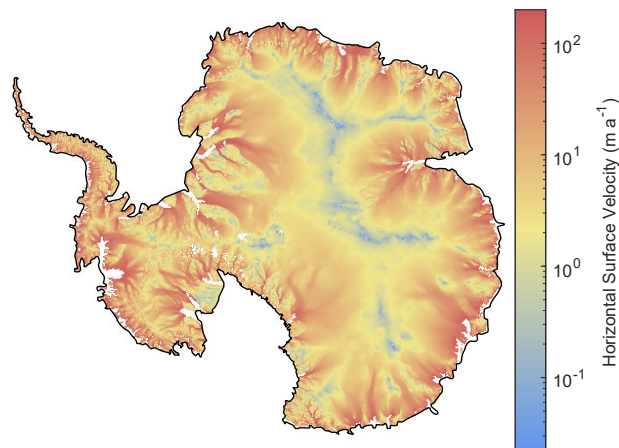
Figure 5.7: Horizontal surface velocity of the Antarctic ice sheet (Palmer et al. 2013).

5.5.2 Future Improvement

Improving models of GHF can be made by collecting additional observations at key sites, incorporating regional variations in proxy-based calculations and improving the inputs to BHFC models. Key localities for drilling in Antarctica may include terranes with

thermally well-characterised conjugate margins. These sites will allow one to assess the validity of thermal connections. Additional observational constraints will also be useful in regions near compositional boundaries (e.g., major suture zones) to test the impact of thermal refraction from thermal conductivity variations in bedrock. Since drilling is an expensive endeavour dependent upon scarce funding, BHFC will continue to be a helpful constraint for proxy-based GHF estimates.

Empirical proxy-based GHF models can be improved by implementing regional variations in physical properties—heat production and thermal conductivity. Creating regional models can be difficult because thermal properties cannot be remotely sensed directly. However, several studies in the past decade have developed empirical predictors for physical properties including seismic velocity, density, and rock age (S. Jennings 2019, Gard et al. 2019), which can be remotely sensed or inferred. To improve statistically-based GHF estimates, one could employ Bayesian techniques that could produce a distribution of models that allow for the probability distribution of heat flux.

While we use our BHFC model as a constraint on current GHF proxy models, we acknowledge our model's limitations. Improvements to the BHFC can be improved by reducing the number of assumptions involved in the calculations by reducing dataset uncertainties and improving physical models of processes. The surface temperature (T_s) is calculated from topography and is not measured directly. The model also ignored horizontal advection for simplicity and, while often factor insignificant, it can become a notable factor in regions of high horizontal velocity (i.e., many coastal regions). While the horizontal surface velocity (u_s) of ice is observed by GPS and satellite observations, the vertical velocity is calculated from the change in horizontal velocity (Appendix B.1.2). This calculation can introduce inaccuracies as some terms are not well constrained. The formulation that we use for the glacial heat equation does not take into account convection within the ice sheet as the study by Hughes (2012) suggested is significant. Despite these uncertainties, we remain confident that the results accurately represent a clear upper bound for ice basal melting GHF across Antarctica.

As GHF models improve, it may be possible to compare GHF models with the BHFC

to predict locations of undiscovered lakes. GHF constraint plots such as these could be extremely useful in current attempts to model ideal environments for subglacial lakes to be found in both Antarctica and Greenland (Miles et al. 2017), as these models can identify regions where melting occurs, but the water is transported elsewhere without forming lakes.

5.6 Conclusions

We have demonstrated that the basal heat flux constraint (BHFC), assuming base of the ice sheet is at the melting point, is a useful constraint on Antarctica geothermal heat flux (GHF) models. There are very few places where the GHF proxy estimates exceed the BHFC as expected. In regions where there are many subglacial lakes, GHF should exceeded the BHFC as melt is present. In this regard, the GHF models perform poorly in much of East Antarctica, which we suggest indicates an underestimate of GHF in many regions. We suggest these regions with underpredicted GHF lack variability due to the use of uniform physical properties in empirical calculations or the use of means for statistical correlations. As GHF is an important boundary condition on the dynamics of ice sheets, it is important that future proxy-based models of GHF incorporate bounds placed by the presence or absence of melts at the base of the ice sheets. Until proxy-based GHF models improve these issues, we suggest ice sheet modelers incorporate higher variability, and greater magnitudes of GHF estimates beneath the East Antarctica ice sheet near lakes.

Statement of Authorship

Title of Paper	Prediction of subglacial lake melt source regions from site characteristics
Publication Status	☐ Published ⬤ Accepted for Publication ◯ Submitted for Publication ☐ Unpublished and Unsubmitted work written in manuscript style
Publication Details	

Principal Author

Name of Principal Author (Candidate)	Simon Robert Willcocks
Contribution to the Paper	Concerted the idea, wrote main paper, developed all models and generated figures.
Overall percentage (%)	90%
Certification:	This paper reports on original research I conducted during the period of my Higher Degree by Research candidature and is not subject to any obligations or contractual agreements with a third party that would constrain its inclusion in this thesis. I am the primary author of this paper.
Signature	Date 17/12/22

Co-Author Contributions

By signing the Statement of Authorship, each author certifies that:

i. the candidate's stated contribution to the publication is accurate (as detailed above);

ii. permission is granted for the candidate in include the publication in the thesis; and

iii. the sum of all co-author contributions is equal to 100% less the candidate's stated contribution.

Name of Co-Author	Derrick Hasterok
Contribution to the Paper	Supervised paper, proofread and adjusted the final text and figures
Signature	Date 20 Nov 2022

Name of Co-Author	
Contribution to the Paper	
Signature	Date

Please cut and paste additional co-author panels here as required.

Chapter 6

Prediction of subglacial lake melt source regions from site characteristics

Abstract

Subglacial melt has important implications for ice sheet dynamics. Locating and identifying subglacial lakes is expensive and time-consuming, requiring radar surveys or satellite methods. We explore three methods to identify source regions for lakes using seven continent-wide environmental characteristics that are sensitive to, or influenced by ice sheet temperature. A simple comparison of environmental properties at lake locations with their continent-wide distributions suggests a statistical relationship (high Kolmogorov-Smirnov statistic) between stable lake locations and ice thickness and surface temperatures, indicating melting under passive conditions. Active lakes, in contrast, show little correlation to direct thermally influenced parameters, instead exhibiting large statistical differences with horizontal velocity and bed elevation. More sophisticated techniques, including principal component analysis (PCA) and machine learning (ML) classification, provide better spatial identification of lake types. Positive PCA scores derived from the environmental characteristics correlate with stable lakes whereas negative values corre-

spond to active lakes. ML methods can also identify regions where subglacial lake melt sources are likely. While ML provides the most accurate classification maps, the combination of approaches adds a deeper knowledge of the primary controls on lake formation and the environmental settings in which they are likely to be found.

6.1   Introduction

Since the confirmation of subglacial lakes existence in the late 1960's (Robin et al. 1970), 675 subglacial lakes have been discovered beneath the Antarctic Ice Sheet (Livingstone et al. 2022). Multiple studies have targeted these lakes because of their unique isolated environments buried under kilometres of ice and their influence on glacial dynamics (Humbert et al. 2018, Couston 2021). For example, subglacial lakes have been shown to affect ice velocity (Stearns et al. 2008). Additionally, subglacial lakes reduce bedrock friction (Gudlaugsson et al. 2016) and increase heat transfer at the bedrock/ice interface (Pattyn et al. 2016). Subglacial lakes may portend more regional melting that have implications for subglacial hydrology and hydrogeology (Wright et al. 2012, Ashmore & Bingham 2014, Fricker et al. 2016) that can perturb the solid Earth temperature field (Siegert et al. 2017). Additionally, subglacial lakes are also sites of extreme environments that host life, serving as an analogue of possible life on icy moons (Siegert et al. 2001, Christner et al. 2014, Thatje et al. 2019).

The vast majority of known subglacial lakes have been identified by remote sensing techniques. Radio-echo sounding (RES) Siegert (2000) is the most effective method for detecting subglacial lakes. RES is an indirect observation technique that relies on radio waves to penetrate the ice sheet and reflect off sub-glacial water bodies. Smaller lakes can be difficult to resolve using this method as they blend into the bedrock background (Magnússon et al. 2021). Ephemeral lakes resulting from seasonal filling and drainage of basins may not be captured by RES, instead these active lakes are more commonly discovered by satellite altimetry by the changes in ice elevation and specific surface morphology (Gray 2005, Fricker et al. 2007, Horgan et al. 2012).

Despite the discovery of numerous subglacial lakes, many have likely gone undiscovered

(Goeller et al. 2016, MacKie et al. 2020). For comparison, Canada is roughly 75% of the land area of Antarctica, yet has nearly 880,000 lakes, most of which are glacial (Messager et al. 2016). Scandinavia, though much smaller, has a similar spatial density of lakes as Canada (Messager et al. 2016). While an ice sheet still covers Antarctica and the bed remains frozen over much of the continent (maximum estimated area covered by lakes 95% Siegert 2000, Goeller et al. 2016), there are likely many more subglacial lakes beneath the Antarctic Ice Sheet due to limitations presented by current detection methods (MacKie et al. 2020).

Because neither remote-sensing technique is likely to identify all existing lakes, multivariate and machine-learning methods have been demonstrated to help identify favourable lake-forming environments (Rodriguez-Galiano et al. 2015). For example, MacKie et al. (2020) used logistic regression trained using five environmental variables and several derivative parameters to refine estimates of locations and areas of subglacial lakes. Their result provides a minimum estimate of 0.32% of Antarctica covered by subglacial lakes. However, this result will only be a fraction of the total area of melting at the base of the ice sheet.

In this study, we build upon these previous studies to explore seven site characteristics that contribute to the thermal state of the ice sheet to develop multivariate methods to predict the source regions and classification of subglacial lake melt sources. Our tests include comparison between distributions of individual variables at lakes with greater Antarctica, principal component analysis, and machine learning using the Sub-space KNN method. From these tests, we develop three separate models of subglacial lake melt source identification that can be applied to subglacial environments.

6.2 Background

6.2.1 Subglacial Lakes

Subglacial lakes are classified as active or stable (Figure 6.1), where stable lakes can be identified via RES (Oswald & Robin 1973, Carter et al. 2007, Wright & Siegert 2012) and

active lakes by satellite observations of ice elevation (Gray 2005). Stable subglacial lakes are believed to have formed when the melting point is reached under a geothermal gradient (Siegert 2000). With the exception of near-surface effects, the temperature increases with depth in ice (Paterson 1994). This increase in temperature results in the ice exceeding its pressure melting point under sufficiently thick ice, which then melts and collects in a low region to form a subglacial lake. For a typical geothermal gradient (with a surface temperature of -50 °C, ice thermal conductivity of 2.3 W m^{-1} K^{-1} and basal heat flux of 40 mW m^{-2}), the melting point is roughly located at a depth of around 2.5 km, based on a simple back of the envelope estimates using the heat equation, though this varies depending on regional heat flux (An et al. 2015, Martos et al. 2017) and local environmental factors such as surface temperature (King & Turner 1997), ice velocity, mass accumulation rates (Llubes et al. 2006) and subglacial geology (Willcocks et al. 2021). Active lakes—lakes where water is actively transported into or out of the lake— lead to the overlying ice sheet being raised/lowered accordingly due to ice buoyancy (Horgan et al. 2012). Since these types of lakes may result from inflow of external water sources, it is possible for lakes to form irrespective of the geothermal environment. Due to the transient nature of these lakes, active lakes can be temporary or seasonal (Lai et al. 2021).

6.2.2   Predictive Studies

Previous attempts at predictive models have included Livingstone et al. (2013) and Goeller et al. (2016) who both use the hydraulic potential to identify the drainage pathways under the Antarctic Ice Sheet and locate points of pooling above bedrock. Goeller et al. (2016) identified 10,183 potential lake locations. Both models identified around 4-5% of the Antarctic Ice Sheet base to lie above a region where water can pool in the bedrock. Livingstone et al. (2013) was able to reduce this percentage down to 2.7% by removing pooling locations where temperatures would be too cold for liquid water while Goeller et al. (2016) was able to reduce the percentage down to 0.6% by scaling the predicted lakes down to match those of known lake locations. Both of these models are highly
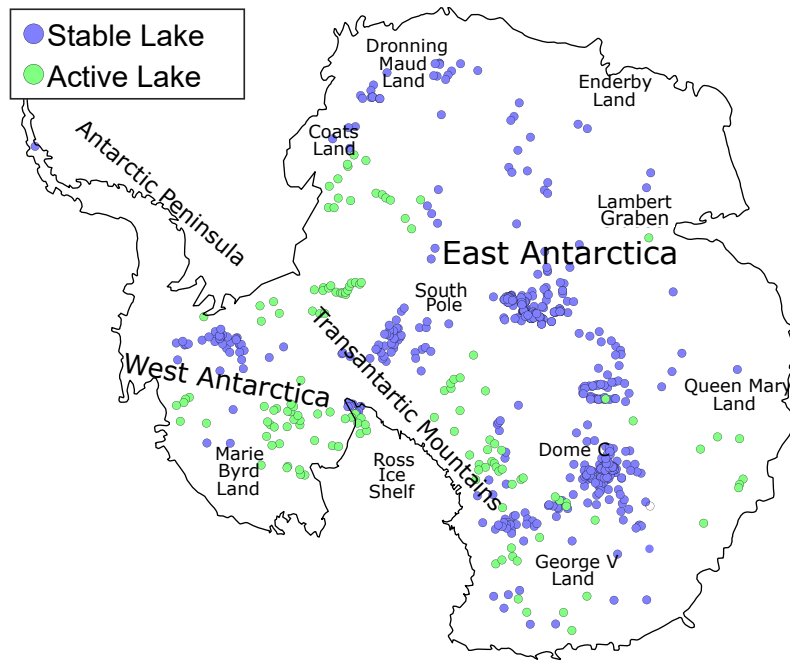
Figure 6.1: Map of subglacial lake locations across Antarctica categorized into active (with active water inflows/outflows) and stable (with constant water levels). There are 535 stable and 140 active lakes. Lake locations and designations from Livingstone et al. (2022).

dependent on the Bedmap2 dataset (Fretwell et al. 2013), which has an unrealistically smooth bed topography due to interpolation (MacKie et al. 2020).

To address some of these issues, MacKie et al. (2020) used machine learning methods to incorporate additional datasets to refine the number of lakes. To improve the limitations of the Bedmap2 dataset, MacKie et al. (2020) generated more realistic bedrock topography by simulating small-scale roughness via Fourier analysis. Derivative parameters including bed slope and curvature of hydraulic potential were then incorporated into their analysis. In addition, MacKie et al. (2020) included heat flux, ice velocity, strain, curvature of hydraulic potential, ice surface slope, ice thickness, flow accumulation models, and the distance along the ice flow path from the grounding line to form a linear regression. The estimated area covered by subglacial lakes in this study ranges from 0.32 to 0.6%. However, not all of these variables contribute meaningfully to the analysis.

We take a broader perspective, focusing not simply on lakes but on their source potential, that is, the base of the ice sheet that is melting and contributes to lake formation. We use the more recent and higher resolution topography of BedMachine (Morlighem

et al. 2019) and examine several recent models of geothermal heat flux.

6.3   Datasets

To classify the formation environment of subglacial lakes, we examine the seven site characteristics shown in Figure 6.2. These parameters are chosen as direct or indirect proxies for temperature or thermal state at the ice sheet bed and can be easily observed/estimated. To prepare each dataset for analysis, they were projected onto Antarctic polar stereographic coordinates and interpolated into a common grid with a discretization of 10 km $\times$ 10 km.
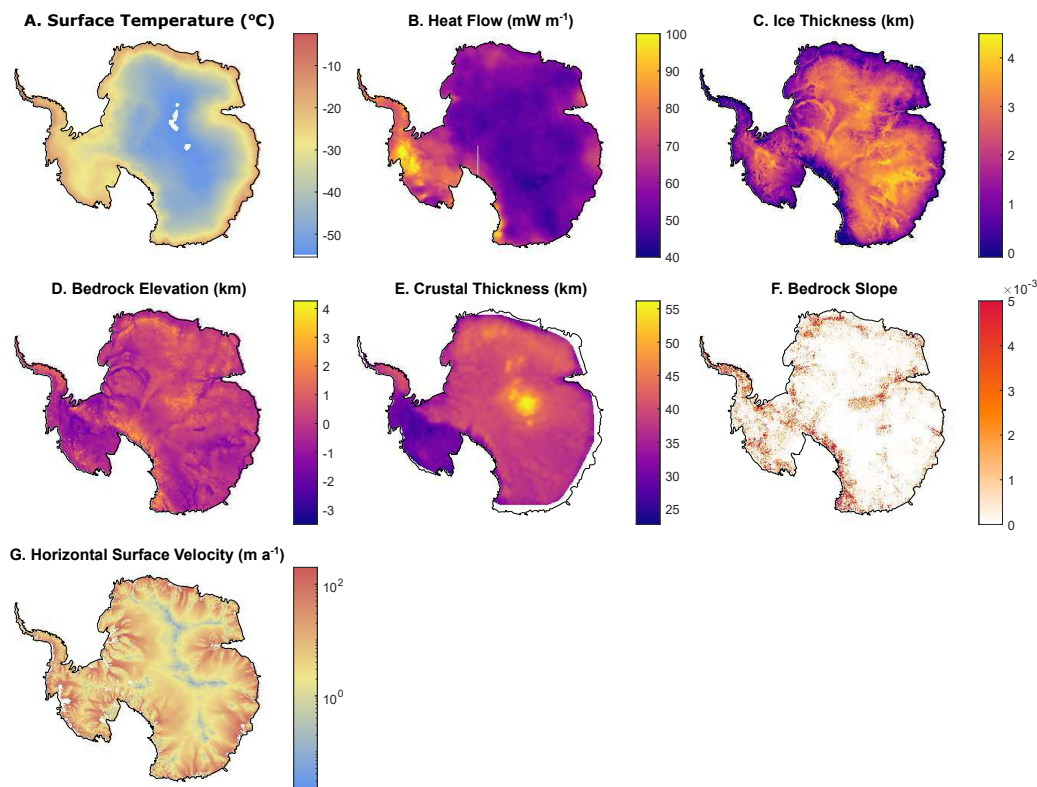
Figure 6.2: Datasets used for developing lake melt source classification: ice thickness (C), bed rock elevation (D) and bedrock slope (F) have all been taken from Morlighem et al. (2019). Surface temperature (A) is an averaging of multiple temperature measurements dating from 1979-2011 van Wessem et al. (2014). Heat flow (B) is an ensemble average from the following sources Maule (2005), An et al. (2015), Martos et al. (2017), Shen et al. (2020), Guimarães et al. (2020), Stål et al. (2021). Crustal thickness (E) from Baranov et al. (2017). Horizontal surface velocity (G) is from Palmer et al. (2013).

Surface temperature, is an important boundary condition that influences the depth at

which melting is reached under a positive thermal gradient. Temperature was recorded by averaging the updated Regional Atmospheric Climate Model (RACMO2) over a 32 year period (1979-2011) (van Wessem et al. 2014). In Antarctica, the estimated surface temperature ranges from -5 to -60 °C, with the former being closer to the melting point. Therefore, we expect that lakes are more likely to be in regions of warmer surface temperatures.

Basal temperatures of the ice sheet are influenced by the solid-Earth geothermal gradient (Paterson 1994). Because there are relatively few direct estimates of Antarctic geothermal heat flux, we average six published geophysical proxy-based estimates of heat flux. We do this by interpolating all six models into the same 10 km × 10 km used by all other samples and then finding the mean heat flux in each cell. This ensemble heat flux map may improve the average by reinforcing heat flux estimates where they agree and averaging out large contrasting anomalies where the models poorly agree (Supplementary Methods). These models include a satellite-based magnetic Curie depth model (Maule 2005), shear-wave tomography model (An et al. 2015), Curie airborne-based magnetic model (Martos et al. 2017), an interpolated model based on current core heat flux measurements (Guimarães et al. 2020) and two empirical seismic similarity models (Shen et al. 2020, Stål et al. 2021).

Although the heat flux is proportional to the thermal gradient, the absolute temperature at depth is critical for melting. Therefore, the thickness of the ice is also an important characteristic of the site to consider. For ice thickness, we use the BedMachine model (Morlighem et al. 2019), which is higher resolution than the earlier Bedmap2 (Fretwell et al. 2013). While the depth at which melting will occur differs from region to region, we expect many areas of thick ice to have lake melt sources due to the vast depth causing even the lowest thermal gradients to reach the melting point of ice.

Large-scale elevation variations can be sensitive to tectonic activity and/or reflect thermal gradients in the lithosphere beneath (An et al. 2015, Hasterok & Chapman 2011, Hasterok & Gard 2016). Although the ice represents a relatively uniform cover in the interior, bed elevation may help identify hidden thermal contributions to lithospheric

buoyancy. The link between elevation and thermal structure can be complicated by variations in compositional buoyancy (lateral variations in crustal thickness and rock density). Furthermore, we do not expect to find lake melt sources in regions of the highest topography, since surface ice is often too thin and/or surface temperatures are too cold for a sufficient gradient to create a lake melt source in these environments. We use BedMachine (Morlighem et al. 2019) as the bed elevation model.

Crustal thickness can also be used as a proxy for tectonically active/stable regions and reflects total radiogenic heat flux (Hasterok & Webb 2017, Goes et al. 2020). We acknowledge that the link between the crustal thickness and the lithospheric thermal state can be tenuous, especially at the global scale (Mareschal & Jaupart 2013), but there are good reasons to suspect that it may be a reasonable assumption beneath Antarctica. First, the Cenozoic West Antarctic Rift has a thin crust and an estimated high geothermal heat flux (Jordan et al. 2020, Behrendt 1999). The older East Antarctica has thicker crust and lower geothermal heat flux (Krynauw 1996). Second, the mantle has about an order of magnitude lower concentrations of heat producing elements than the crust, so a thick crust may have higher radiogenic heat flux. We use the crustal thickness model by Baranov et al. (2017), which has a grid spacing of 10 km × 10 km.

Furthermore, we will examine the topographic bedrock slope around lakes, as some models predict that topography can focus heat flux into valleys and away from peaks (van der Veen et al. 2007). If correct, we expect to see lake melt sources in areas of extreme topography changes due to the amplification it causes in local heat flux at the base of valleys where lakes would not originally form (Palmer et al. 2013). We define the topographic bedrock slope as the magnitudes of the change in bed elevation using the following equation:

$$R = \sqrt{\left(\frac{\partial z}{\partial x}\right)^2 + \left(\frac{\partial z}{\partial y}\right)^2}, \tag{6.1}$$

with respect to the slope in orthogonal directions.

Llubes et al. (2006) demonstrates how ice velocity in both the horizontal and vertical direction directly influence the thermal profiles via advection dissipation and basal friction. Since measuring velocity throughout the ice is impractical, we use surface velocities as a

proxy for the underlying velocity values in the glaciers (Wolff & Doake 1986) as well as the thermal effects it applies. The surface velocity of the ice in the horizontal direction is taken from Rignot (2019). Since there is a high correlation between horizontal and vertical velocity, we used horizontal surface velocity as a proxy for both directions.

Complex physical processes can make it difficult to directly link these thermally sensitive proxies to temperature. Thus, the use of multidimensional methods can potentially reveal patterns between proxies that simpler analyses cannot.

6.4 Methods

We explore three techniques to characterise environments associated with subglacial lakes: (1) comparative analysis, the simplest and least rigorous; (2) principal component analysis, a multivariate method; and (3) machine learning methods, the most sophisticated method, though with less clear causal connections between observations and predictions.

6.4.1 Comparative Analysis

When examining environmental parameters individually, specific parameters are expected to be identified as critical to an ideal lake melt source. We compared the distribution of lake parameters (both active and stable) against the whole of Antarctica with a resolution of 10 km × 10 km. Comparisons are made both visually and using the two-sample Kolmogorov-Smirnov (KS) statistic. Low KS values suggest similar distributions and therefore little influence of the environmental variable on lake melt source formation. High KS values indicate greater differences between the distributions and may indicate an influence of the environmental variable on lake melt source formation or as a possible predictor of lake occurrence (Maguire et al. 2021).

6.4.2 Principal Component Analysis

Principal component analysis (PCA) is a multidimensional method that determines a set of linear basis vectors that can be used to discriminate data. We use it in order to examine

the source of variance in the data and separate Antarctic regions based on the likelihood of finding active lake melt source, stable lake melt source, or no melt source at all. We perform a PCA to account for the fact that no single environmental variable can describe an ideal lake melt source environment. It is also used as a precondition to reduce noise in some of the machine learning experiments.

There are significant variations in the magnitudes and ranges of each of the variables with respect to each other, which can make it more difficult to resolve the sources of variance. To account for this, we centre and normalise all parameters by

$$\hat{x}_i = \frac{x_i - \bar{x}_i}{\sigma_{x_i}}, \tag{6.2}$$

where x_i is the observed data, $\bar{x}_i$ is the mean and σ_{x_i} is the standard deviation. Rather than use $\bar{x}_i$ and σ_{x_i} from the lakes, we use the parameters calculated from the Antarctic grids to perform the PCA analysis. This choice gives us a series of values for each of the lake parameters standardised in relation to Antarctica as a whole. It also ensures that as the database of lakes grows, the PCA vectors need not change. Using these unitless variables, we conduct a principal component analysis on the normalized parameters to create a set of eigenvectors and eigenvalues for our principal axes. We then compare the scores of lakes with those of greater Antarctica to identify regions with high potential for lake melt sources.

6.4.3   Machine Learning Methods

The third set of tests for lake melt sources classification employs machine learning methods, computed using the MATLAB® Machine Learning Classifier (MLC) application (MATLAB 2020). The classifier takes a set of identified multivariate data points (also referred to as training data) and applies multiple machine learning algorithms on the data variables in order to create a prediction function that can identify unidentified data points from their input variables. All tests were performed using 10% cross-validation to reduce the likelihood of overfitting. Tests were performed with and without PCA precondition-

ing, but found that it did not make a significant difference in accuracy and, therefore, was not included in the preferred classifier. The resulting prediction function uses the training data to test its accuracy by the number of correct classifications it makes. Unlike the previous two methods, MLC has multiple methods at its disposal, which we use to find methods that accurately identify environments with lake melt sources probabilities.

A null lake class (i.e., no lake present) is required to train the machine learning classifier to identify regions without lakes. Although we have a database of lake locations, there is no validated null lake dataset (i.e., locations without lakes). Therefore, we randomly assign several Antarctic locations as proxies for a null class (i.e., no lake present) with the only restriction being a minimum proximity to currently known lake locations. While randomly picking points can be a tenuous method for creating a null class—an undiscovered lake can be incorrectly assigned a null class—staying far away from known existing lakes is a simple and independent criterion that seems logically reasonable. Several tests were conducted by varying the minimum allowable distance from null points to known lakes. An optimal threshold of 200 km was determined for the null proxy cells (Supplementary Methods). To prevent oversampling, 675 null proxy cells—same as the number of subglacial lakes—are used for training.

We initially begin by testing the training data against all 25 of the available classifiers using default settings to identify the most promising methods from their accuracy (see attached supplementary table). The best performing methods were explored more thoroughly, testing a range of tuning parameters (see supplementary material). The subspace KNN method was found to deliver the highest percentage of correct classifications, and therefore, used create our preferred classifier model. The subspace KNN model is an ensemble learner where KNN classifications are made using multiple subsets of the environmental properties. The classification is predicted via the majority response from the ensemble of predictions. To access the probability score for each class, we reverted to the command-line versions of the classification codes.

6.5   Results

6.5.1   Comparative Analysis

Surface temperature is one of the most distinct parameters when comparing lakes with Antarctica as a whole (Figure 6.3). The estimated annual average surface temperatures for Antarctica range from -55 to -10 °C with a relatively uniform distribution (Figure 6.3A). Stable lakes are more common in regions with low surface temperatures, generally <-40 °C whereas active lakes are more common at warmer temperatures. The KS statistic for stable lakes is 0.49 and for active lakes it is 0.163, indicating a greater difference between stable lakes and Antarctica than between active lakes and Antarctica.
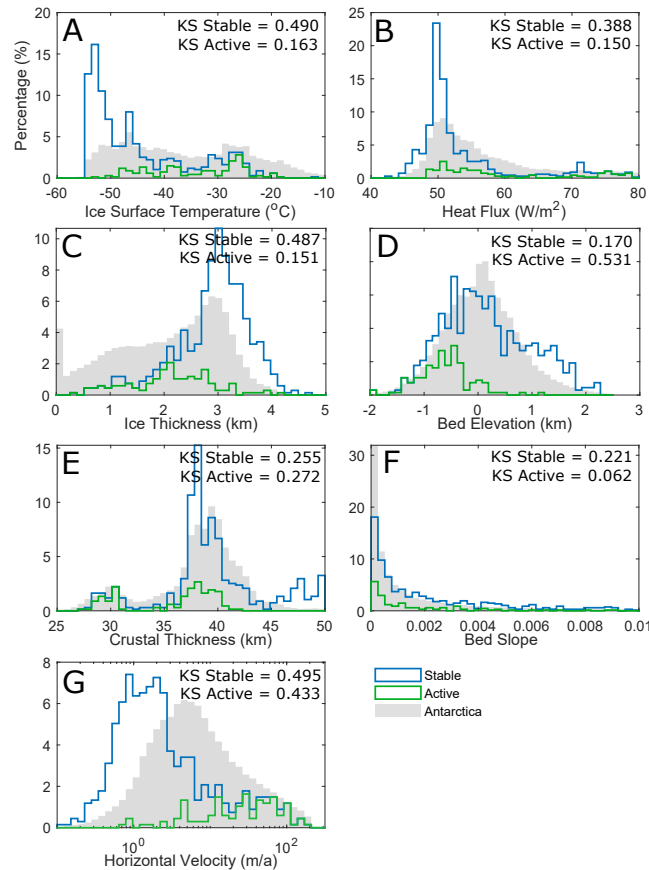
Figure 6.3: Comparison of Antarctic and lake distribution for key environmental parameters. Antarctica datasets have been resampled to a common 10 km × 10 km grid. The Antarctic datasets have been normalized to a percentage of the entire continent, lakes have been normalized to the total number of lakes (both active and stable). The Kolmogorov–Smirnov (KS) statistics are computed between the cumulative distributions of lakes distinguished by type and the Antarctic continent. Larger KS values indicate a greater difference between the distributions.

Both Antarctica and subglacial lakes skew toward lower basal heat flux values, with both peaking around 50 mW m^{-2}(Figure 6.3B). Although Antarctica has a long, smooth tail for high estimated heat flux values, stable lakes noticeably drop above 57.5 mW m^{-2}. The one exception is a small cluster of lakes around 75 mW m^{-2}. These high heat flux related lakes are in regions of West Antarctic (Figure 6.1) that experience Cenozoic rifting (Schroeder et al. 2014).

A large difference between Antarctic and stable lake distributions is found with ice thickness (Figure 6.3C). Antarctica ice thickness values are relatively uniformly distributed, ranging from 0 to 4 km. However, lakes rarely occur beneath ice thinner than 1 km, and stable lakes generally skew strongly towards regions with thick ice (>2.8 km). The peak in the lake distribution occurs slightly higher than 3 km of ice, resulting in a KS statistic of 0.487 relative to the Antarctic continent. Active lakes are found beneath a wider range of ice thickness values, from less than 500 m to nearly 4 km. This distribution more closely reflects that of greater Antarctica with a KS statistic of 0.151.

The elevation of the Antarctic bed generates a relatively smooth normal distribution ranging from -2 to 2 km (Figure 6.3D). In general, lakes are biased towards lower elevation regions. Although stable lakes have a similar distribution to Antarctica as a whole, active lakes are biased towards lower values. The skew toward lower values is relatively minor for stable lakes, resulting in a KS statistic of 0.17. In contrast, active lakes are strongly skewed toward lower elevations, resulting in a high KS statistic of 0.531.

The bimodal crustal thickness distribution of Antarctica is reflected in active but not stable subglacial lakes (Figure 6.3E). Active lakes exhibit the same bimodal nature as they are found in both East and West Antarctica whereas the vast majority of stable lakes are found in regions with the thickest crust (i.e., East Antarctica, >37 km). This result is unsurprising given the geographic distribution of the identified lakes (Figure 6.1) and the well-known East-West dichotomy of the continent (Baranov et al. 2017, e.g.,). Despite the lack of stable lakes above thin crust in East Antarctica, the KS values are fairly similar for both types of subglacial lakes because the thin crust includes a relatively small area of Antarctica.

Bedrock slope is the least dissimilar environmental parameter between greater Antarctica and its lakes. Both lakes and Antarctica as a whole skew toward topographically flat (Figure 6.3F). Out of the seven parameters, bedrock slope has the least distinct differences between active and stable lakes. Bedrock slope is a poor factor to determine the ideal lake environment, which is consistent with Willcocks et al. (2021) who shows how the topographic effect of local heat flux is likely the opposite of that theorised by van der Veen et al. (2007).

The surface ice velocity of the Antarctic Ice Sheet peaks at 1 - 4 m a^{-1} (Figure 6.3G). Neither active nor stable lakes distributions are similar to that of Antarctica. In a clear difference between stable and active lakes, stable lakes are skewed towards regions with slow moving ice whereas active lakes are skewed towards regions of fast moving ice. The regions of slow velocities have high vertical advection which depresses the thermal gradient, carrying colder temperatures down to the base of the ice sheet (Mony et al. 2020). Thus stable lakes can only form under regions of sufficiently thick ice where temperatures can reach the melting point along these depressed thermal gradients. Active lakes, however, tend to form in regions where the ice is flowing rapidly showing that they are not the product of the geothermal gradient. The KS-statistic is relatively high for both types of lakes, 0.495 for stable lakes and 0.433 for active lakes.

6.5.2 Principal Component Analysis

The PCA analysis indicates a relatively similar variance between five of the seven normalised and centred variables (Table 6.1). Horizontal velocity accounts for the largest variance ($\sim$29%) whereas bedrock slope accounts for 2% of the total. Because the variance contributed by bedrock slope is very small, we exclude it from the remainder of the PCA analyses. Excluding bedrock slope results in relatively minor changes to the basis functions and does not affect interpretations based on the results.

The first three principal components account for >90% of the total variance (Table 6.2). The first principal component explains nearly 63% of the variance in the data. The analysis identifies crustal thickness and bed elevation as the most important variables,

Table 6.1: Variance of environmental parameters associated with Antarctic subglacial lakes as well as the percentage of the total share of the variance. Most variance is found in the velocity whose variance makes up over a 1/4 of the total variance. Bedrock slope makes up the least with less than 1.5% of the total variance. Note: We have taken the log of velocity to account for the orders of magnitude difference between the maximum and minimum values.

	Variance	Total %
surface temperature	0.711	10.912
basal heat flux	0.825	12.660
ice thickness	0.508	7.801
bed elevation	1.369	21.013
crustal thickness	1.868	28.667
bedrock slope	0.097	1.495
horizontal velocity (log)	1.137	17.451

contributing to a positive score. On the negative side, horizontal velocity, surface temperature and heat flux are important. For the second principal component, ice thickness contributes to a negative score whereas all other variables trend towards positive values.

Table 6.2: Basis vectors determined by the PCA analysis of subglacial lakes and their explained variance. We can see that almost 63% of variance is held within the first principal component and over 93% of the variance is contained within the first three principal components.

	PC1	PC2	PC3	PC4	PC5	PC6
surface temperature	-0.315	0.338	-0.163	0.157	-0.152	0.844
basal heat flux	-0.266	0.434	-0.423	0.594	0.086	-0.450
ice thickness	0.129	-0.450	0.109	0.567	0.619	0.255
bed elevation	0.500	0.451	-0.333	-0.344	0.554	0.105
crustal thickness	0.637	0.345	0.421	0.415	-0.352	0.040
horizontal velocity (log)	-0.397	0.416	0.703	-0.106	0.395	-0.089
% variance	66.136	16.506	10.774	3.44	2.272	0.872

For the first two principal components, the projection of the basis vectors is quite simple, which makes it relatively straightforward to interpret the variance of scores. The basis vectors fall into three groups: (1) bed elevation and crustal thickness; (2) surface temperature, geothermal heat flux, and horizontal velocity; and (3) ice thickness. An increase in group 1 vectors increases PC1 and PC2 scores. An increase in group 2 vectors increases PC1 and decreases PC2. An increase in group 3 vectors has little influence on PC1 while strongly contributing to negative PC2 scores (Figure 6.4).

Unfortunately, the similarity between the distributions of the lake scores and the
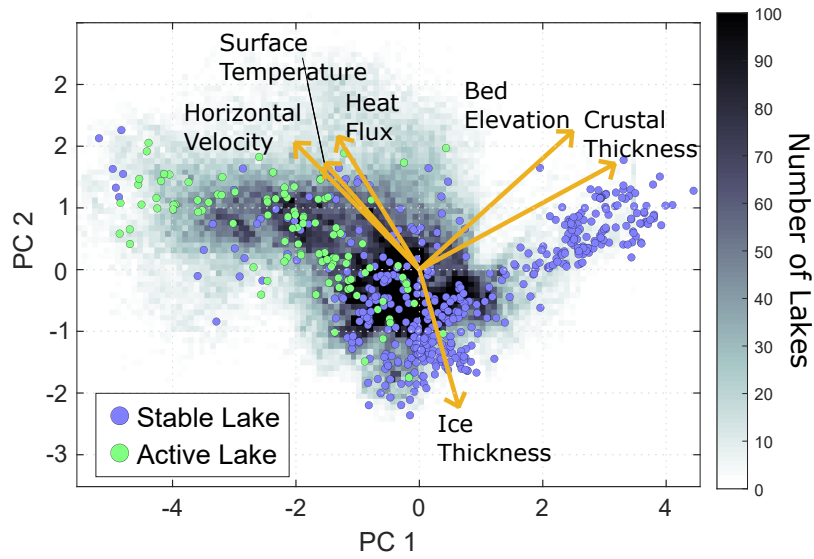
Figure 6.4: Map of lake scores in the first two principal axis overlying a heat map of the scores of a 10 km × 10 km terrestrial Antarctic grid. Scores are computed from the sum the of products of the centred and normalized environmental parameters with their associated principal vector components. Also shown are the projections of the environmental vector components illustrating the relative importance of each parameter on a locations score.

Antarctic grid prevents accurately predicting a lake melt source from the PCA results (Figure 6.4). However, it is possible to discriminate between stable and active lakes and the regions they are most likely to be found from the PCA score. Stable lakes tend to have positive PC1 scores and/or negative PC2 scores whereas active lakes tend to have negative PC1 scores and less negative PC2 scores. Stable lakes tend to follow the group 1 and 3 axes whereas active lakes tend to project along the group 2 axes. While there are several stable lakes with negative PC1 (generally PC1 < -1), only two active lakes have a positive PC1 score. The stable versus active lake tendencies towards positive and negative PC1 scores, respectively, provide a means to classify regions as favourable to either type of lake.

A map of PC1 scores illustrates the correspondence between PC1 scores and sub-glacial lake locations (Figure 6.5). PC1 scores are generally positive in East Antarctica except along the coast and within ice streams. PC1 scores are generally negative in West Antarctica and along the coast. This result is reflective of the general East–West dichotomy within Antarctica; thick crust and higher bed elevation in the east and higher heat flux and surface temperatures in the west. The PC1 map shows a nice correspon-

dence to the locations of lakes, even resolving the difference in classes at reasonably fine resolution in some regions (e.g., Coats Land).
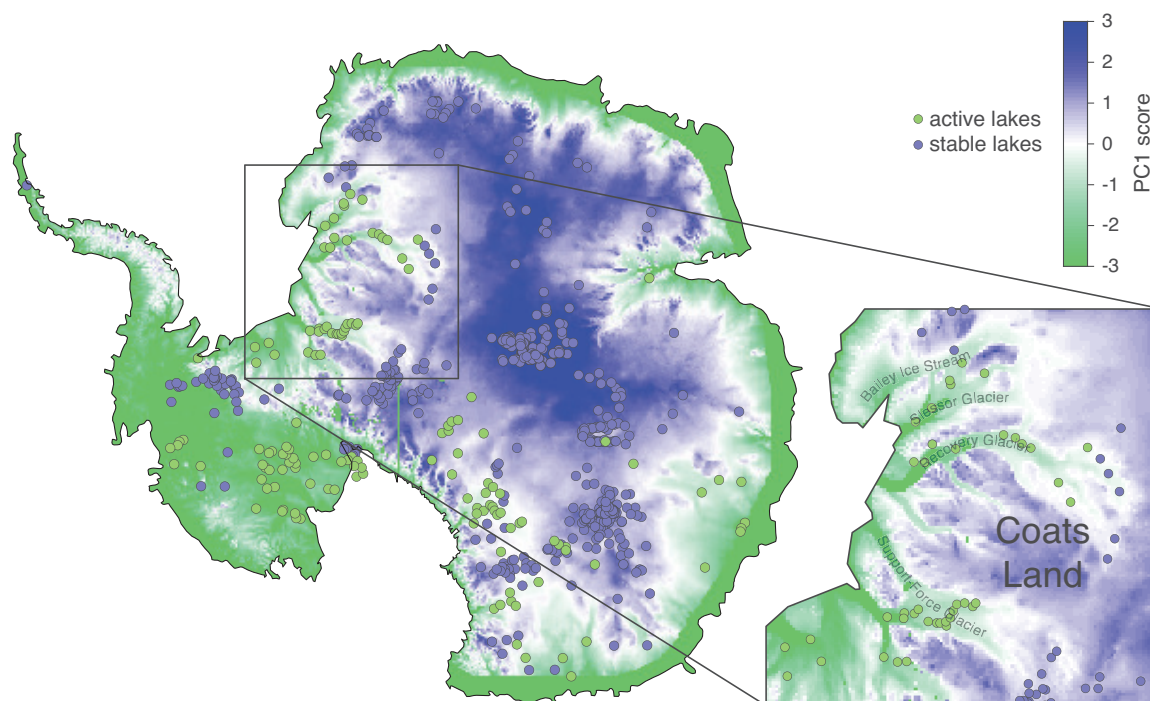
Figure 6.5: The scores of each Antarctic cell along the first principal axis thus showing where active lakes are likely to form (green areas) over stable ones (blue areas). A larger scale view of PCA1 illustrates the accuracy of predicted lake types of the region in the black box shown in along with ice stream names.

6.5.3 Subspace KNN Classifier

Our preferred Subspace KNN classifier uses 7 learners with 4 dimensions to generate the prediction function. The preferred model was determined by training classifiers to a range of learners and dimensions (Supplementary Methods). The ideal model parameters were chosen by a kink in the L-curve of the classification error rate. Model performance relative to each class was evaluated using multiple metrics computed from the confusion matrix (Table 6.3). Across the three classes, the subspace KNN model resulted in precision >73% with the highest, 92% for stable lakes. Sensitivity is another metric of accuracy. Around 90% of stable lakes and null cells where correctly identified by the Subspace KNN model. However, only 58% of active lakes were correctly identified by the model. Most incorrectly identified true lakes were misclassified as null. However, many of the misclassified lakes

lie just outside of regions classified with high lake probabilities (Figure 6.6). Perhaps the relatively low grid resolution of the environmental parameters plays some role in the accuracy.

Table 6.3: Performance of the preferred classifier (7 learners, 4 dimensions). The confusion matrix reports the true and predicted class following model training. Also shown are the percentages correct/total and incorrect/total in each respective row and column.

| | | Predicted Class | | | | |
		stable	active	null	sensitivity	miss rate
	stable	456	12	68	85.1 %	14.9 %
True Class	active	18	80	41	57.6 %	42.4 %
	null	22	17	631	94.2 %	5.8 %
	precision	91.9 %	73.4 %	85.3 %		
	false discovery rate	8.1 %	26.6 %	14.7 %		

Visually, the map of predicted lake class map shows good spatial correspondence between lakes and the class probability (Figure 6.6). The machine learning model identifies the regions running from Dome C across central East Antarctica, the around the South Pole, and the Pine Island Glacier as high probabilities for stable lakes. High probabilities of active lakes are found in Marie Byrd Land, west of the Transantarctic Mountains and south of Mount Erebus, and ice streams in Coats Land. Because of our color scale, only null regions with very high probability null class (>90%) are clearly null (white). These regions tend to be relatively large and continuous and far from lakes. However, there are many regions with more moderate probabilities of a null class that also exist, which must contain misclassified lakes. We chose a simple majority to determine a locations class, however, raising the threshold for null determination would reduce the number of lakes classified as null.

6.6   Discussion

We find that multivariate methods provide valuable insight into the types of environments associated with source regions for subglacial lakes. While a comparative analysis is able to show unique trends in the distribution of lake properties compared to the Antarctic background it can only be used in a qualitative way. Thus to develop any reasonable
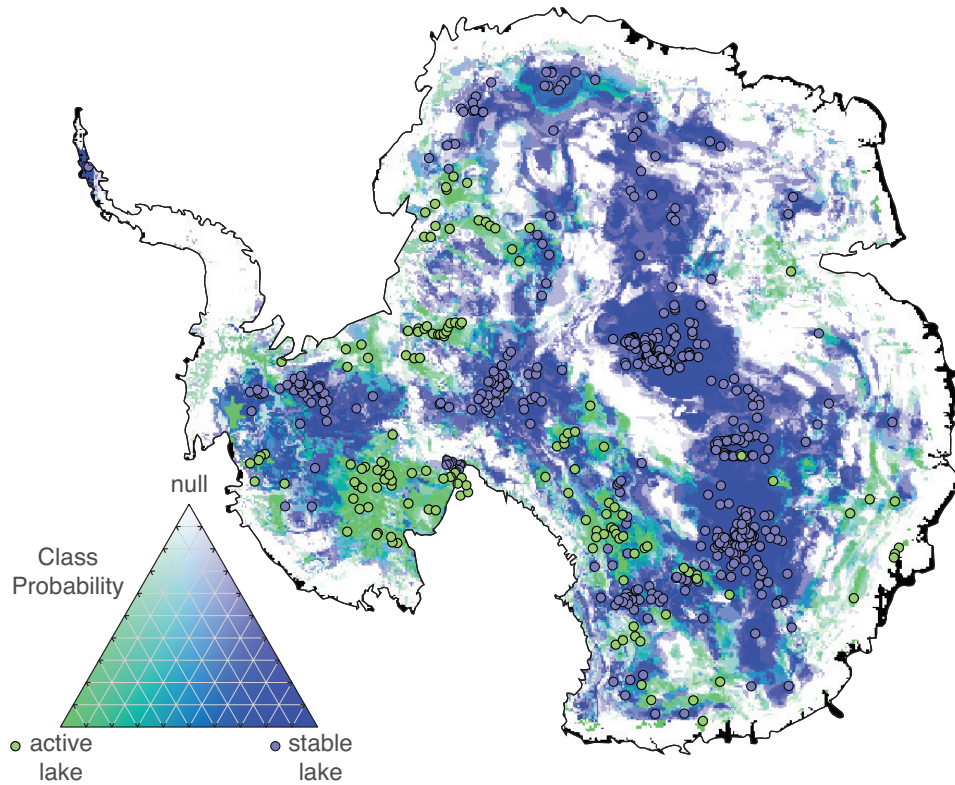
Figure 6.6: Location of stable (blue) and active (green) lake melt sources classified by a Machine Learning Classifier as having a high or low probability based of the six parameters identified in this paper. The classifier was created using a training data set of 140 active and 535 stable Antarctic sub-glacial lakes parameters combined with 675 Antarctic null cell parameters. Null cells where identified based off being over 200km away form any currently observed lake.

map of subglacial melt sources and the types of lakes they fill, multivariate methods are required.

The comparative analysis is able to identify biases in the types of environments conducive to lake formation (Figure 6.3). Only horizontal velocity shows clear differences between both lake types and Antarctica, though in opposite ways. Stable lakes tend to be found in regions of low velocity whereas active lakes are more common in regions of fast moving ice. MacKie et al. (2020) also identified a similar distinction in horizontal velocity correlation coefficients between the two types of lakes. Stable lakes tend to reside in regions with ice thicker than 2500 m (not the 3500 m identified Pattyn et al. (2016)), low surface temperature and low heat flow. It is likely that the low heat flow influences the thick ice. This combination of properties is consistent with the geographic location of the most stable lakes in the interior of East Antarctica. In contrast, active lakes are

found regions with low bed elevation and high velocities, which are more commonly found in West Antarctica and along coastal ice streams. Bell et al. (2007) had previously made similar observations about active lakes found in ice streams. The lack of a clear difference in heat flux, surface temperature, and ice thickness suggests that active lakes may not have strongly thermal origins. Instead, active lakes form by melting elsewhere which is subsequently transported to the lake locations. The low accuracy of the KNN method for active lakes is probably related to our choice of environmental datasets that reflect the thermal conditions of the ice sheet. A different set of datasets may be required to improve the performance of machine learning methods when looking for active lakes.

PCA provides a means to quantitatively map the multivariate distribution of properties that contribute to stable and active lakes (Figure 6.5). The first principal component is the most significant for identifying lake types. In regions where both active and stable lakes are in close proximity the result is remarkably accurate as demonstrated for Coats Land (Figure 6.5 inset). Although regions with high second principal component scores (>1.8) are generally regions without lakes, most of the null randomised cells show little difference in distribution to lakes (Supplementary Figure 2B). These regions correspond to the Antarctic Peninsula and the Transantarctic Mountains. Hence PCA may poorly identify regions where melt is unlikely.

Machine learning can refine the prediction of lake types and melt source regions and provides the means to assess the confidence in such predictions. For example, the Subspace KNN classifier is able to rectify regions where PCA poorly classifies stable lakes in West Antarctica (Figure 6.6). By adding null locations, it identifies regions where melting is unlikely. Because the null cells are random and only based on a minimum proximity to known lakes, there is the potential that some of the null cells could still be regions of melting. However, the distribution of null regions is considerably greater than the area where the randomized null points are located, many with no null training points (Figure 6.6 and Supplementary Figure 2A).

Like MacKie et al. (2020), we find that the bedrock slope adds very little useful information to identify lakes and potential melt sources. While other environmental

properties have clear biases in lake distributions, bed slope does not (Figure 6.3G). We initially ran machine learning models with bed slope, but found that it did not produce significant improvements in the classification models. Therefore, we excluded bed slope from our preferred models. Previous studies include hydraulic potential (Livingstone et al. 2013, Goeller et al. 2016, MacKie et al. 2020), which may improve precise prediction of lakes rather than melt regions. However, the large error in bed elevation (up to ±1000 km in some locations) Morlighem et al. (2019) can undermine the utility of bed slope for predictions. Additionally MacKie et al. (2020) found very low correlation between bed slope and lake probability predictions further suggesting its limited contribution. It is more likely that the addition of distance along flow paths and a water routing algorithm results in the differences in probability between MacKie et al.'s model and our own.

The probabilities predicted for lake locations by MacKie et al. (2020) are generally much lower than ours. Again, this difference is likely due to the addition of water routing model and an attempt to precisely locate lakes rather than identify potential source regions. However, there are some key differences that arise from other choices. Our model predicts a gap in central East Antarctica that is devoid of lakes (Figure 6.6) whereas MacKie et al. (2020) predict no such gap, probably due to our method for introducing null cells. It remains to be seen whether our method is valid. Another clear difference between our model and MacKie et al. (2020) is situated beneath the Pine Island Glacier in West Antarctica, where there are several stable lakes (Figure 6.6). These lakes were included in the lake database at the time MacKie et al. (2020) trained their model. While they do show a very slight probabilities (<0.001) beneath this region, our model suggests a much higher likelihood.

There have been a number of new heat flux models of the Antarctic continent in the past few years. Current models can have a wide variety of values for the basal geothermal heat flux of Antarctica (Shen et al. 2020). MacKie et al. (2020) included a global seismic tomography based heat flux model by Shapiro (2004) and two magnetic Curie depth derived heat flux models (Maule 2005, Martos et al. 2017). The global tomography model is too low resolution to be very useful so it is excluded from our study. We include several

more recent heat flux models in our analysis in addition to the two magnetic-based models, including the continent-wide seismic tomography-based model by An et al. (2015), two statistical-based models by Shen et al. (2020) and Stål et al. (2021), and a thermal-based model by Guimarães et al. (2020).

Our preferred model uses the ensemble heat flux model, however, we produced a Subspace KNN map for each heat flux model separately. We find that the ensemble model gives results with the highest accuracy, though admittedly the variations in accuracy range from 86 to 91% (Supplementary Figure 3D). Because an ensemble model averages out differences and amplifies agreement between models, it will often produce a better estimate of the true field. Hence, the best result is obtained using the ensemble heat flux.

When compared individually, the recent statistical-based models—which we believe are presently the most accurate estimates of heat flux—do not perform as well as the magnetic based models. We hesitate to speculate why this may be so because there are clear issues with the magnetic models. For example, heat flux in some large regions of west Antarctica is estimated to be >150 mW m^{-2} (Maule 2005, Martos et al. 2017), whereas heat flux higher than 120 mW m^{-2} would cause regional melting of the middle to lower crust (Hasterok & Chapman 2011). Furthermore, the Curie depth models are highly sensitive to the initial depth estimates (Hasterok et al. 2021). In order to produce the predicted low heat flux in cratonic East Antarctica and higher heat flow in the Cretaceous West Antarctica Rift, the crustal thickness in West Antarctica was arbitrarily halved to produce the initial Curie depth (Maule 2005, Martos et al. 2017). Thus the Curie depth based heat flux estimates may have biases introduced that make them less accurate. However, none of the heat flux models perform well when compared with conjugate terranes in Australia, India and Africa (Pollett et al. 2019).

Regardless of the heat flux model used to train the lake classifier, the results are generally similar (Supplementary Figure 4). The largest differences occur in West Antarctica, though even there, the models share broad agreement of no lakes on the Antarctic Peninsula, stable lakes in the vicinity of the Pine Island Glacier and active lakes in Marie Byrd Land. Another region of some difference appears beneath Victoria Land to the west of

the Transantarctic Mountains.

Given the large variations in heat flux models, there is likely still some significant improvement that can be made in the future. Some of the discrepancies between heat flux models result from differences in sensitivity of the geophysical fields to temperature as opposed to other factors like composition. However, a significant fraction of the differences are probably due to uncertainties in physical properties of the crust that are poorly constrained (Pollett et al. 2019). Physical property uncertainties also affect statistically based methods since they tend to resort to average behaviour rather than accurately capturing the range and wavelength of spatial variations (Shen et al. 2020). Therefore, improving heat flux models requires better estimates of heat production and thermal conductivity variations both laterally and vertically within the crust. It may be possible to improve physical property estimates using empirical relationships between thermal properties and geophysical proxies such as crustal seismic velocity or density (Hasterok & Webb 2017, Hasterok et al. 2018, S. Jennings 2019). Near surface variations in thermal conductivity can also cause refractive effects that are not incorporated into geophysical proxy-based heat flux estimates (Willcocks et al. 2021). Incorporating these estimates will require models of subglacial geology, specifically the location of geologic contacts which could be developed from a combination of gravity and aeromagnetic observations.

6.7   Conclusion

Multivariate methods have the potential to improve our understanding of subglacial lake distributions and their source regions. Using a combination of comparative analysis, principal component analysis, and machine learning classification, we find that stable lakes are more likely in regions with thick ice, and low geothermal heat flux and active lakes lie in regions with fast ice concentrated in coastal ice streams and West Antarctica. Principal component analysis is able to distinguish between the environments that typically form active lakes compared to stable lakes, but cannot identify regions unlikely to contain lakes. Machine learning methods can improve the prediction of lake types, as well as identify regions without lakes. The Subspace KNN method was found to be the most accurate

machine learning method. Producing more accurate maps that identify ideal subglacial lake melt sources requires improved resolution of environmental characteristics. Such maps will also benefit from improved heat flux estimates that incorporate subice geology to predict thermal properties.

Chapter 7

Conclusion and Future Directions

Demand for better understandings of the Antarctic thermal regime has become a necessity to improve models of ice sheet dynamics in response to climate change. The geothermal heat flux transferred from the soild Earth to the ice sheet is of keen interest because it provides a basal boundary condition for the thermal state of the ice, influencing the rheology, flow velocities, and melt potential. Throughout this thesis I have improve our understanding of the Antarctic thermal state by developing independent constraints on geothermal heat flux derived from subglacial lakes and producing a model of the thermal conductivity of the Antarctic lithosphere.

The importance of knowing the thermal conductivity make up of the underlying Antarctic bedrock cannot be understated. Chapter 3 shows the flow of heat is intrinsically linked to the thermal conductivity differences between the Antarctic ice sheet and the underlying bedrock. Heat will intrinsically seek the path of least thermal resistance on the way to the surface resulting in localized region of elevated basal heat flux around topographic peaks and especially geological contacts. Thermal refraction can adjust the temperature within an ice sheet by as much as 2.5 °C which can result melting in places previously not assumed. These effects can be scaled up to continental sizes as heat naturally seeks the path of least resistance from the mantle to the surface.

Since the thermal conductivity make up of the underlying Antarctic bedrock has a major effect on the flow of heat proxy-based models of GHF cannot assume a constant conductivity continent wide. I collected the thermal conductivity and density of 49 sam-

ples from Antarctic outcrops and I found no discernible differences between these samples and the global thermal conductivity database. As there is no difference, the supplemented global dataset is used to produce a relationship between thermal conductivity and seismic velocity. This has allowed me to estimate the thermal conductivity of the Antarctic continental crust to a depth of 35 km. This model highlights a highly thermally conductivity region under the south pole that, as shown in Chapter 3 could allude to heightened basal heat flux. Although this model is not high enough resolution to accurately model small-scale refractive effects, this study provides a way to predict conductivity once higher resolution seismic models exist.

A similar heightened basal heat flux is also alluded to when I compare current proxy models of Antarctic basal heat flux against the basal heat flux constraint (BHFC). Since all of the 6 proxy models tested fell well below the BHFC it indicates none of the models can generate the number of observed subglaical lakes. This high heat flux anomaly is most noticeable at the lakes located beneath the South Pole which is constant with the findings in Chapter 4 showing a potential elevated heat flux as the result of a thermally conductive crust. Such a feature does not show up in many current proxy basal heat flux which may be a result of their use of uniform parameters including thermal conductivity.

To demonstrate the importance of basal heat flux models I combine them with other Antarctic environmental properties develop predictive models of subglaical melts. While a simple analysis of site characteristics indicates surface temperature, ice thickness and ice velocity are key variables associated with melting results from PCA indicate that bed elevation, crustal thickness and basal heat flux are also important. While PCA is only able to distinguish regions in Antarctica based on lake type rather than lake probability,the probabilities for each type of lake (or no lake at all) can be predicted using machine learning. I use a subspace KNN classifier to accurately classify the location and probability of stable and active lakes across Antarctica.

To accurately model the thermodynamic state of the ice sheet major improvements will be required in mapping the Antarctic geothermal heat flux. Geothermal heat flux is a critical a component in the creation of subglacial lake melt sources (chapter 6) as the

addition of more modern models saw a noticeable increase in the accuracy of predictive maps. Improvements in mapping the Antarctic geothermal heat flux will require a better understanding of the bedrock thermal conductivity (chapter 3). We can interpolate the surface Antarctic bedrock thermal conductivity by measuring the oxide composition of bedrock samples distributed across the continent and using equation 4.6 to assign a thermal conductivity. We can also turn seismic velocity models of the Antarctic region into maps of thermal conductivity (chapter 4) although this will require expansion of seismic measurement into large regions of East Antarctica. Using the mapped bedrock thermal conductivity to create a Antarctic geothermal heat flux model one can also test accuracy using the methods laid out in chapter 5.

Future studies may build upon the methods and results developed in this thesis to further improve dynamic models of the Antarctic Ice Sheet. Future studies should employ a content-wide model of Antarctic crustal thermal conductivity based on a much larger array of samples including a greater geographic sampling and a larger number of mafic lithologies that are currently under-represented relative to felsic compositions. Additionally, the conductivity dataset should incorporate temperature effects on conductivity to improve the accuracy of predictive relationships for the deep crust. Models for the geothermal heat flux can also be further improved by refining constraints provided by subglacial lakes. For example, adding more properties or detailed observation at subglacial lakes that address non-thermal effects that contrute to melting may improve the subspace KNN-classifier accuracy with respect to lake melt sources.

Appendix A

Supplementary material for Chapter 3: Thermal refraction: implications for subglacial heat flux

To compute the conductivity depth relationships shown in Figure 3.3a we use the equation from (Paterson 1994),

$$k(\text{W m}^{-1}\text{ K}^{-1}) = \frac{2k_i\rho}{3\rho_i - \rho}, \tag{A.1}$$

where k_i is the conductivity of pure ice, ρ_i is the density of pure ice, and ρ is the observed density of ice at depth. The thermal conductivity of pure ice can be estimated using the relation by Paterson (1994),

$$k_i(T) = 2.072exp(-5.7 \times 10^{-3}\,T), \tag{A.2}$$

where T is temperature in degrees Celsius. The density of pure ice is given by

$$\rho_i(\text{kg m}^{-3}) = 916exp(-\alpha_V T), \tag{A.3}$$

where α_V is the thermal expansivity of ice, 112×10^{-6} K^{-1}. The temperature can be determined from ice cores. For Figure 3.3a we use the South Pole temperature profile as

reported by Price et al. (2002),

$$T(^\circ\text{C}) = 1.83415 \times 10^9 z^3 - 1.59061 \times 10^8 z^2 + 0.00267687z - 51, \qquad \text{(A.4)}$$

where z is given in meters. The observed density of ice has been determined on a separate core by Kuivinen & Koci (1982),

$$\rho(\text{kg m}^{-3}) = 374.15 + 562.285(1 - exp(-0.01535z)), \qquad \text{(A.5)}$$

with z in meters.

Appendix B

Supplementary material for Chapter 5: Melt constraints on the geothermal heat flux beneath the Antarctic Ice Sheet

B.1 Creating Ice Geothermal Profiles

This supplement details our method for calculating geothermal profiles through the Antarctic ice sheet to estimate a basal heat flux constraint. To compute the basal heat flux constraint, we first solve for temperature using the heat equation governing a moving ice sheet (Llubes et al. 2006),

$$\kappa \frac{dT^2}{dz^2} - u\frac{dT}{dx} - w\frac{dT}{dz} + \frac{\tau_b \frac{du}{dz} z}{c_p \rho H} = 0, \tag{B.1}$$

for temperature, where u and w are the horizontal and w is the vertical velocities, respectively. The thickness of the ice is given as H, basal shear stress by τ_b, and κ, c_p and ρ are the physical properties of the ice. We use a finite difference formulation, solving the

above PDE in one-dimension,

$$T_i = \frac{T_{i+1} + T_{i-1}}{2} + \frac{\Delta z^2}{2\kappa_i}\left(\frac{-\frac{\Delta V}{\Delta z}_i \tau \; z_i}{c_{p,i}\rho_i h} - w_i \frac{T_{i+1} - T_{i-1}}{\Delta z}\right) \qquad \text{(B.2)}$$

where i represents one of 50 discrete points along a profile from $z = [0, H]$ (surface to base of the ice sheet). As many of the of the physical properties are temperature dependent, the solution must be determined iteratively until the solution is stable. From this temperature profile, basal heat flux (Q_b) can easy be calculated from Fourier's Law applied at the base of the ice sheet (equation 1 of the main text). If no stable solution is obtained, we set the cell as not-a-number (NaN).

B.1.1   Physical properties

A number of physical properties are required to estimate the thermal profile. We use the following temperature-dependent relationships to estimate the thermal properties of the ice (Paterson 1994),

$$\text{thermal diffusivity,} \qquad\qquad \kappa(T) = \frac{k(T)}{\rho(T) \; c_p(T)}; \qquad \text{(B.3)}$$

$$\text{density,} \qquad\qquad \rho(T) = 916 \; e^{-112.5 \times 10^{-6}T}; \qquad \text{(B.4)}$$

$$\text{thermal conductivity,} \qquad\qquad k(T) = 2.072 \; e^{-5.7 \times 10^{-3}T}; \qquad \text{(B.5)}$$

$$\text{specific heat capacity,} \qquad\qquad c_p(T) = 2.1275 \times 10^3 + 7.253 \; T. \qquad \text{(B.6)}$$

B.1.2   Vertical Velocity

Since measuring vertical velocity at the surface is difficult, we use the principle of mass balance (Paterson 1994),

$$\frac{\partial v}{\partial x} + \frac{\partial u}{\partial y} + \frac{\partial w}{\partial z} = 0 \qquad\qquad \text{(B.7)}$$

where v, u and w are the ice velocity in the x,y and z directions, respectively. Next, we determine that the vertical velocity by,

$$w(z) = w_b + \int_H^z \frac{dv}{dx} + \frac{du}{dy} \ dz, \tag{B.8}$$

where H is the ice thickness and w_b is the vertical velocity at the base of the ice sheet (which we will assume is 0 since ice does not flow into the bedrock). Thus, the surface velocity is be equivalent to

$$w_s = \int_H^0 \frac{dv}{dx} + \frac{du}{dy} \ dz. \tag{B.9}$$

Since it is not possible to measure the velocity through the entire ice sheet remotely, we use the surface velocity to estimate the velocity though the entire ice sheet. The absolute horizontal velocity ($V_s = \sqrt{u_s^2 + v_s^2}$) within the ice sheet can be estimated by the relation (Paterson 1994),

$$V(z) = V_s \left(1 - \left(\frac{z}{H} \right)^{n+1} \right), \tag{B.10}$$

where n represents a variable integer that determines the profile horizontal velocity takes. The n value can vary from region to region, but may be difficult to determine a priori. Therefore, we set this value to 3, which produces vertical temperature profiles in the ice sheet similar to those observed in Antarctica (Figure 4B and C of the main text).

Since vertical velocity is determined based on the change in horizontal velocity, it can be estimated by (Wolff & Doake 1986),

$$w(z) = w_s \frac{\int_H^z f(z)dz}{\int_H^0 f(z)dz} \tag{B.11}$$

where $f(z) = \frac{V(z)}{V_s}$.

B.1.3 Basal Shear

Basal shear stress, τ_b, found via the following equation,

$$\tau_b = \rho_i g H \ \sin(\alpha_s) \tag{B.12}$$

where ρ_i is the density of ice, g is gravity and α_s is the bedrock slope expressed as an angle. We calculate the α_s using Antarctic bedrock topography Fretwell et al. (2013).

B.1.4   Demonstrating horizontal advection is negligible

We assume horizontal advection is negligible in our calculations outlined above. To show that horizontal advection is negligible we compare its base properties of ice velocity and thermal gradient to those of vertical advection. Vertical surface ice velocity is found to be around 0.2 m/annum Rignot (2019) while the vertical ice gradient is around 25° C/km Willcocks et al. (2021). Meanwhile the horizontal surface ice velocity to be around 0.7 m a^{-1} Rignot (2019) while the horizontal ice gradient sits around 0.2 °C lat^{-1} = 0.0016 °C km^{-1} Fortuin & Oerlemans (1990). While horizontal surface ice velocity can be anywhere from 5 to 10 times greater than vertical surface ice velocity, the fact that the vertical gradient is over 6000 times larger than the horizontal gradient results in the horizontal advection term being over 1000 times smaller and thus negligible in the case of our studies.

B.2   Individual Model Plots

Bellow are the 6 individual model plots used in this paper (Maule 2005, An et al. 2015, Martos et al. 2017, Guimarães et al. 2020, Shen et al. 2020, Stål et al. 2021) and their comparison to the ensemble model as well as the basal heat flux constraint (BHFC). We used these plots in the main paper to help visualise geographically how the proxy models individually relate to the BHFC. Also shown is their comparison to the measured drill core site values (Table B.1).
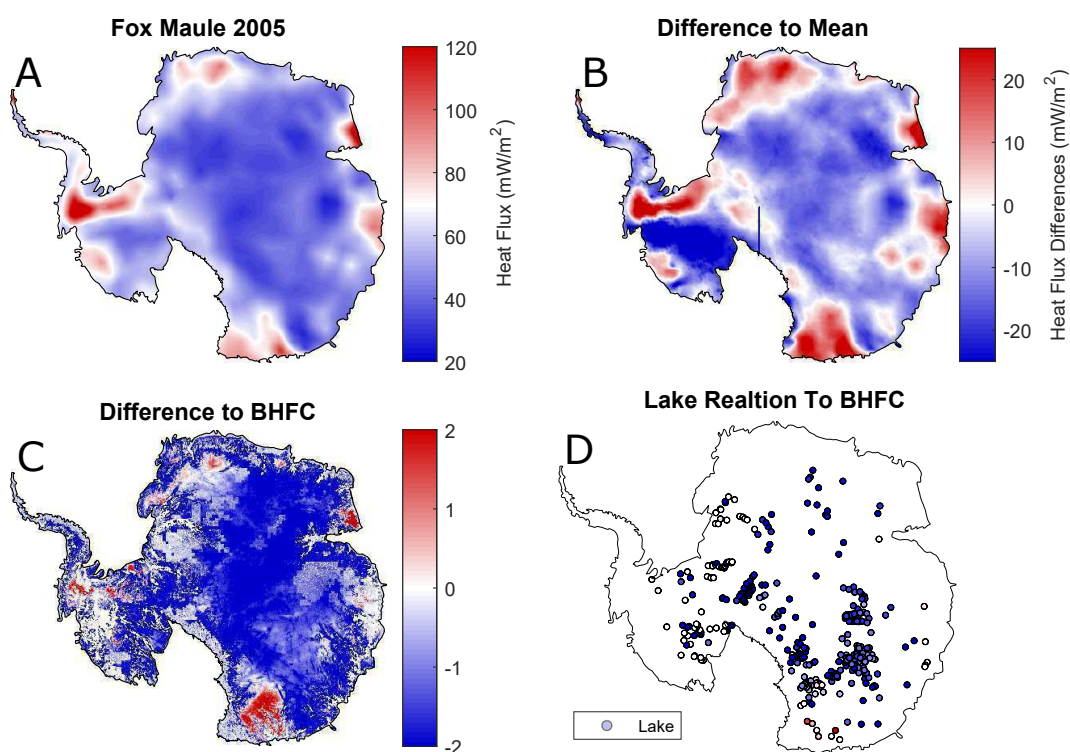
Figure B.1: Evaluation of Maule (2005). A) The original Model, B) The model compared with the mean of the models (main text, figure 1A), C) The model compared with the basal heat flux constraint (main text, figure 3B) and D) A Map of lakes compared with the maximum discrepancy split into the 4 quantiles as explained in section 5.2 in the main text.

Table B.1: The measured geothermal heat flux values in Antarctica (Guimarães et al. 2020) compared to the estimated geothermal heat flux of each tested model in the same region.

Core Site	Lat	Lon	Q site	Maule	An	Martos	Guimarães	Shen	Stål	Mean
DVDP-14/North Fork	-77.54	-161.41	142	58.25	71.14	82.09	129.98	64.30	72.43	79.70
DVDP-12/Lake Leon	-77.63	-162.85	100	60.36	74.84	109.72	140.79	63.80	71.84	86.89
Nagursk-1	-80.78	-47.71	57	35.76	48.08	54.60	51.45	49.30	51.57	48.46
Nagursk-1.2	-88.37	168.62	54	58.90	54.53	55.55	60.28	59.07	63.11	58.57
McMurdo	-77.76	-162.28	115	59.04	72.82	94.47	137.88	63.53	80.26	84.67
Thwaites Glacier WA	-75.5	-106.8	114	41.55	51.60	59.91	49.03	47.20	53.75	50.51
Concordia Subglacial	-74.05	-125.05	100	39.37	45.54	63.34	46.21	47.08	49.81	48.56
Dyer Plateau	-70.5	65	100	64.39	61.48	101.27	77.49	78.12	70.89	75.61
Thwaites Glacier WA	-75.5	-106.8	97	41.55	51.60	59.91	49.03	47.20	53.75	50.51
Lake Vida	-77.82	-161.81	85	58.32	71.69	85.60	134.97	62.82	79.45	82.14
McMurdo Ice Shelf	-77.76	-162.28	82	59.04	72.82	94.47	137.88	63.53	80.26	84.67
Byrd Station	-80.01	119.52	75	42.97	68.08	134.70	54.52	72.20	80.73	75.53
Law Dome	-66.76	-112.8	75	48.86	47.68	63.57	56.07	58.38	65.23	56.63
Siple Dome	-81.65	148.81	69	56.88	64.93	108.80	99.69	67.80	72.64	78.46
EPICA Dome C	-75.1	-123.4	67	41.76	43.50	58.33	51.08	44.88	56.79	49.39
Upper Vincennes	-73.5	-122	65	40.01	49.75	65.45	48.43	42.66	50.95	49.54
South Pole	-90	0	61	52.05	52.81	58.40	55.07	50.36	53.82	53.75
Dome F	-75.1	-39.7	59	41.58	53.55	71.06	59.66	42.22	49.38	52.91
Vostok	-78.45	-106.87	53	38.86	53.79	52.58	48.17	48.11	49.68	48.53
EPICA Dome C 1	-75.1	-23.4	45	51.49	44.63	60.84	56.84	55.68	70.82	56.72
Conc. Trench Dome C	-74.05	-125.05	40	39.37	45.54	63.34	46.21	47.08	49.81	48.56
Dome C area	-75.12	-123.83	40	41.90	40.71	58.07	50.87	45.61	54.05	48.53
Lower Vincennes	-73.5	-122	40	40.01	49.75	65.45	48.43	42.66	50.95	49.54
Vestfold Hills Block	-68.68	-78.25	31	30.56	41.64	40.79	49.87	38.15	38.71	39.95

Figure B.2: Evaluation of Martos et al. (2017). A) The original Model, B) The model compared with the mean of the models (main text, figure 1A), C) The model compared with the basal heat flux constraint (main text, figure 3B) and D) A Map of lakes compared with the maximum discrepancy split into the 4 quantiles as explained in section 5.2 in the main text.
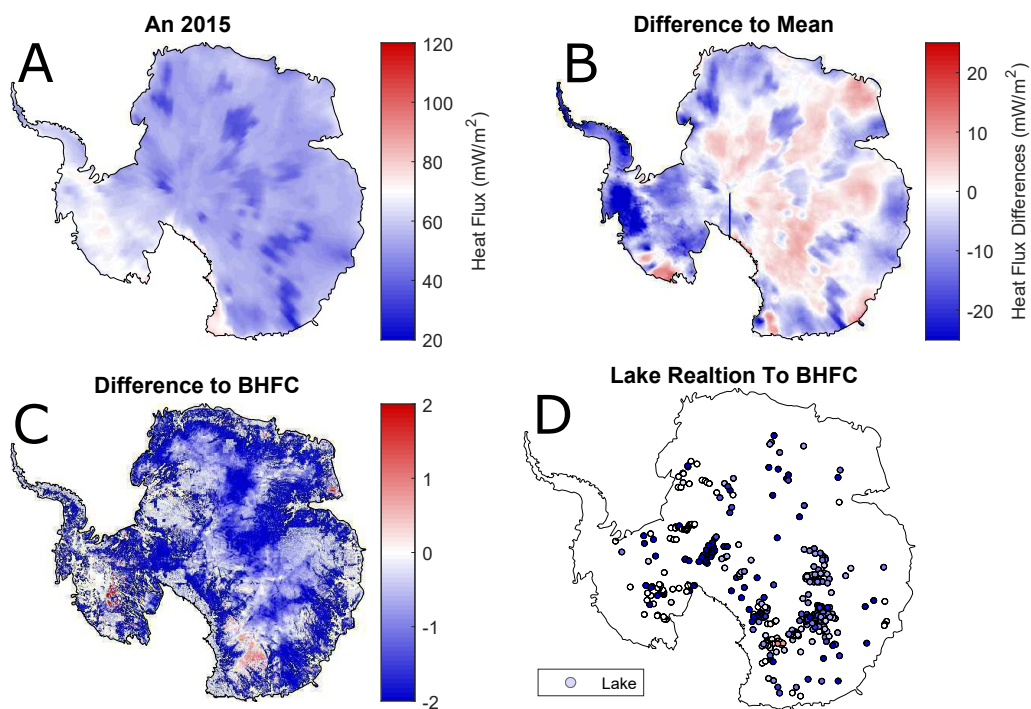
Figure B.3: Evaluation of An et al. (2015). A) The original Model, B) The model compared with the mean of the models (main text, figure 1A), C) The model compared with the basal heat flux constraint (main text, figure 3B) and D) A Map of lakes compared with the maximum discrepancy split into the 4 quantiles as explained in section 5.2 in the main text.
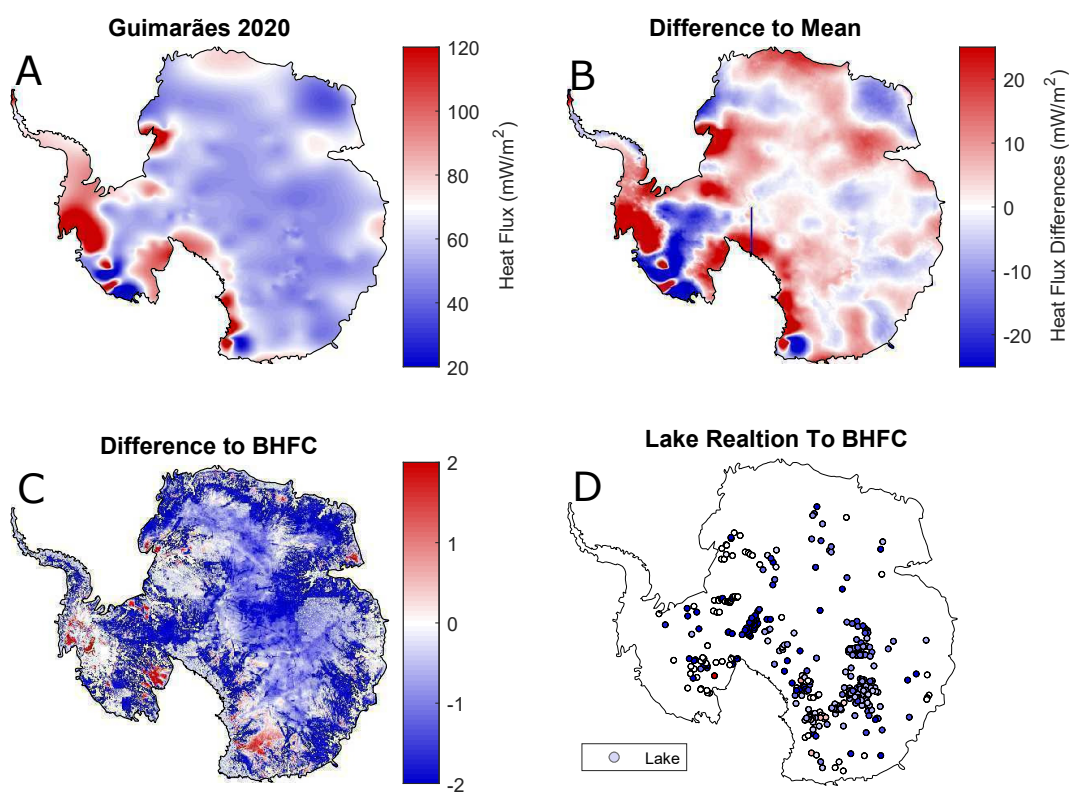
Figure B.4: Evaluation of Guimarães et al. (2020). A) The original Model, B) The model compared with the mean of the models (main text, figure 1A), C) The model compared with the basal heat flux constraint (main text, figure 3B) and D) A Map of lakes compared with the maximum discrepancy split into the 4 quantiles as explained in section 5.2 in the main text.
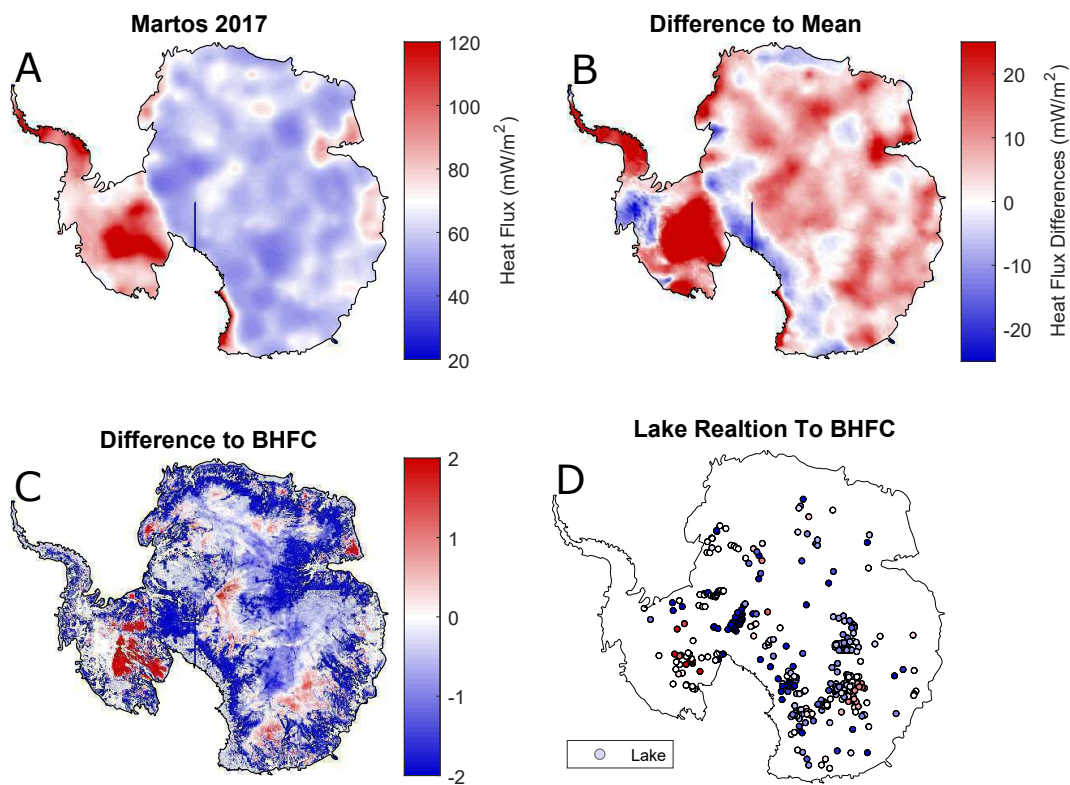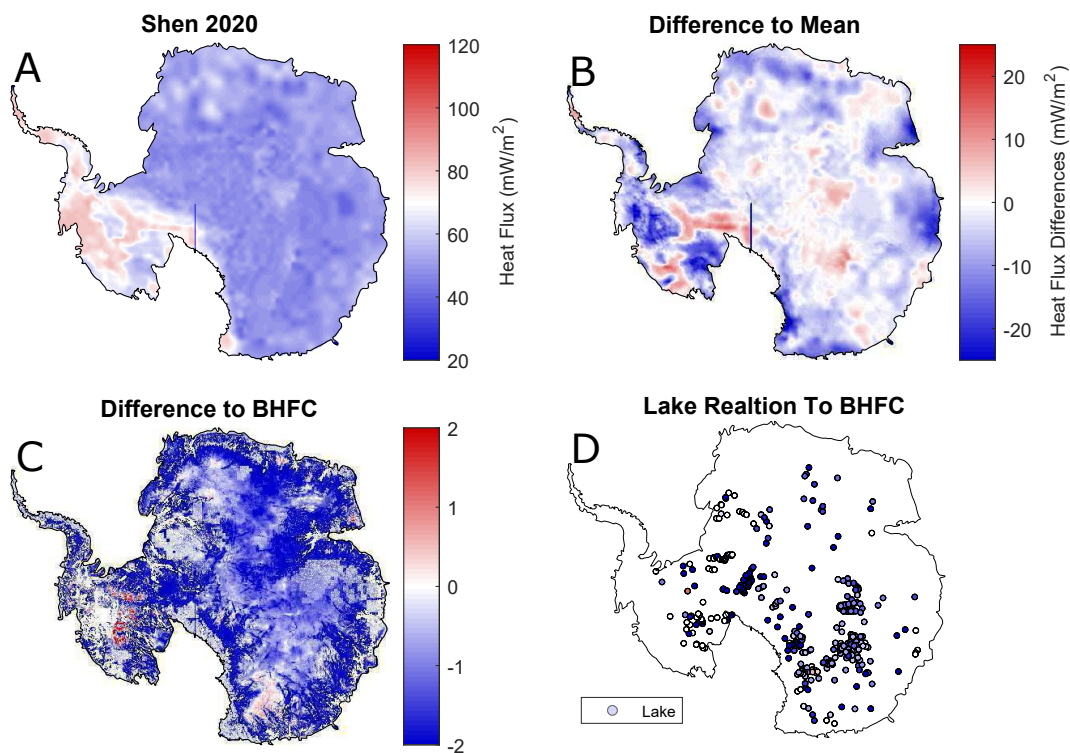
Figure B.5: Evaluation of Shen et al. (2020). A) The original Model, B) The model compared with the mean of the models (main text, figure 1A), C) The model compared with the basal heat flux constraint (main text, figure 3B) and D) A Map of lakes compared with the maximum discrepancy split into the 4 quantiles as explained in section 5.2 in the main text.
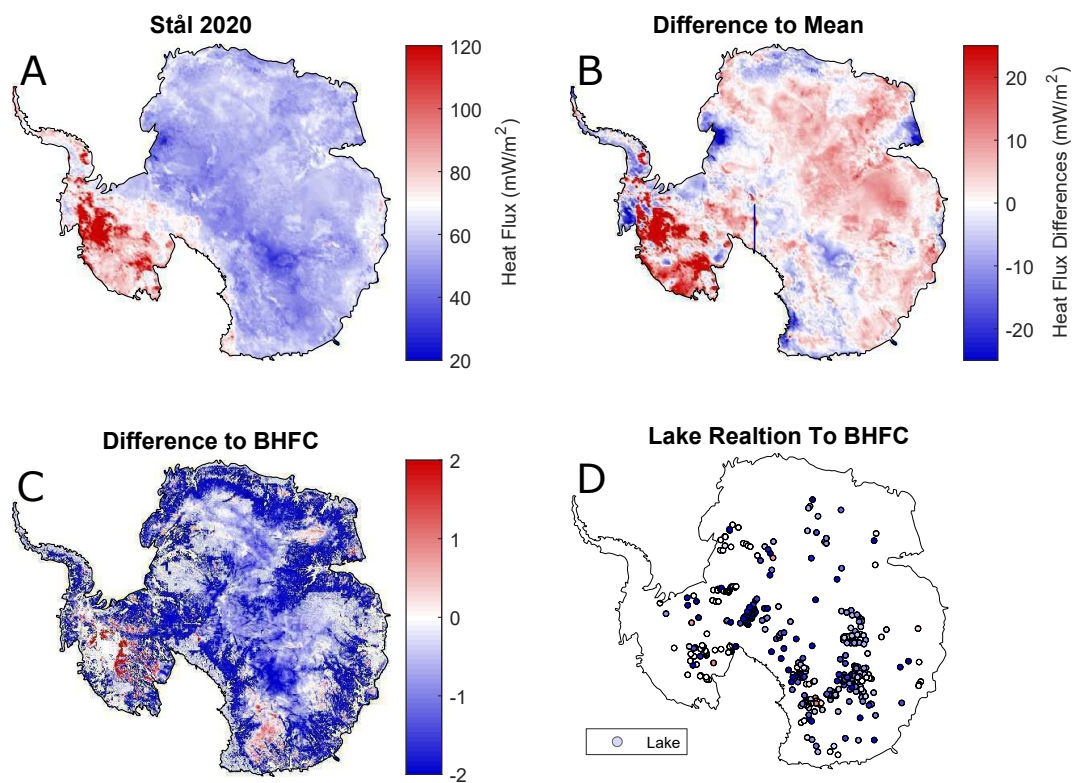
Figure B.6: Evaluaton of Stål et al. (2021). A) The original Model, B) The model compared with the mean of the models (main text, figure 1A), C) The model compared with the basal heat flux constraint (main text, figure 3B) and D) A Map of lakes compared with the maximum discrepancy split into the 4 quantiles as explained in section 5.2 in the main text.

Appendix C

Supplementary material for Chapter 6: Prediction of subglacial lake locations from site characteristics

Here we demonstrate the process in which we refined the subspace KNN model to create the most reliable prediction function.

C.1   Refining Subspace KNN model

A subspace KNN model is a form of ensemble model in which the KNN method of classifying a point is preformed over a number of ensembles consisting of a select number of dimensions (our environmental parameters). These scores from each ensemble are then weighted against each other with the most common classification across the ensembles being chosen as the final classification. We can adjust this model in two ways:

- First one can adjust the number of dimensions being used. Dimension can range from 1 (in which classification are based of individual environmental parameters) to 6 (in which classification are based of all 6 environmental parameters at once which is just a basic KNN).

- Second one can adjust the number of number of ensembles being used (also referred

as learners). We can run as many learners as we want but an obsessive number learners will result in oversampling in which the same combination of dimensions will be sampled multiple times.

For the learners, a sharp improvement was observed in our models accuracy in classifying the training data between 1-7 learners. However, past this point we see minimal to no improvement in our model accuracy (Figure C.1 A). Thus, to prevent oversampling of our learners, we will uses 7 learners in the final model. For dimensions a similar trend is observed as seen in the learners in which accuracy improves greatly between 1-4 dimensions but little to no improvement is seen beyond that point (Figure C.1 B) . We will uses 4 dimensions as 5 and 6 dimensions are somewhat limiting in ensemble arrangements in comparison.

C.2   Refining Lake and Antarctica data

In determining the optimal proxy distance to sample for our training null cells (cells with no lakes), we need a distance that keeps our null cells away from ideal lake environments while at the same time not limiting our sample space to the extremities of the Antarctic content. Although Figure C.1 C shows an increase in our model accuracy with a larger proxy distance, we note that, as shown in Figure C.2A at a distance greater than 200 km we will be unable to sample any null cells from the interior of the continent thus greatly reducing our diversity of points. Thus, we chose to set our proximity at 200 km, as this gives us the greatest accuracy, while still giving a wide distribution of null cell properties that are generally representative of the distribution of Antarctic environments (Figure C.2B).

With geothermal heat flux being a poorly known property in Antarctica we test the individual accuracies of the 6 models used along with the combined mean (C.1 D). Strangely we see newer models preforming more poorly in comparison to older models this conflicts with our assumption that the newer models Shen et al. (2020) and Stål et al. (2021) are more accurate representation of the true Antarctic Geothermal Heat Flux base of the
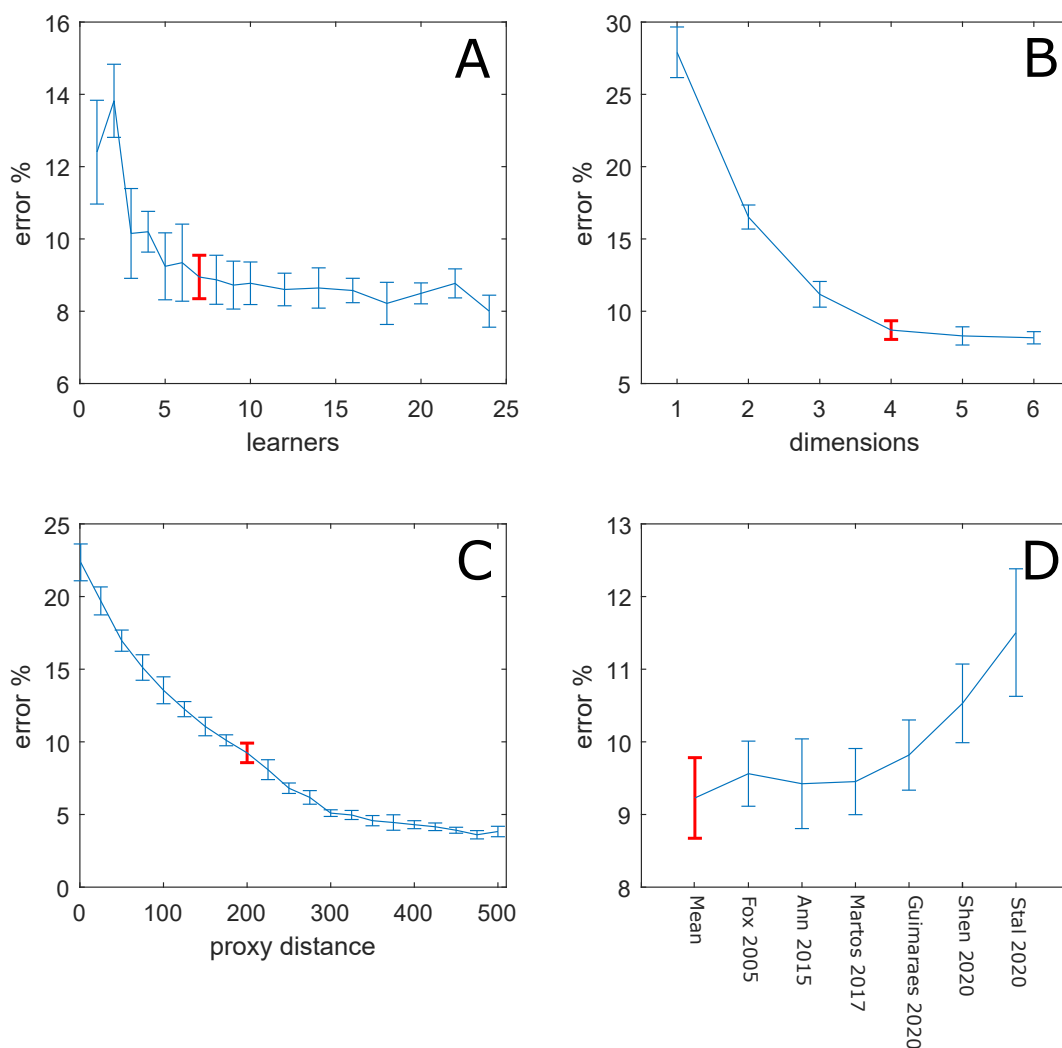
Figure C.1: The accuracy of our subspace KNN model (as measured by the percentage of incorrect classification in the training data) compared to the number of learners (A), the number of dimensions (B), null cells proxy distance from the lake (C) and heat flow model used (D). All models where run 11 times to create the error bars using the optimal variables as highlighted in the other figures. Highlighted bars indicate the final values used in the subspace KNN model used to create the prediction function.

techniques used. Regardless the mean preforms better than any individual model on its own and thus we will uses the mean of all 6 models as our value for heat flux.

C.3 Final Subspace KNN model's ROC curve

Receiver operating characteristic (ROC) curves shows the result of our models in identifying each classification types (stable, active and null) at different classification thresholds on the Subspace KNN output scores (Figure C.3). The better our data is at being clas-
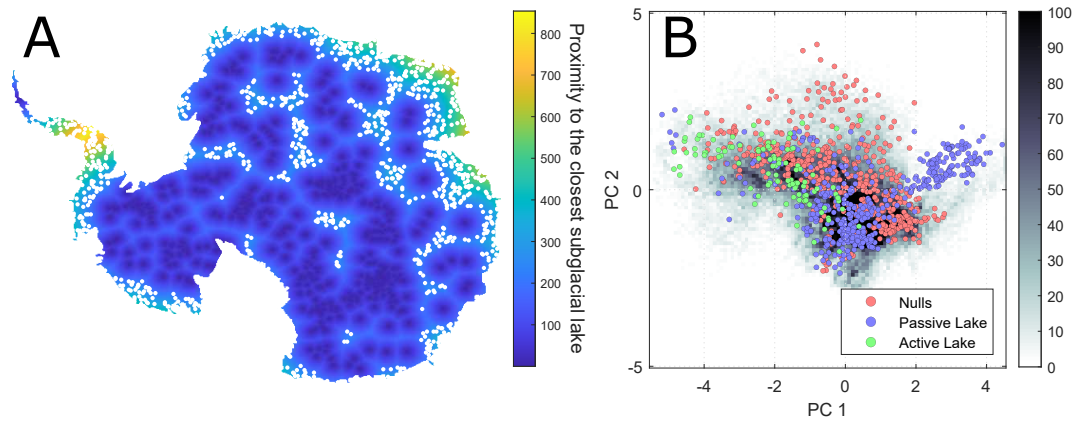
Figure C.2: A) Map of Antarctica showing proximity to the closest subglacial lake along with the location of null cells. B) Distribution of subglacial lakes and null cells across the 1st and 2nd principal axis (see main text).

sified by the subspace KNN model the quicker the true positive value (e.g. stable lake being identified as a stable lake) will approach 1 in comparisons to the false positive rate (e.g. active lake/ null cells being identified as a stable lake). This accuracy result can be measured by the area under the curve (AUC) with a value as close to 1 being desirable. The red dots seen in Figure C.3 represents the cut off thresholds our final subspace KNN model uses when classifying the data,

For stable lakes and null cells we see very strong ROC curves both with AUC values of 0.94 showing that our final Subspace KNN model identify most of the training data's stable lakes and null cells without many false identifications. As a result our final Subspace KNN model is, on average, able to identify 85% of null cells and 90% of stable lakes while only incorrectly identifying 5% of cells as null cells and 11% as stable lakes. While the final Subspace KNN model is excellent at identifying stable lakes and null cells it is not as accurate at identify active lakes. Our final Subspace KNN model is only able to identify 54 % of active lakes before the false positive rate becomes too large. As addressed in the paper poor the accuracy of our model in identify active lakes is likely a result of the limited number of active lakes in our training data combined with the wide distribution of active lake properties.
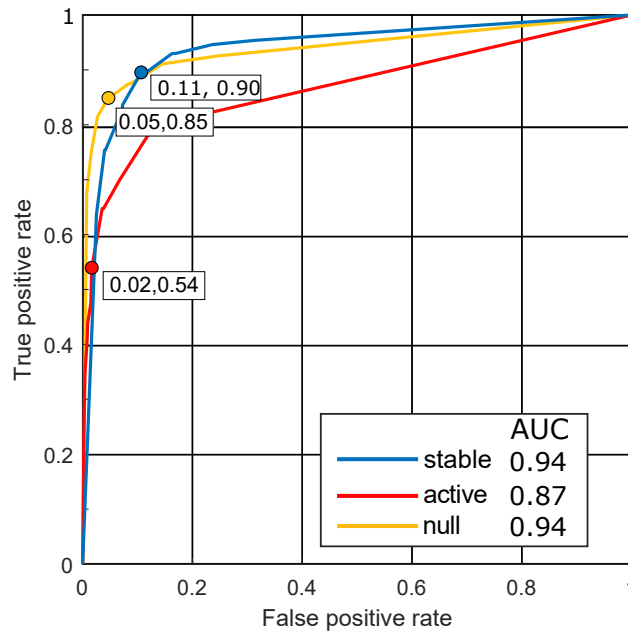
Figure C.3: ROC curves of the Active Lake Cells, Stable Lake Cells and Null Cells along with the area under each curve.

C.3.1   Separate Basal Heat Flux Models

To test the individual geothermal heat flux models on the classifier, we preform the same hyperparameters used to train the preferred classifier C.4. The result is fairly similar for each of the heat flux models, though there are a few differences in the details. For example, there are some differences in Dronning Maud Land, Ellsworth Land (Pine Island Glacier), and west of the Transantarctic Mountains. There is only a minor influence on the resulting classification accuracy as a result of these minor differences (Supplmentary Figure C.1D).
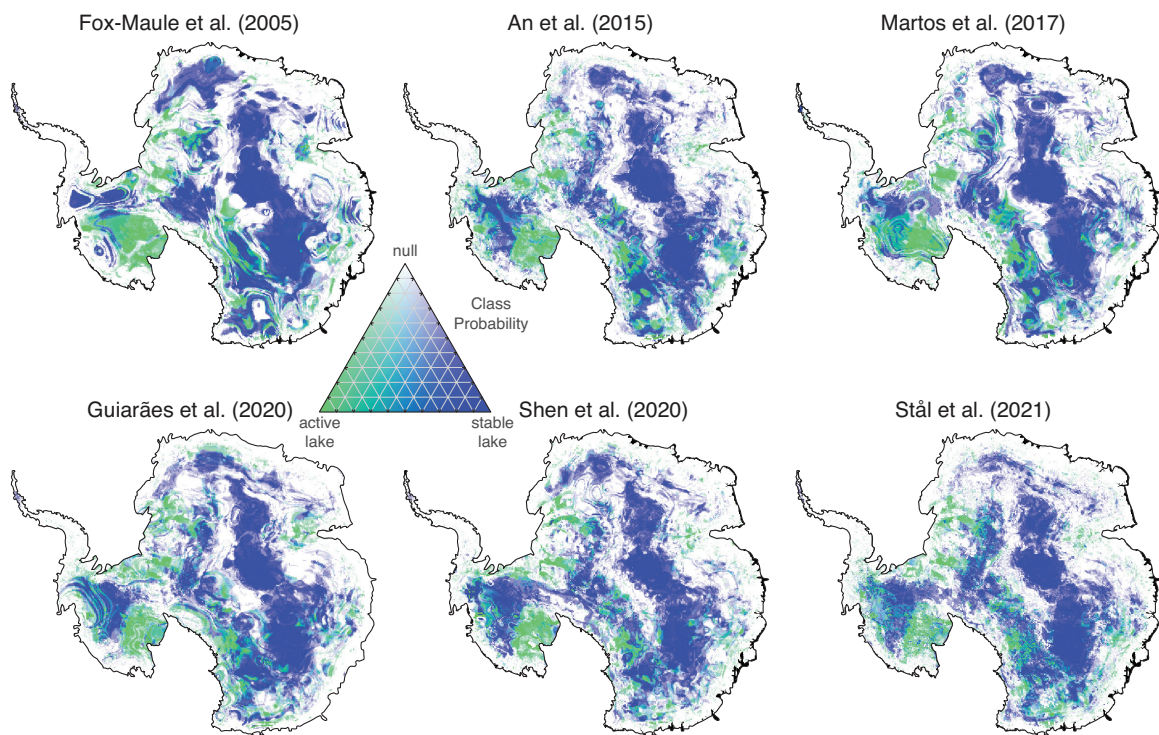
Figure C.4: Machine learning Classifier of lake melt sources as preformed in Figure 6 of the main text. Each map uses a one of the 6 proxy models as its value for basal heat flux.

Bibliography

An, M., Wiens, D. A., Zhao, Y., Feng, M., Nyblade, A., Kanao, M., Li, Y., Maggi, A. & Lévêque, J.-J. (2015), 'Temperature, lithosphere-asthenosphere boundary, and heat flux beneath the antarctic plate inferred from seismic velocities', *Journal of Geophysical Research: Solid Earth* **120**(12), 8720–8742.

Ashmore, D. W. & Bingham, R. G. (2014), 'Antarctic subglacial hydrology: current knowledge and future challenges', *Antarctic Science* **26**(6), 758–773.

Baranov, A., Tenzer, R. & Bagherbandi, M. (2017), 'Combined gravimetric–seismic crustal model for Antarctica', *Surveys in Geophysics* **39**(1), 23–56.

Barr, I. D., Spagnolo, M., Rea, B. R., Bingham, R. G., Oien, R. P., Adamson, K., Ely, J. C., Mullan, D. J., Pellitero, R. & Tomkins, M. D. (2022), '60 million years of glaciation in the transantarctic mountains', *Nature Communications* **13**(1).

Beardsmore, G. R. & Cull, J. P. (2001), *Crustal Heat Flow: A Guide to Measurement and Modelling*, Cambridge University Press.

Begeman, C. B., Tulaczyk, S. M. & Fisher, A. T. (2017), 'Spatially variable geothermal heat flux in west antarctica: Evidence and implications', *Geophysical Research Letters* **44**(19), 9823–9832.

Behn, M. & Kelemen, P. B. (2003), 'Relationship between seismic p-wave velocity and the composition of anhydrous igneous and meta-igneous rocks', *Geochem. Geophys. Geosyst.* **4**, 1041.

Behrendt, J. C. (1999), 'Crustal and lithospheric structure of the west antarctic rift system from geophysical investigations - a review', *Global and Planetary Change* **23**(1), 25–44.
   URL: *https://www.sciencedirect.com/science/article/pii/S0921818199000491*

Bell, R. E., Studinger, M., Shuman, C. A., Fahnestock, M. A. & Joughin, I. (2007), 'Large subglacial lakes in East Antarctica at the onset of fast-flowing ice streams', *Nature* **445**(7130), 904–907.
   URL: *https://doi.org/10.1038/nature05554*

Blackwell, D. D., Steele, J. L. & Brott, C. A. (1980), 'The terrain effect on terrestrial heat flow', *Journal of Geophysical Research: Solid Earth* **85**(B9), 4757–4772.

Blight, D. F. & Oliver, R. L. (1977), 'The metamorphic geology of the windmill islands, antarctica: A preliminary account', *Journal of the Geological Society of Australia* **24**(5-6), 239–262.

Bons, P. D., Jansen, D., Mundel, F., Bauer, C. C., Binder, T., Eisen, O., Jessell, M. W., Llorens, M.-G., Steinbach, F., Steinhage, D. & Weikusat, I. (2016), 'Converging flow and anisotropy cause large-scale folding in Greenland's ice sheet', *Nature Communications* **7**(1), 11427.

Brigaud, F. & Vasseur, G. (1989), 'Mineralogy, porosity and fluid control on thermal conductivity of sedimentary rocks', *Geophysical Journal International* **98**(3), 525–542.

Brocq, A. M. L., Ross, N., Griggs, J. A., Bingham, R. G., Corr, H. F. J., Ferraccioli, F., Jenkins, A., Jordan, T. A., Payne, A. J., Rippin, D. M. & Siegert, M. J. (2013), 'Evidence from ice shelves for channelized meltwater flow beneath the Antarctic Ice Sheet', *Nature Geoscience* **6**(11), 945–948.
   URL: *https://doi.org/10.1038/ngeo1977*

Burton-Johnson, A., Dziadek, R. & Martin, C. (2020), 'Review article: Geothermal heat flow in antarctica: current and future directions', *The Cryosphere* **14**(11), 3843–3873.
   URL: *https://doi.org/10.5194/tc-14-3843-2020*

Cameron, R. L. & Bull, G. B. (2013), The thermal diffusivity and thermal conductivity of glacial ice at wilkes station, antarctica, *in* 'Antarctic Research: The Matthew Fontaine Maury Memorial Symposium', American Geophysical Union, pp. 178–184.

Carter, S. P., Blankenship, D. D., Peters, M. E., Young, D. A., Holt, J. W. & Morse, D. L. (2007), 'Radar-based subglacial lake classification in antarctica', *Geochemistry, Geophysics, Geosystems* **8**(3), n/a–n/a.

Chapman, D. (1986), Thermal gradients in the continental crust, *in* J. Dawson, D. Carswell, J. Hall & K. Wedepohl, eds, 'The Nature of the Lower Continental Crust', number 24 *in* 'Special Publication', Geological Society of America, Denver, pp. 63–70.

Chopra, N., Ray, L., Satyanarayanan, M. & Elangovan, R. (2018), 'Evaluate best-mixing model for estimating thermal conductivity for granitoids from mineralogy: A case study for the granitoids of the Bundelkhand craton, central India', *Geothermics* **75**, 1–14.

Christner, B. C., Priscu, J. C., Achberger, A. M., Barbante, C., Carter, S. P., Christianson, K., Michaud, A. B., Mikucki, J. A., Mitchell, A. C., Skidmore, M. L., Vick-Majors, T. J., Adkins, W. P., Anandakrishnan, S., Barcheck, G., Beem, L., Behar, A., Beitch, M., Bolsey, R., Branecky, C., Edwards, R., Fisher, A., Fricker, H. A., Foley, N., Guthrie, B., Hodson, T., Horgan, H., Jacobel, R., Kelley, S., Mankoff, K. D., McBryan, E., Powell, R., Purcell, A., Sampson, D., Scherer, R., Sherve, J., Siegfried, M. & Tulaczyk, S. (2014), 'A microbial ecosystem beneath the west antarctic ice sheet', *Nature* **512**(7514), 310–313.
URL: *https://doi.org/10.1038/nature13667*

Clauser, C. & Huenges, E. (1995), Thermal conductivity of rocks and minerals, *in* T. Ahrens, ed., 'Rock Physics and Phase Relations: A Handbook of Physical Constants', Vol. 3 of *AGU Reference Shelf*, AGU, Washington, D.C., pp. 105–126.

Coletti, C., Borghi, A., Cossio, R., Dalconi, M. C., Santa, G. D., Peruzzo, L., Sassi, R., Vettorello, A. & Galgaro, A. (2021), 'A multi-scale methods comparison to provide gran-

itoid rocks thermal conductivity', *Construction and Building Materials* **304**, 124612.
URL: *https://doi.org/10.1016/j.conbuildmat.2021.124612*

Cook, S. J., Swift, D. A., Kirkbride, M. P., Knight, P. G. & Waller, R. I. (2020), 'The empirical basis for modelling glacial erosion rates', *Nature Communications* **11**(1).

Couston, L.-A. (2021), 'Turbulent convection in subglacial lakes', *Journal of Fluid Mechanics* **915**, A31.

Dahl-Jensen, D., Mosegaard, K., Gundestrup, N., Clow, G. D., Johnsen, S. J., Hansen, A. W. & Balling, N. (1998), 'Past temperatures directly from the Greenland ice sheet', *Science* **282**(5387), 268–271.

Davies, J. H. (2013), 'Global map of solid earth surface heat flow', *Geochemistry, Geophysics, Geosystems* **14**(10), 4608–4622.

Davis, M. G., Chapman, D. S., Wagoner, T. M. V. & Armstrong, P. A. (2007), 'Thermal conductivity anisotropy of metasedimentary and igneous rocks', *Journal of Geophysical Research* **112**(B5).

De, G., Robin, Q., Evans, S. & Bailey, J. T. (1969), 'Interpretation of radio echo sounding in polar ice sheets', *Philosophical Transactions of the Royal Society of London. Series A, Mathematical and Physical Sciences* **265**(1166), 437–505.
URL: *https://doi.org/10.1098/rsta.1969.0063*

de Q. Robin, G. (1955), 'Ice movement and temperature distribution in glaciers and ice sheets', *Journal of Glaciology* **2**, 523–532.

DeConto, R. M., Pollard, D., Alley, R. B., Velicogna, I., Gasson, E., Gomez, N., Sadai, S., Condron, A., Gilford, D. M., Ashe, E. L., Kopp, R. E., Li, D. & Dutton, A. (2021), 'The paris climate agreement and future sea-level rise from antarctica', *Nature* **593**(7857), 83–89.
URL: *https://doi.org/10.1038/s41586-021-03427-0*

Doran, P. T., Fritsen, C. H., McKay, C. P., Priscu, J. C. & Adams, E. E. (2002), 'Formation and character of an ancient 19-m ice cover and underlying trapped brine in an "ice-sealed" east antarctic lake', *Proceedings of the National Academy of Sciences* **100**(1), 26–31.
URL: *https://doi.org/10.1073/pnas.222680999*

Ehlers, T. A. (2005), 'Crustal thermal processes and the interpretation of thermochronometer data', *Reviews in Mineralogy and Geochemistry* **58**(1), 315–350.

Engelhardt, H. (2004), 'Ice temperature and high geothermal flux at Siple Dome, West Antarctica, from borehole measurements', *Journal of Glaciology* **50**(169), 251–256.

England, P. C. & Richardson, S. W. (1980), 'Erosion and the age dependence of continental heat flow', *Geophysical Journal International* **62**(2), 421–437.

Fagherazzi, S., Baticci, L., Brandon, C. M. & Rulli, M. C. (2021), 'Bedrock erosion in subglacial channels', *PLOS ONE* **16**(9), e0253768.

Fisher, A. T., Mankoff, K. D., Tulaczyk, S. M., Tyler, S. W. & Foley, N. (2015), 'High geothermal heat flux measured below the west antarctic ice sheet', *Science Advances* **1**(6).

Fortuin, J. & Oerlemans, J. (1990), 'Parameterization of the annual surface temperature and mass balance of Antarctica', *Annals of Glaciology* **14**, 78–84.

Fowler, C. (2006), *The Solid Earth*, 2ed edn, Cambridge.

Fretwell, P., Pritchard, H. D., Vaughan, D. G., Bamber, J. L., Barrand, N. E., Bell, R., Bianchi, C., Bingham, R. G., Blankenship, D. D., Casassa, G., Catania, G., Callens, D., Conway, H., Cook, A. J., Corr, H. F. J., Damaske, D., Damm, V., Ferraccioli, F., Forsberg, R., Fujita, S., Gim, Y., Gogineni, P., Griggs, J. A., Hindmarsh, R. C. A., Holmlund, P., Holt, J. W., Jacobel, R. W., Jenkins, A., Jokat, W., Jordan, T., King, E. C., Kohler, J., Krabill, W., Riger-Kusk, M., Langley, K. A., Leitchenkov, G., Leuschen, C., Luyendyk, B. P., Matsuoka, K., Mouginot, J., Nitsche, F. O., Nogi, Y., Nost, O. A.,

Popov, S. V., Rignot, E., Rippin, D. M., Rivera, A., Roberts, J., Ross, N., Siegert, M. J., Smith, A. M., Steinhage, D., Studinger, M., Sun, B., Tinto, B. K., Welch, B. C., Wilson, D., Young, D. A., Xiangbin, C. & Zirizzotti, A. (2013), 'Bedmap2: improved ice bed, surface and thickness datasets for Antarctica', *The Cryosphere* **7**(1), 375–393.

Fricker, H. A., Scambos, T., Bindschadler, R. & Padman, L. (2007), 'An active subglacial water system in west antarctica mapped from space', *Science* **315**(5818), 1544–1548.
  URL: *https://doi.org/10.1126/science.1136897*

Fricker, H. A., Siegfried, M. R., Carter, S. P. & Scambos, T. A. (2016), 'A decade of progress in observing and modelling Antarctic subglacial water systems', *Philosophical Transactions of the Royal Society A: Mathematical, Physical and Engineering Sciences* **374**(2059), 20140294.

Fuchs, S. & Balling, N. (2016), 'Improving the temperature predictions of subsurface thermal models by using high-quality input data. Part 2: A case study from the Danish-German border region', *Geothermics* **64**, 1–14.

Fuchs, S., Förster, H. J., Braune, K. & Förster, A. (2018), 'Calculation of thermal conductivity of low-porous, isotropic plutonic rocks of the crust at ambient conditions from modal mineralogy and porosity: A viable alternative for direct measurement?', *Journal of Geophysical Research: Solid Earth* **123**(10), 8602–8614.

Fuchs, S., Schütz, F., Förster, H.-J. & Förster, A. (2013), 'Evaluation of common mixing models for calculating bulk thermal conductivity of sedimentary rocks: Correction charts and new conversion equations', *Geothermics* **47**, 40–52.

Gard, M. (2021), Constraints on the Thermal State of the Continental Lithosphere, PhD thesis, University of Adelaide.

Gard, M. & Hasterok, D. (2021), 'A global curie depth model utilising the equivalent source magnetic dipole method', *Physics of the Earth and Planetary Interiors* **313**, 106672.
  URL: *https://doi.org/10.1016/j.pepi.2021.106672*

Gard, M., Hasterok, D. & Halpin, J. (2019), 'Global whole-rock geochemical database compilation', *Earth System Science Data Discussions* pp. 1–23.

Goeller, S., Steinhage, D., Thoma, M. & Grosfeld, K. (2016), 'Assessing the subglacial lake coverage of Antarctica', *Annals of Glaciology* **57**(72), 109–117.

Goes, S., Govers, R. & Vacher, P. (2000), 'Shallow mantle temperatures under europe from P and S wave tomography', *Journal of Geophysical Research* **105**(B5), 11153–11169.
URL: *https://doi.org/10.1029/1999jb900300*

Goes, S., Hasterok, D., Schutt, D. L. & Klöcking, M. (2020), 'Continental lithospheric temperatures: A review', *Physics of the Earth and Planetary Interiors* **306**, 106509.

Goldsby, D. L. & Kohlstedt, D. L. (2001), 'Superplastic deformation of ice: Experimental observations', *Journal of Geophysical Research: Solid Earth* **106**(B6), 11017–11030.

Golynsky, A. V., Ferraccioli, F., Hong, J. K., Golynsky, D. A., von Frese, R. R. B., Young, D. A., Blankenship, D. D., Holt, J. W., Ivanov, S. V., Kiselev, A. V., Masolov, V. N., Eagles, G., Gohl, K., Jokat, W., Damaske, D., Finn, C., Aitken, A., Bell, R. E., Armadillo, E., Jordan, T. A., Greenbaum, J. S., Bozzo, E., Caneva, G., Forsberg, R., Ghidella, M., Galindo-Zaldivar, J., Bohoyo, F., Martos, Y. M., Nogi, Y., Quartini, E., Kim, H. R. & Roberts, J. L. (2018), 'New Magnetic Anomaly Map of the Antarctic', *Geophysical Research Letters* **45**(13), 6437–6449.
URL: *https://doi.org/10.1029/2018gl078153*

Goscombe, B., Foster, D. A., Gray, D. & Wade, B. (2020), 'Assembly of central Gondwana along the Zambezi Belt: Metamorphic response and basement reactivation during the Kuunga Orogeny', *Gondwana Research* **80**, 410–465.

Gray, L. (2005), 'Evidence for subglacial water transport in the West Antarctic Ice Sheet through three-dimensional satellite radar interferometry', *Geophysical Research Letters* **32**(3).

Greve, R. & Blatter, H. (2009), *Dynamics of Ice Sheets and Glaciers*, Springer Berlin Heidelberg.

Gudlaugsson, E., Humbert, A., Kleiner, T., Kohler, J. & Andreassen, K. (2016), 'The influence of a model subglacial lake on ice dynamics and internal layering', *The Cryosphere* **10**(2), 751–760.

Guimarães, S. N. P., Vieira, F. P. & Hamza, V. M. (2020), 'Heat flow variations in the antarctic continent', *International Journal of Terrestrial Heat Flow and Applications* **3**(1), 1–10.

Harley, S. L., Fitzsimons, I. C. W. & Zhao, Y. (2013), 'Antarctica and supercontinent evolution: historical perspectives, recent advances and unresolved issues', *Geological Society, London, Special Publications* **383**(1), 1–34.

Hartmann, A., Rath, V. & Clauser, C. (2005), 'Thermal conductivity from core and well log data', *International Journal of Rock Mechanics and Mining Sciences* **42**(7-8), 1042–1055.

Harvey, P. K., Brewer, T. S., Lovell, M. A. & Kerr, S. A. (1998), 'The estimation of modal mineralogy: a problem of accuracy in core-log calibration', *Geological Society, London, Special Publications* **136**(1), 25–38.

Hasterok, D. & Chapman, D. (2007), 'Continental thermal isostasy II: Applications to North America', *J. Geophys. Res.* **112**, B06415.

Hasterok, D. & Chapman, D. (2011), 'Heat production and geotherms for the continental lithosphere', *Earth and Planetary Science Letters* **307**(1-2), 59–70.
URL: *https://doi.org/10.1016/j.epsl.2011.04.034*

Hasterok, D. & Gard, M. (2016), 'Utilizing thermal isostasy to estimate sub-lithospheric heat flow and anomalous crustal radioactivity', *Earth and Planetary Science Letters* **450**, 197–207.

Hasterok, D., Gard, M. & Webb, J. (2018), 'On the radiogenic heat production of metamorphic, igneous, and sedimentary rocks', *Geoscience Frontiers* **9**(6), 1777–1794.

Hasterok, D. P., Gard, M., Halpin, J. A., Hand, M. P., Stål, T., Raimondo, T. & McLaren, S. (2021), Improving thermal properties estimates of the antarctic crust and their uncertainties (invited), ep12d-02, *in* 'EOS Transactions', presented at 2021 Fall Meeting, AGU, New Orleans, LA, 13-17 Dec.

Hasterok, D. & Webb, J. (2017), 'On the radiogenic heat production of igneous rocks', *Geoscience Frontiers* **8**(5), 919–940.

Henderson, R. G. & Cordell, L. (1971), 'Reduction of unevenly spaced potential field data to a horizontal plane by means of finite harmonic series', *Geophysics* **36**(5), 856–866.

Herron, M. M. (1988), 'Geochemical classification of terrigenous sands and shales from core or log data', *SEPM Journal of Sedimentary Research* **Vol. 58**.
URL: *https://doi.org/10.1306/212f8e77-2b24-11d7-8648000102c1865d*

Horai, K. (1971), 'Thermal conductivity of rock-forming minerals', *J. Geophys. Res.* **76**, 1278–1308.

Horai, K.-I. & Baldridge, S. (1972), 'Thermal conductivity of nineteen igneous rocks, II estimation of the thermal conductivity of rock from the mineral and chemical compositions', *Physics of the Earth and Planetary Interiors* **5**, 157–166.

Horai, K. & Susaki, J. (1989), 'The effect of pressure on the thermal conductivity of silicate rocks up to 12 kbar', *Physics of the Earth and Planetary Interiors* **55**(3-4), 292–305.

Horgan, H. J., Anandakrishnan, S., Jacobel, R. W., Christianson, K., Alley, R. B., Heeszel, D. S., Picotti, S. & Walter, J. I. (2012), 'Subglacial lake whillans — seismic observations of a shallow active reservoir beneath a west antarctic ice stream', *Earth and Planetary Science Letters* **331-332**, 201–209.

Hughes, T. J. (2012), 'Thermal convection in ice sheets: New data, new tests', *Natural Science* **04**(07), 409–418.

Humbert, A., Steinhage, D., Helm, V., Beyer, S. & Kleiner, T. (2018), 'Missing evidence of widespread subglacial lakes at recovery glacier, antarctica', *Journal of Geophysical Research: Earth Surface* **123**(11), 2802–2826.

Jones, M. (1987), 'Heat flow and heat production in the Namaqua Mobile Belt, South Africa', *J. Geophys. Res.* **92**(B7), 6273–6289.

Jones, M. (1988), 'Heat flow in the Witwatersrand Basin and environs, and its significance for the South African shield geotherm and lithospheric thickness', *J. Geophys. Res.* **93**, 3243–3260.

Jordan, T. A., Riley, T. R. & Siddoway, C. S. (2020), 'The geological history and evolution of west antarctica', *Nature Reviews Earth & Environment* **1**, 1–17.

Kadir, S. M. S. A., Yunos, K. R. B. M., Omar, A. H. H. & Hamid, D. T. A. (2013), 'The daily life challenges faced by the researcher in arctic', *Procedia - Social and Behavioral Sciences* **90**, 764–771.

King, J. & Turner, J. (1997), *Antarctic Meteorology and Climatology*, Cambridge Universaty Press.

Krynauw, J. (1996), 'A review of the geology of east antarctica, with special reference to the c. 1000 ma and c. 500 ma events', *Terra Antarctica* **3**, 77–89.

Kuivinen, K. C. & Koci, B. R. (1982), 'South Pole ice core drilling, 1981–1982', *Antarctic Journal of the United States* **17**(5), 89–91. https://icedrill.org/library/south-pole-ice-core-drilling-1981-1982.

Lachenbruch, A. H. (1968), 'Rapid estimation of the topographic disturbance to superficial thermal gradients', *Reviews of Geophysics* **6**(3), 365–400.

Lai, C.-Y., Stevens, L. A., Chase, D. L., Creyts, T. T., Behn, M. D., Das, S. B. & Stone, H. A. (2021), 'Hydraulic transmissivity inferred from ice-sheet relaxation following greenland supraglacial lake drainages', *Nature Communications* **12**(1), 3955.
    URL: *https://doi.org/10.1038/s41467-021-24186-6*

Larour, E., Morlighem, M., Seroussi, H., Schiermeier, J. & Rignot, E. (2012), 'Ice flow sensitivity to geothermal heat flux of Pine Island Glacier, Antarctica', *Journal of Geophysical Research: Earth Surface* **117**(F044023).

Larour, E., Seroussi, H., Morlighem, M. & Rignot, E. (2012), 'Continental scale, high order, high spatial resolution, ice sheet modeling using the ice sheet system model (ISSM)', *Journal of Geophysical Research: Earth Surface* **117**(F1), n/a–n/a.

Lees, C. H. (1910), 'On the shapes of the isogeotherms under mountain ranges in radio-active districts', *Proceedings of the Royal Society A: Mathematical, Physical and Engineering Sciences* **83**(563), 339–346.

Liefferinge, B. V. & Pattyn, F. (2013), 'Using ice-flow models to evaluate potential sites of million year-old ice in Antarctica', *Climate of the Past* **9**(5), 2335–2345.

Lienhard, IV, J. H. & Lienhard, V, J. H. (2019), *A Heat Transfer Textbook*, 5th edn, Dover Publications, Mineola, NY.
URL: *http://ahtt.mit.edu*

Livingstone, S. J., Clark, C. D., Woodward, J. & Kingslake, J. (2013), 'Potential subglacial lake locations and meltwater drainage pathways beneath the antarctic and greenland ice sheets', *The Cryosphere* **7**(6), 1721–1740.
URL: *https://tc.copernicus.org/articles/7/1721/2013/*

Livingstone, S. J., Li, Y., Rutishauser, A., Sanderson, R. J., Winter, K., Mikucki, J. A., Björnsson, H., Bowling, J. S., Chu, W., Dow, C. F., Fricker, H. A., McMillan, M., Ng, F. S. L., Ross, N., Siegert, M. J., Siegfried, M. & Sole, A. J. (2022), 'Subglacial lakes and their changing role in a warming climate', *Nature Reviews Earth & Environment* **3**(2), 106–124.

Llubes, M., Lanseau, C. & Rémy, F. (2006), 'Relations between basal condition, subglacial hydrological networks and geothermal flux in Antarctica', *Earth and Planetary Science Letters* **241**(3-4), 655–662.

Lösing, M., Ebbing, J. & Szwillus, W. (2020), 'Geothermal heat flux in Antarctica: Assessing models and observations by bayesian inversion', *Frontiers in Earth Science* **8:105**.

Lucazeau, F. (2019), 'Analysis and mapping of an updated terrestrial heat flow dataset', *Geochemistry, Geophysics, Geosystems* **121**, 1328 – 1350.

Lwasa, S., Seto, K., Bai, X., Blanco, H., Gurney, K., Kilkiş, S., Lucon, O., Murakami, J., Pan, J., Sharifi, A. & Yamagata, Y. (2022), Urban systems and other settlements supplementary material, *in* P. Shukla, J. Skea, R. Slade, A. A. Khourdajie, R. van Diemen, D. McCollum, M. Pathak, S. Some, P. Vyas, R. Fradera, M. Belkacemi, A. Hasija, G. Lisboa, S. Luz & J. Malley, eds, 'IPCC, 2022: Climate Change 2022: Mitigation of Climate Change. Contribution of Working Group III to the Sixth Assessment Report of the Intergovernmental Panel on Climate Change', Cambridge University Press, Cambridge, UK and New York, NY, USA, chapter 8.

Lynas, M., Houlton, B. Z. & Perry, S. (2021), 'Greater than 99% consensus on human caused climate change in the peer-reviewed scientific literature', *Environmental Research Letters* **16**(11), 114005.
URL: *https://doi.org/10.1088/1748-9326/ac2966*

MacKie, E. J., Schroeder, D. M., Caers, J., Siegfried, M. R. & Scheidt, C. (2020), 'Antarctic topographic realizations and geostatistical modeling used to map subglacial lakes', *Journal of Geophysical Research: Earth Surface* **125**(3).

Magnússon, E., Pálsson, F., Gudmundsson, M. T., Högnadóttir, T., Rossi, C., Thorsteinsson, T., Ófeigsson, B. G., Sturkell, E. & Jóhannesson, T. (2021), 'Development of a subglacial lake monitored with radio-echo sounding: case study from the eastern Skaftá cauldron in the Vatnajökull ice cap, Iceland', *The Cryosphere* **15**(8), 3731–3749.
URL: *https://doi.org/10.5194/tc-15-3731-2021*

Maguire, R., Schmerr, N., Pettit, E., Riverman, K., Gardner, C., Della-Giustina, D., Avenson, B., Wagner, N., Marusiak, A. G., Habib, N., Broadbeck, J. I., Bray, V. J.

& Bailey, H. (2021), 'Geophysical constraints on the properties of a subglacial lake in northwest Greenland', *The Cryosphere* **15**, 3279–3291.

Maqsood, A., Kamran, K. & Gul, I. H. (2004), 'Prediction of thermal conductivity of granite rocks from porosity and density data at normal temperature and pressure: *in situ* thermal conductivity measurements', *Journal of Physics D: Applied Physics* **37**(24), 3396–3401.
URL: *https://doi.org/10.1088/0022-3727/37/24/007*

Mareschal, J.-C. & Jaupart, C. (2013), 'Radiogenic heat production, thermal regime and evolution of continental crust', *Tectonophysics* **609**, 524–534. Moho: 100 years after Andrija Mohorovicic.
URL: *https://www.sciencedirect.com/science/article/pii/S004019511200769X*

Marfunin, A. S. (2011), *Advanced Mineralogy*, Springer Berlin Heidelberg.

Marrero, S. M., Hein, A. S., Naylor, M., Attal, M., Shanks, R., Winter, K., Woodward, J., Dunning, S., Westoby, M. & Sugden, D. (2018), 'Controls on subaerial erosion rates in antarctica', *Earth and Planetary Science Letters* **501**, 56–66.

Martos, Y. M., Catalán, M., Jordan, T. A., Golynsky, A., Golynsky, D., Eagles, G. & Vaughan, D. G. (2017), 'Heat flux distribution of antarctica unveiled', *Geophysical Research Letters* **44**(22), 11,417–11,426.

MATLAB (2020), *version 9.8.0.1359463 (R2020a)*, The MathWorks Inc., Natick, Massachusetts.

Matthews, K. J., Maloney, K. T., Zahirovic, S., Williams, S. E., Seton, M. & Müller, R. D. (2016), 'Global plate boundary evolution and kinematics since the late paleozoic', *Global and Planetary Change* **146**, 226–250.

Maule, C. F. (2005), 'Heat flux anomalies in antarctica revealed by satellite magnetic data', *Science* **309**(5733), 464–467.

Maxwell, J. C. (2009), *A Treatise on Electricity and Magnetism*, Cambridge University Press.
URL: *https://doi.org/10.1017/cbo9780511709333*

McLaren, S., Sandiford, M., Hand, M., Neumann, N., Wyborn, L. & Bastrakova, I. (2003), The hot southern continent: heat flow and heat production in australian proterozoic terranes, *in* 'Evolution and Dynamics of the Australian Plate', Vol. 22 of *Special Pub.*, Geological Society of America, pp. 151–161.

Messager, M. L., Lehner, B., Grill, G., Nedeva, I. & Schmitt, O. (2016), 'Estimating the volume and age of water stored in global lakes using a geo-statistical approach', *Nature Communications* **7**(1).

Middlemost, E. A. (1994), 'Naming materials in the magma/igneous rock system', *Earth-Science Reviews* **37**(3-4), 215–224.
URL: *https://doi.org/10.1016/0012-8252(94)90029-9*

Miles, K. E., Willis, I. C., Benedek, C. L., Williamson, A. G. & Tedesco, M. (2017), 'Toward monitoring surface and subsurface lakes on the greenland ice sheet using sentinel-1 SAR and landsat-8 OLI imagery', *Frontiers in Earth Science* **5**.
URL: *https://doi.org/10.3389/feart.2017.00058*

Mony, L., Roberts, J. L. & Halpin, J. A. (2020), 'Inferring geothermal heat flux from an ice-borehole temperature profile at Law Dome, East Antarctica', *Journal of Glaciology* **66**(257), 509–519.

Morlighem, M., Rignot, E., Binder, T., Blankenship, D., Drews, R., Eagles, G., Eisen, O., Ferraccioli, F., Forsberg, R., Fretwell, P., Goel, V., Greenbaum, J. S., Gudmundsson, H., Guo, J., Helm, V., Hofstede, C., Howat, I., Humbert, A., Jokat, W., Karlsson, N. B., Lee, W. S., Matsuoka, K., Millan, R., Mouginot, J., Paden, J., Pattyn, F., Roberts, J., Rosier, S., Ruppel, A., Seroussi, H., Smith, E. C., Steinhage, D., Sun, B., van den Broeke, M. R., van Ommen, T. D., van Wessem, M. & Young, D. A. (2019), 'Deep

glacial troughs and stabilizing ridges unveiled beneath the margins of the Antarctic ice sheet', *Nature Geoscience* **13**(2), 132–137.

Nyblade, A., Pollack, H., Jones, D., Podmore, F. & Mushayandebvu, M. (1990), 'Terrestrial heat flow in east and southern Africa', *J. Geophys. Res.* **95**, 17371–17384.

Oswald, G. K. A. & Robin, G. D. Q. (1973), 'Lakes beneath the antarctic ice sheet', *Nature* **245**(5423), 251–254.

Palmer, S. J., Dowdeswell, J. A., Christoffersen, P., Young, D. A., Blankenship, D. D., Greenbaum, J. S., Benham, T., Bamber, J. & Siegert, M. J. (2013), 'Greenland subglacial lakes detected by radar', *Geophysical Research Letters* **40**(23), 6154–6159.

Parrenin, F., Cavitte, M. G. P., Blankenship, D. D., Chappellaz, J., Fischer, H., Gagliardini, O., Masson-Delmotte, V., Passalacqua, O., Ritz, C., Roberts, J., Siegert, M. J. & Young, D. A. (2017), 'Is there 1.5-million-year-old ice near Dome C, Antarctica?', *The Cryosphere* **11**(6), 2427–2437.

Passalacqua, O., Cavitte, M., Gagliardini, O., Gillet-Chaulet, F., Parrenin, F., Ritz, C. & Young, D. (2018), 'Brief communication: Candidate sites of 1.5 myr old ice 37 km southwest of the Dome C summit, East Antarctica', *The Cryosphere* **12**(6), 2167–2174.

Paterson, W. S. B. (1994), *The Physics of Glaciers*, Vol. 43, Pergamon.

Pattyn, F., Carter, S. P. & Thoma, M. (2016), 'Advances in modelling subglacial lakes and their interaction with the antarctic ice sheet', *Philosophical Transactions of the Royal Society A: Mathematical, Physical and Engineering Sciences* **374**(2059), 20140296.

Pearce, D., Hodgson, D., Thorne, M., Burns, G. & Cockell, C. (2013), 'Preliminary analysis of life within a former subglacial lake sediment in antarctica', *Diversity* **5**(3), 680–702.
URL: *https://doi.org/10.3390/d5030680*

Perol, T. & Rice, J. R. (2015), 'Shear heating and weakening of the margins of West Antarctic ice streams', *Geophysical Research Letters* **42**(9), 3406–3413.

Pittard, M. L., Roberts, J. L., Galton-Fenzi, B. K. & Watson, C. S. (2016), 'Sensitivity of the Lambert-Amery glacial system to geothermal heat flux', *Annals of Glaciology* **57**(73), 56–68.

Pollett, A., Hasterok, D., Raimondo, T., Halpin, J. A., Hand, M., Bendall, B. & McLaren, S. (2019), 'Heat flow in southern Australia and connections with East Antarctica', *Geochemistry, Geophysics, Geosystems* **20**(11), 5352–5370.
URL: *https://doi.org/10.1029/2019gc008418*

Price, P. B., Nagornov, O. V., Bay, R., Chirkin, D., He, Y., Miocinovic, P., Richards, A., Woschnagg, K., Koci, B. & Zagorodnov, V. (2002), 'Temperature profile for glacial ice at the South Pole: Implications for life in a nearby subglacial lake', *Proceedings of the National Academy of Sciences* **99**(12), 7844–7847.

Pringle, D. J., Eicken, H., Trodahl, H. J. & Backstrom, L. G. E. (2007), 'Thermal conductivity of landfast antarctic and arctic sea ice', *Journal of Geophysical Research* **112**(C04017).

Ray, L., Chopra, N., Hiloidari, S., Naidu, N. N. & Kumar, V. (2021), 'Thermal conductivity of granitoids of varying composition up to 300°c and implications for crustal thermal models', *Geophysical Journal International* **227**(1), 316–332.
URL: *https://doi.org/10.1093/gji/ggab191*

Ray, L., Förster, H.-J., Schilling, F. & Förster, A. (2006), 'Thermal diffusivity of felsic to mafic granulites at elevated temperatures', *Earth and Planetary Science Letters* **251**, 241–253.

Ray, L., Förster, H.-J., Förster, A., Fuchs, S., Naumann, R. & Appelt, O. (2015), 'Tracking the thermal properties of the lower continental crust: Measured versus calculated thermal conductivity of high-grade metamorphic rocks (Southern Granulite Province, India)', *Geothermics* **55**, 138–149.

Ray, L., Kumar, P. S., Reddy, G. K., Roy, S., Rao, G. V., Srinivasan, R. & Rao, R.

U. M. (2003), 'High mantle heat flow in a Precambrian granulite province: evidence from southern India', *Journal of Geophysical Research: Solid Earth* **108**(B2), 2084.

Reading, A. M., Stål, T., Halpin, J. A., Lösing, M., Ebbing, J., Shen, W., McCormack, F. S., Siddoway, C. S. & Hasterok, D. (2022), 'Antarctic geothermal heat flow and its implications for tectonics and ice sheets', *Nature Reviews Earth & Environment* .

Rhodes, J., Koteas, C., Mabee, S., Ryan, A. & Isaacson, M. (2013), The massachusetts geothermal data project, Database, Massachusetts Geological Survey.
URL: *https://mgs.geo.umass.edu/biblio/massachusetts-geothermal-data-project*

Ridley, J. K., Cudlip, W. & Laxon, S. W. (1993), 'Identification of subglacial lakes using ERS-1 radar altimeter', *Journal of Glaciology* **39**(133), 625–634.

Rignot, E. (2019), 'MEaSUREs phase map of Antarctic ice velocity, version 1'.

Robin, G. d. Q., Swithinbank, C. & Smith, B. (1970), 'Radio echo exploration of the antarctic ice sheet', *International Symposium on Antarctic Glaciological Exploration (ISAGE)* **3**(7), 97–115.
URL: *https://nora.nerc.ac.uk/id/eprint/526306*

Rodriguez-Galiano, V., Sanchez-Castillo, M., Chica-Olmo, M. & Chica-Rivas, M. (2015), 'Machine learning predictive models for mineral prospectivity: An evaluation of neural networks, random forest, regression trees and support vector machines', *Ore Geology Reviews* **71**, 804–818.
URL: *https://doi.org/10.1016/j.oregeorev.2015.01.001*

Rudnick, R. & Gao, S. (2014), Composition of the continental crust, *in* 'Treatise on Geochemistry', Elsevier, pp. 1–51.

S. Jennings, D. Hasterok, J. P. (2019), 'A new compositionally based thermal conductivity model for plutonic rocks', *Geophysical Journal International* **219**(2), 1377–1394.

Sanchez, G., Halpin, J. A., Gard, M., Hasterok, D., Stål, T., Raimondo, T., Peters, S. & Burton-Johnson, A. (2021), 'PetroChron antarctica: A geological database for

interdisciplinary use', *Geochemistry, Geophysics, Geosystems* **22**(12).
URL: *https://doi.org/10.1029/2021gc010154*

Schroeder, D. M., Blankenship, D. D., Young, D. A. & Quartini, E. (2014), 'Evidence for elevated and spatially variable geothermal flux beneath the west antarctic ice sheet', *Proceedings of the National Academy of Sciences* **111**(25), 9070–9072.
URL: *https://doi.org/10.1073/pnas.1405184111*

Sergienko, O. V. & Hindmarsh, R. C. A. (2013), 'Regular patterns in frictional resistance of ice-stream beds seen by surface data inversion', *Science* **342**(6162), 1086–1089.

Shapiro, N. (2004), 'Inferring surface heat flux distributions guided by a global seismic model: particular application to Antarctica', *Earth and Planetary Science Letters* **223**(1-2), 213–224.

Shen, W., Wiens, D. A., Anandakrishnan, S., Aster, R. C., Gerstoft, P., Bromirski, P. D., Hansen, S. E., Dalziel, I. W. D., Heeszel, D. S., Huerta, A. D., Nyblade, A. A., Stephen, R., Wilson, T. J. & Winberry, J. P. (2018), 'The crust and upper mantle structure of central and West Antarctica from bayesian inversion of Rayleigh wave and receiver functions', *Journal of Geophysical Research: Solid Earth* **123**(9), 7824–7849.
URL: *https://agupubs.onlinelibrary.wiley.com/doi/abs/10.1029/2017JB015346*

Shen, W., Wiens, D. A., Lloyd, A. J. & Nyblade, A. A. (2020), 'A geothermal heat flux map of antarctica empirically constrained by seismic structure', *Geophysical Research Letters* **47**(14).

Siegert, M. J. (2000), 'Antarctic subglacial lakes', *Earth-Science Reviews* **50**(1-2), 29–50.

Siegert, M. J. (2005), 'LAKES BENEATH THE ICE SHEET: The occurrence, analysis, and future exploration of lake vostok and other antarctic subglacial lakes', *Annual Review of Earth and Planetary Sciences* **33**(1), 215–245.

Siegert, M. J. & Dowdeswell, J. A. (1996), 'Spatial variations in heat at the base of the antarctic ice sheet from analysis of the thermal regime above subglacial lakes', *Journal of Glaciology* **42**(142), 501–509.

Siegert, M. J., Ellis-Evans, J. C., Tranter, M., Mayer, C., Petit, J.-R., Salamatin, A. & Priscu, J. C. (2001), 'Physical, chemical and biological processes in lake vostok and other antarctic subglacial lakes', *Nature* **414**(6864), 603–609.
URL: *https://doi.org/10.1038/414603a*

Siegert, M. J., Kulessa, B., Bougamont, M., Christoffersen, P., Key, K., Andersen, K. R., Booth, A. D. & Smith, A. M. (2017), 'Antarctic subglacial groundwater: a concept paper on its measurement and potential influence on ice flow', *Geological Society, London, Special Publications* **461**(1), 197–213.

Siegert, M. J., Kwok, R., Mayer, C. & Hubbard, B. (2000), 'Water exchange between the subglacial lake vostok and the overlying ice sheet', *Nature* **403**(6770), 643–646.
URL: *https://doi.org/10.1038/35001049*

Smith, R., Shaw, H., Leudke, R. & Russell, S. (1978), Comprehensive tables giving physical data and thermal energy estimates for young igneous systems of the united states, Technical report, U. S. Geological Survey.
URL: *https://doi.org/10.2172/6273152*

Stål, T., Reading, A. M., Halpin, J. A. & Whittaker, J. M. (2021), 'Antarctic geothermal heat flow model: Aq1', *Geochemistry, Geophysics, Geosystems* **22**(2).

Stearns, L. A., Smith, B. E. & Hamilton, G. S. (2008), 'Increased flow speed on a large east antarctic outlet glacier caused by subglacial floods', *Nature Geoscience* **1**(12), 827–831.
URL: *https://doi.org/10.1038/ngeo356*

Stephenson, R., Egholm, D. L., Nielsen, S. B. & Stovba, S. M. (2009), 'Role of thermal refraction in localizing intraplate deformation in southeastern Ukraine', *Nature Geoscience* **2**(4), 290–293.

Sundberg, J., Back, P.-E., Ericsson, L. O. & Wrafter, J. (2009), 'Estimation of thermal conductivity and its spatial variability in igneous rocks from in situ density logging', *International Journal of Rock Mechanics and Mining Sciences* **46**(6), 1023–1028.

Swain, A. K. (2019), 'Influence of thermal conductivity of rocks on polar ice sheet recession near schirmacher oasis, east antarctica', *Journal of the Geological Society of India* **93**(4), 455–465.

Talalay, P., Li, Y., Augustin, L., Clow, G. D., Hong, J., Lefebvre, E., Markov, A., Motoyama, H. & Ritz, C. (2020), 'Geothermal heat flux from measured temperature profiles in deep ice boreholes in Antarctica', *The Cryosphere* **14**(11), 4021–4037.

Thatje, S., Brown, A. & Hillenbrand, C.-D. (2019), 'Prospects for metazoan life in subglacial antarctic lakes: the most extreme life on earth?', *International Journal of Astrobiology* **18**(5), 416–419.

Turner, J., Marshall, G., Clem, K., Colwell, S., Phillips, T. & Lu, H. (2019), 'Antarctic temperature variability and change from station data', *International Journal of Climatology* **40**.

van der Veen, C. J., Leftwich, T., von Frese, R., Csatho, B. M. & Li, J. (2007), 'Subglacial topography and geothermal heat flux: Potential interactions with drainage of the Greenland Ice Sheet', *Geophysical Research Letters* **34**(L12501).

van Wessem, J. M., Reijmer, C. H., Lenaerts, J. T. M., van de Berg, W. J., van den Broeke, M. R. & van Meijgaard, E. (2014), 'Updated cloud physics in a regional atmospheric climate model improves the modelled surface energy balance of Antarctica', *The Cryosphere* **8**(1), 125–135.
URL: *https://doi.org/10.5194%2Ftc-8-125-2014*

Veiseh, S., Khodabandeh, N. & Hakkaki-Fard, A. (2009), 'Mathematical models for thermal conductivity-density relationship in fibrous thermal insulations for practical applications', *Asian Journal of Civil Engineering* **10**.

Verma, S. P., Torres-Alvarado, I. S. & Velasco-Tapia, F. (2003), 'A revised CIPW norm', *Swiss Bulletin of Mineralogy and Petrology* **83**(2), 197–216.

White, L. F., Bailey, I., Foster, G. L., Allen, G., Kelley, S. P., Andrews, J. T., Hogan,

K., Dowdeswell, J. A. & Storey, C. D. (2016), 'Tracking the provenance of Greenland-sourced, Holocene aged, individual sand-sized ice-rafted debris using the Pb-isotope compositions of feldspars and 40 Ar/ 39 Ar ages of hornblendes', *Earth and Planetary Science Letters* **433**, 192–203.

Wilkens, N., Behrens, J., Kleiner, T., Rippin, D., Rückamp, M. & Humbert, A. (2015), 'Thermal structure and basal sliding parametrisation at pine island glacier – a 3-d full-stokes model study', *The Cryosphere* **9**(2), 675–690.
URL: *https://doi.org/10.5194/tc-9-675-2015*

Willcocks, S., Hasterok, D. & Jennings, S. (2021), 'Thermal refraction: implications for subglacial heat flux', *Journal of Glaciology* pp. 1–10.

Wolff, E. & Doake, C. (1986), 'Implications of the form of the flow law for vertical velocity and age-depth profiles in polar ice', *Journal of Glaciology* **32**(112), 366–370.

Wright, A. & Siegert, M. (2012), 'A fourth inventory of antarctic subglacial lakes', *Antarctic Science* **24**(6), 659–664.

Wright, A., Young, D., Roberts, J., Schroeder, D., Bamber, J., Dowdeswell, J., Young, N., Le Brocq, A., Warner, R., Payne, A. et al. (2012), 'Evidence of a hydrological connection between the ice divide and ice sheet margin in the Aurora Subglacial Basin, East Antarctica', *Journal of Geophysical Research: Earth Surface* **117**(F1).

Ye, X., Yu, Z., Zhang, Y., Kang, J., Wu, S., Yang, T. & Gao, P. (2022), 'Mineral composition impact on the thermal conductivity of granites based on geothermal field experiments in the Songliao and Gonghe Basins, China', *Minerals* **12**(2), 247.
URL: *https://doi.org/10.3390/min12020247*

Young, D. A., Roberts, J. L., Ritz, C., Frezzotti, M., Quartini, E., Cavitte, M. G. P., Tozer, C. R., Steinhage, D., Urbini, S., Corr, H. F. J., van Ommen, T. & Blankenship, D. D. (2017), 'High-resolution boundary conditions of an old ice target near Dome C, Antarctica', *The Cryosphere* **11**(4), 1897–1911.